

*NANOCOMPOSITE MATERIALS
FOR HIGH-PERFORMANCE
ELECTROCHEMICAL
SUPERCAPACITORS*

*NANOCOMPOSITE MATERIALS
FOR HIGH-PERFORMANCE
ELECTROCHEMICAL
SUPERCAPACITORS*

By MOHAMED SAMIR HASSAN HASSAN NAWWAR

A Thesis Submitted to the School of Graduate Studies in Partial Fulfillment
of the Requirements for the Degree Doctor of Philosophy

McMaster University © Copyright by Mohamed Nawwar, July 2021

McMaster University DOCTOR OF PHILOSOPHY (2021)

Hamilton, Ontario (Materials Science and Engineering)

TITLE: Nanocomposite Materials for High-Performance Electrochemical
Supercapacitors

AUTHOR: Mohamed Samir Hassan Hassan Nawwar

M.Sc. in Chemical Engineering (Military Technical College MTC, Egypt)

B.Sc. in Chemical Engineering (Military Technical College MTC, Egypt)

SUPERVISOR:

Prof. Ishwar K. Puri, Ph.D., Fellow CAE, AAAS, ASME, Dean and Professor

CO-SUPERVISOR:

Prof. Igor Zhitomirsky, Distinguished Engineering Professor

Faculty of Engineering, McMaster University, Hamilton, Ontario, Canada

NUMBER OF PAGES: 187

Lay abstract

The rapid increase in human population has caused many economic problems, one of them the enormous energy consumption rate as compared to the limitations of sources available for clean and renewable energy sources.

Energy storage systems can be classified into different types, e.g., chemical, electrochemical, thermal, and mechanical systems. Popular electrochemical energy storage systems, such as batteries and capacitors, are used for many important daily applications but have difficulties while optimizing power and energy densities. Here, electrochemical supercapacitors (ESs) are considered potential energy storage systems that could balance power and energy densities with fast charge-discharge and a long lifetime.

The purpose of this research is to advance nanocomposite materials for electrochemical supercapacitor applications, where we use new colloidal approaches to fabricate high-performance electrochemical supercapacitor electrodes and devices. Our results reveal that these devices can have exceptional performance that facilitates new routes for their development.

Abstract

Electrochemical supercapacitors (ESs) are one of the most modern energy storage systems that offer a balance between power and energy densities in which the energy storage mechanisms could be an electrostatic double layer (EDLCs) and pseudocapacitive.

In this thesis, hybrid asymmetric supercapacitors have been developed to optimize the advantages for different types of (ESs) such as high conductivity, stability, fast charge-discharge, and relatively high performance. These developments include high active mass loading electrodes based on multiwall carbon nanotubes (MWCNTs) and transition metal oxides with incubation of low binder percentage and a high mass loading of 40 mg cm^{-2} that guarantees high electrochemical performance at a wide potential range for different electrodes, especially the cathodic one. Novel synthesis techniques and different multi-dispersants have been demonstrated; a conception colloidal fabrication method has been developed to improve the morphology/dispersion for composites of $\text{Fe}_3\text{O}_4/\text{MWCNTs}$ (M-CNTs) and $\text{NiFe}_2\text{O}_4/\text{MWCNTs}$.

Firstly, an advanced synthesis method called particle extraction through a liquid-liquid interface (PELLI) has been developed to enhance the dispersion of the nanoparticles M-CNTs. Furthermore, palmitic acid (PA) has been used as a surfactant in the bottom-up (PELLI) to reduce the agglomeration of M-CNTs with high Gamma (γ) ratio (nanoparticles/MWCNTs).

Moreover, different synthesis methods have been developed in the presence of celestine blue dye (CB) as a co-dispersant with advanced electrostatic interaction and coagulation mechanism that ensured well- dispersed of (Fe_3O_4 , NiFe_2O_4) coated (MWCNTs) at high mass loading.

Subsequently, more optimizations have been done to analyze the effect of different adsorption mechanisms by using other co-dispersant agents such as pyrocatechol violet (PV), azure A chloride (AA), and m-cresol purple (CP).

Finally, cyclic voltammetry, galvanic charge-discharge (GCD), electrochemical impedance spectroscopy (EIS), and cyclic stability have been done for the fabricated electrodes and devices in neutral aqueous electrolytes that showed a relevant electrochemical performance in a large potential range.

Acknowledgment

First and foremost, my deepest gratitude goes to my supervisors, Prof. Ishwar K. Puri and Prof. Igor Zhitomirsky, for always being available to provide answers, encouragement, research guidance, and discussions throughout this critical time. Nothing can describe how it feels to know that I have them as a mentor and adviser. Thanks for being as understanding as I worked through critical time requirements. Your excessive support, teaching, and encouragement are appreciated more than you know.

I would also like to express my sincere thanks to my committee member Prof. Hatem Zurob for his valuable discussion and suggestions. I would also express my gratitude to Prof. Mohamed Elbestawi for becoming one of my Ph.D. proposal and comprehensive examiners and give me good advice. I would thank collaborators: Dr. Rakesh P. Sahu, Dr. Ryan Poon, and Dr. Ri Chen for their kindly help, contribution, and cooperation. I am also thankful for my colleagues in the MuRG and Zhitomirsky electrochemical groups. I would also like to express my gratitude to the following people for their technical support for my Ph.D. research study: Dr. Britten, Dr. Victoria Jarvis, Dr. Carmen Andrei, and Dr. Aithal Srivatsa. I am so grateful to my beautiful country Egypt for their sponsorship and especially Dr. Ahmed Abd Elgawad and Dr. Ahmed Abdalla from TRC in Egypt for their support.

Lastly, but most importantly, I would like to express my indebtedness to my family for their prayers, inspiration, support, and blessed wishes. Words cannot express my gratitude to my wife Sally and my son Eyad for all the patience, love, and endless support.

M. Nawwar

Declaration of academic achievements

This dissertation was used to fulfill the requirements of an engineering Ph.D. degree. All the research projects were conducted from September 2018 to June 2021. Within this thesis research, advanced colloidal synthesis techniques and constructed materials have been adequately developed to fabricate composites. The developed composites have been suitable for the positive and negative electrodes of ESs. The major contributions of this thesis work were from my supervisors and me. The work of this thesis resulted in four journal papers; all of them were accepted and published in peer-reviewed journals. I was the first author and contributor on these papers that were listed in the following:

- **Mohamed Nawwar**, Ryan Poon, Ri. Chen, Rakesh P. Sahu, Ishwar K. Puri, and Igor Zhitomirsky, “**High areal capacitance of Fe₃O₄-decorated carbon nanotubes for supercapacitor electrodes**”. Carbon Energy, volume 1, issue 1, 124-133, 2019.
- **Mohamed Nawwar**, Ryan Poon, Rakesh P. Sahu, Ishwar K. Puri, and Igor Zhitomirsky, “**Fe₃O₄ spinel-Mn₃O₄ spinel ceramic supercapacitor prepared using celestine blue as a dispersant, capping agent and charge transfer mediator**”. Ceramics International, volume 46, issue 11, 18851–18858, 2020.
- **Mohamed Nawwar**, Rakesh P. Sahu, Ishwar K. Puri, and Igor Zhitomirsky, “**Functionally decorated carbon nanotube networks for energy storage in supercapacitors**”. Frontiers in Energy Research, volume 8, issue 46, 2020.

- **Mohamed Nawwar, Rakesh P. Sahu, Ishwar K. Puri, and Igor Zhitomirsky, “Pseudocapacitive behavior of ferrimagnetic NiFe_2O_4 -carbon nanotube electrodes prepared using a multifunctional dispersing agent”, Open Ceramics, Peer-reviewed Journal of the European Ceramic Society, volume 6C, 100127, 2021.**

Table of contents

| | |
|--|---------------|
| Lay abstract | iv |
| Abstract | v |
| Acknowledgment | vii |
| Declaration of academic achievements..... | viii |
| Table of contents..... | x |
| List of figures | xiv |
| List of tables | xxii |
| List of abbreviations and symbols | xxiii |
| Chapter 1 Literature review | 26 |
| 1.1 Introduction..... | 26 |
| 1.2 Fundamentals | 28 |
| 1.3 Classifications of electrochemical supercapacitors (ESs)..... | 31 |
| 1.3.1 Electrostatic double layer capacitors (EDLCs) | 32 |
| 1.3.2 Electrochemical pseudocapacitors | 34 |
| 1.3.3 Hybrid (asymmetric) supercapacitors | 36 |
| 1.4 Active materials for supercapacitors applications | 37 |
| 1.4.1 Carbon-based materials | 37 |
| 1.4.2 Redox-based materials | 38 |
| 1.5 Mass loadings of electrodes | 40 |
| 1.6 Dispersion of metal oxides..... | 41 |
| 1.7 Dispersion of MWCNTs | 45 |
| 1.8 Electrolytes for electrochemical supercapacitors (ESs)..... | 46 |
| 1.8.1 Aqueous electrolytes | 47 |
| 1.8.2 Organic electrolytes..... | 49 |

| | | |
|------------------|---|-----------|
| 1.8.3 | Ionic liquid electrolytes | 49 |
| Chapter 2 | Problem statement and objectives | 50 |
| 2.1 | Gaps in the field of asymmetric hybrid supercapacitors..... | 50 |
| 2.1.1 | Difficulties for dispersion of MWCNTs and agglomeration of MNPs | 50 |
| 2.1.2 | Low performance at high active mass loading | 51 |
| 2.1.3 | Low capacitance of negative electrodes (unmatched capacitance) | 53 |
| 2.2 | Objectives | 54 |
| Chapter 3 | Methodology and experimental work..... | 55 |
| 3.1 | Synthesis of the M-CNTs by chemical co-precipitation (CCP) and liquid-liquid extraction method (PELLI)..... | 55 |
| 3.2 | Synthesis of the MNPs coated MWCNTs using multifunctional dispersants | 56 |
| 3.3 | Material characterization | 56 |
| 3.3.1 | X-ray diffraction (XRD)..... | 57 |
| 3.3.2 | Transmission electron microscope (TEM) | 57 |
| 3.3.3 | RAMAN spectroscopy | 57 |
| 3.3.4 | FTIR spectroscopy | 57 |
| 3.4 | Electrode fabrication by impregnation..... | 57 |
| 3.5 | Electrochemical characterization | 58 |
| 3.5.1 | Cyclic voltammetry | 58 |
| 3.5.2 | Electrochemical impedance spectroscopy | 59 |
| 3.5.3 | Galvanostatic charge-discharge spectroscopy | 59 |
| 3.6 | References..... | 61 |
| Chapter 4 | High areal capacitance of Fe₃O₄-decorated carbon nanotubes for supercapacitor electrodes | 68 |
| 4.1 | Abstract..... | 69 |
| 4.2 | Introduction..... | 70 |
| 4.3 | Experimental procedures | 73 |

| | | |
|-----|-------------------------------|----|
| 4.4 | Results and discussion | 74 |
| 4.5 | Conclusions..... | 87 |
| 4.6 | Acknowledgement | 87 |
| 4.7 | References..... | 88 |
| 4.8 | Supporting informations | 94 |

**Chapter 5 Fe_3O_4 spinel- Mn_3O_4 spinel supercapacitor prepared using
Celestine blue as a dispersant, capping agent and charge
transfer mediator..... 95**

| | | |
|-----|--|-----|
| 5.1 | Abstract..... | 96 |
| 5.2 | Introduction..... | 97 |
| 5.3 | Experimental procedures | 100 |
| 5.4 | Results and discussion | 102 |
| 5.5 | Conclusions..... | 116 |
| 5.6 | Declaration of competing interest..... | 117 |
| 5.7 | Acknowledgements..... | 117 |
| 5.8 | References..... | 118 |
| 5.9 | Supporting informations | 123 |

**Chapter 6 Functionally decorated carbon nanotube networks for energy
storage in supercapacitors 125**

| | | |
|-----|-----------------------------------|-----|
| 6.1 | Abstract..... | 126 |
| 6.2 | Introduction..... | 127 |
| 6.3 | Experimental procedures | 129 |
| 6.4 | Results and discussion | 131 |
| 6.5 | Conclusions..... | 142 |
| 6.6 | Author contributions | 143 |
| 6.7 | Funding | 143 |
| 6.8 | Acknowledgments..... | 143 |
| 6.9 | Data availability statement | 144 |

| | | |
|------|-------------------------------|-----|
| 6.10 | Conflict of interest..... | 144 |
| 6.11 | Supplementary material..... | 144 |
| 6.12 | References | 145 |
| 6.13 | Supporting informations | 150 |

Chapter 7 Pseudocapacitive behavior of ferrimagnetic NiFe_2O_4 -carbon nanotube electrodes prepared with a multifunctional dispersing agent..... 153

| | | |
|-----|--|-----|
| 7.1 | Abstract..... | 154 |
| 7.2 | Introduction..... | 155 |
| 7.3 | Experimental procedures | 158 |
| 7.4 | Results and discussion | 159 |
| 7.5 | Conclusions..... | 173 |
| 7.6 | Declaration of competing interest..... | 173 |
| 7.7 | Acknowledgments..... | 173 |
| 7.8 | References..... | 174 |
| 7.9 | Supporting Informations | 183 |

Chapter 8 Conclusions and future works..... 184

| | | |
|-----|-------------------------|-----|
| 8.1 | Conclusions..... | 184 |
| 8.2 | Future directions | 187 |

List of figures

| | |
|---|----|
| Figure 1.1 Different designs of electrochemical supercapacitors (ESs) [3]. | 27 |
| Figure 1.2 Ragone plot for the main energy storage devices, relative discharge time in the dashed line [5]. | 28 |
| Figure 1.3 Schematic of simple conventional electrostatic capacitor [6]. | 29 |
| Figure 1.4 Classifications of electrochemical supercapacitors (ESs). | 31 |
| Figure 1.5 Schematic of EDLC [11]. | 33 |
| Figure 1.6 Schematics of EDLC during the charge-discharge cycles [3]. | 33 |
| Figure 1.7 Schematic of mechanisms for pseudocapacitance [3]. | 34 |
| Figure 1.8 Various reversible redox mechanisms for pseudocapacitance [10]. | 35 |
| Figure 1.9 Schematic structure and principles of a hybrid asymmetric supercapacitor [21]. | 36 |
| Figure 1.10 Various conducting polymer structures. (A) (PPy), (B) (PAni), (C) (PTh) and (D) (PEDOT) [31]. | 39 |
| Figure 1.11 Schematic of surface charge of particles as a function of pH [34]. | 42 |
| Figure 1.12 Chemical structures of (A) CA, (B) TCA, (C) PCA, and (D) DCA [35]. | 44 |
| Figure 1.13 Chemical structures of (A) PHA, (B) PGR, (C) AZA, and (D) NB [35,37]. | 45 |
| Figure 1.14 Effects of the properties of the electrolyte on the ESs performance [43]. | 47 |
| Figure 1.15 Potential windows of various electrode materials in aqueous electrolyte [48]. | 48 |

| | |
|--|----|
| Figure 2.1 Schematic for surface modifications of MWCNTs [56]. | 51 |
| Figure 2.2 CV profile for asymmetric device shows the effect of increasing the active mass loadings [33]. | 52 |
| Figure 2.3 CV profile for an asymmetric device shows the unmatched capacitance [62]. | 53 |
| Figure 3.1 Schematic for the fabrication of M-CNTs composite by liquid-liquid extraction methods. | 55 |
| Figure 3.2 Schematic for the fabrication of M-CNTs composites by using multifunctional dispersant. | 56 |
| Figure 3.3 Schematic of composite electrode fabrication using slurry impregnation [34]. | 58 |
| Figure 3.4 (A) Potentiostat (PARSTAT 2273, Princeton Applied Research), (B) The three electrodes cell setup, and (C) The supercapacitor device testing setup. | 59 |
| Figure 3.5 (A) Charge-discharge setup for single electrodes using analyzer (biologic VMB 300), (B) Battery analyzers (MTI Corporation, USA). | 60 |
| Figure 4.1 X-ray diffraction patterns of (a) Fe ₃ O ₄ powder, (b) M-CNTs, and (c) acid-treated CNTs. ▼, JCPDS file 19-0629; ●, JCPDS No. 41-1487; M-CNTs, magnetite-decorated carbon nanotube. | 75 |
| Figure 4.2 A, STEM image; B, EDX line scan for Fe (the line is shown in (A)). EDX, energy-dispersive X-ray spectroscopy; STEM, scanning transmission electron microscope. | 76 |
| Figure 4.3 A, Chemical structure of PA; B, adsorption mechanisms, involving Fe atoms on the particle surface and carboxylic acid group of PA: (a) chelation, (b) bridging. PA, Palmitic acid. | 77 |

Figure 4.4 CVs at scan rates of (a) 2, (b) 5, and (c) 10 mV s⁻¹ for M-CNTs electrodes, prepared (A, B) without PELLI and (C, D) using PELLI for (A, C) $\gamma = 0.40$ and (B, D) $\gamma = 1.0$. M-CNTs, magnetite-decorated carbon nanotube; PELLI, particle extraction through liquid-liquid interface. 78

Figure 4.5 C_s and C_m vs scan rate for M-CNTs: A, prepared without PELLI and B, using PELLI for (a) $\gamma = 1.0$, (b) $\gamma = 0.70$, (c) $\gamma = 0.55$, (d) $\gamma = 0.40$, and (e) $\gamma = 0.25$. M-CNTs, magnetite-decorated carbon nanotube; PELLI, particle extraction through liquid-liquid interface. 79

Figure 4.6 EIS data for M-CNTs electrodes, prepared (A, B, C) without PELLI and (D, E, F) using PELLI: (A, D) Nyquist plot of complex impedance and frequency dependences of (B, E) C_s' and (C, F) C_s'' for (a) $\gamma = 0.40$, and (b) $\gamma = 1.00$. EIS, electrochemical impedance spectroscopy; M-CNTs, magnetite-decorated carbon nanotube; PELLI, particle extraction through liquid-liquid interface.. 81

Figure 4.7 A, Charge-discharge curves for M-CNTs electrodes ($\gamma = 1.0$) prepared (a, b) without PELLI and (c, d) using PELLI at current densities of (a, c) 20 and (b, d) 3mA cm⁻²; B, C_s and C_m vs. scan rate for M-CNTs electrodes ($\gamma = 1.0$) prepared (a) without PELLI and (b) using PELLI. M-CNTs, magnetite-decorated carbon nanotube; PELLI, particle extraction through liquid-liquid interface..... 82

Figure 4.8 A, CVs at scan rates of (a) 2, (b) 5, and (c) 10 mV s⁻¹; B, C_s and C_m vs scan rate; C, Nyquist plot of complex impedance and frequency dependences of D, C_s' and E C_s'' for an asymmetric supercapacitor cell, containing MnO₂-CNTs as a positive electrode and M-CNTs ($\gamma = 1.0$). Prepared using PELLI as a negative electrode. M-CNTs, magnetite-decorated carbon nanotube; PELLI, particle extraction through liquid-liquid interface. 84

| | |
|---|-----|
| Figure 4.9 A, Charge-discharge curves at current densities of (a) 3, (b) 5, (c) 10, (d) 20, (e) 30, (f) 40, and (g) 50mAcm ⁻² ; B, C _s and C _m vs. current density for an asymmetric supercapacitor cell, containing MnO ₂ -CNTs as a positive electrode and M-CNTs ($\gamma=1.0$) prepared using PELLI as a negative electrode. M-CNTs, magnetite-decorated carbon nanotube; PELLI, particle extraction through liquid-liquid interface..... | 85 |
| Figure 4.10 A, Ragone plot for an asymmetric supercapacitor cell, containing MnO ₂ -CNTs as a positive electrode and M-CNTs ($\gamma = 1.0$) prepared using PELLI as a negative electrode; B, (a) capacitance retention and (b) Coulombic efficiency vs cycle number. M-CNTs, magnetite-decorated carbon nanotube; PELLI, particle extraction through liquid-liquid interface. | 86 |
| Figure 4.11 (A) PELLI for M-CNTs by PA (B) Separation of the inorganic phase with the impurities and sideproducts. | 94 |
| Figure 5.1 (A) chemical structure of cationic CB, containing a chelating catechol group, (B) unzipping mechanism of CNT dispersion using CB, (C) interaction of CB with Fe ₃ O ₄ particles: chelating bonding and electrostatic attraction, (D) schematic of Fe ₃ O ₄ decorated CNT and CB interaction with both materials, (E) redox reaction of CB..... | 105 |
| Figure 5.2 X-ray diffraction patterns of (a) mixture of Fe ₃ O ₄ and CNT prepared without CB and (b) FDCNT (▼-JCPDS file No. 19-0629, ●-JCPDS No. 22-1012). | 106 |
| Figure 5.3 Raman spectroscopy data for (a) as-received CNT (b) precipitated Fe ₃ O ₄ , (c) mixture of Fe ₃ O ₄ and CNT, (d) CB dye, and (d) FDCNT for $\gamma= 1.50$ | 107 |
| Figure 5.4 TEM of FDCNT for different (γ): (A, B) 1.50, and (C) 2.00. (D) EDX line scan for Fe, the line is shown in (B). | 108 |

Figure 5.5. (A) CVs at scan rate of 5 mV s^{-1} , (B) C_s and C_m versus scan rate, (C) EIS Nyquist plot, (D) C_s' versus frequency and (E) C_s'' versus frequency for electrodes with $\gamma=1.00$, prepared (a, b) without CB and (c, d) with CB using different methods: (a, c) in-situ chemical precipitation and (b, d) mixing. ... 111

Figure 5.6 Testing data for FDCNT electrodes: (A-C) CVs at scan rates of (a) 2, (b) 5, and (c) 10 mV s^{-1} with (A) $\gamma=1.25$, (B) $\gamma=1.50$, and (C) $\gamma=2.00$; (D) C_s and C_m versus scan rate. (E) Nyquist plot of complex impedance and frequency dependences of (F) C_s' and (G) C_s'' for D(a), E(a), F(a), G(a) $\gamma=1.25$; D(b), E(b), F(b), G (b) $\gamma=1.50$, and D(c), E(c), F(c), G(c) $\gamma=2.00$ 112

Figure 5.7 C_s and C_m versus scan rate for FDCNT electrodes with $\gamma=1.50$ obtained from charge-discharge curves (inset) at current densities of (a) 3, (b) 5, (c) 7, and (d) 10 mA cm^{-2} 114

Figure 5.8 (A) CVs at scan rates of (a) 2, (b) 5 and (c) 10 mV s^{-1} , (B) C_s and C_m versus scan rate, (C) Nyquist plot of complex impedance and frequency dependences of (D) C_s' and (E) C_s'' for an asymmetric supercapacitor cell. 115

Figure 5.9 (A) C_s and C_m versus charge-discharge rate, obtained from charge-discharge curves (inset) at current densities of (a) 3, (b) 5, (c) 7, (d) 20, (e) 30, (f) 40, and (g) 50 mA cm^{-2} , (B) Ragone plot for an asymmetric supercapacitor cell. 116

Figure 5.10 (A) CVs at scan rates of (a) 2, (b) 5 and (c) 10 mV s^{-1} , (B) C_s and C_m versus scan rate, (C) Nyquist plot of complex impedance and frequency dependences of (D) C_s' and (E) C_s'' . For a positive Mn_3O_4 -CNT electrode, prepared by precipitation using CB. 123

Figure 5.11 Charge-discharge curves at current densities of (a) 3, (b) 5, (c) 7, and (d) 10 mA cm^{-2} , for a positive Mn_3O_4 -CNT electrode, prepared by precipitation using CB. 124

| | |
|--|-----|
| Figure 6.1 Chemical structures of (A) CB, (B) PV, (C) AA, (D) CP and schematics, showing (E) unzipping of MWCNT bundles by dispersants, (F) electrostatic repulsion of PV and Fe ₃ O ₄ particles and chelating bonding of PV to Fe atoms on the Fe ₃ O ₄ particle surface, involving a catechol group of PV, (G) electrostatic attraction of AA and Fe ₃ O ₄ . | 133 |
| Figure 6.2 X-ray diffraction patterns of (a) M-CB-MWCNT, (b) M-PV-MWCNT, (c) M-AA-MWCNT, and (d) M-CP-MWCNT. | 134 |
| Figure 6.3 TEM images at different magnifications for (A–C) M-CB-MWCNT, (D–F) M-PV-MWCNT, (G–I) M-AA-MWCNT, and (J–L) M-CP-MWCNT. | 135 |
| Figure 6.4 (A) Average data (40 samples of each composition) for DLS analysis of (a) M-CB-MWCNT, (b) M-PV-MWCNT, (c) M-AA-MWCNT and (d) M-CP-MWCNT, (B) Typical spectrum for M-CP-MWCNT. The width of the peaks indicates the polydispersity of the aggregate (Pd). | 136 |
| Figure 6.5 (A,C) CVs and (B,D) capacitance vs. scan rate for (a) M-CB-MWCNT, (b) M-FH-CB-MWCNT, (c) M-PV-MWCNT, (d) M-AA-MWCNT and (e) M-CP-MWCNT electrodes. | 138 |
| Figure 6.6 (A–D) Frequency dependences of components of complex AC capacitance, calculated from impedance data for (a) M-CB-MWCNT, (b) M-FH-CB-MWCNT, (c) M-PV-MWCNT, (d) M-AA-MWCNT and (e) M-CP-MWCNT electrodes. | 139 |
| Figure 6.7 (A) Charge-discharge curves at current density of 5mA cm ⁻² , (B) capacitance, calculated from charge-discharge data, vs. current density for (a) M-CB-MWCNT, (b) M-FH-CB-MWCNT, (c) M-PV-MWCNT, (d) M-AA-MWCNT and (e) M-CP-MWCNT. | 140 |

| | |
|---|-----|
| Figure 6.8 (A) CVs at scan rates of (a) 2, (b) 5 and (c) 10 mV s ⁻¹ , (B) C _s and C _m calculated from the CV data versus scan rate, (C) Nyquist plot of complex impedance and frequency dependences of (D) C _s ' and (E) C _s " for an asymmetric supercapacitor cell, containing M-FH-CB-MWCNT as a negative electrode and MnO ₂ -MWCNT as a positive electrode..... | 141 |
| Figure 6.9 (A) C _s and C _m vs current density calculated from discharge data, inset shows charge-discharge curves, and different current densities, (B) (a) Coulombic efficiency and (b) capacitance retention and vs. cycle number, (C) Ragone plot for an asymmetric supercapacitor cell, containing M-FH-CB-MWCNT as a negative electrode and MnO ₂ -MWCNT as a positive electrode, (D) LEDs powered by two asymmetric cells..... | 142 |
| Figure 6.10 X-ray diffraction patterns of Fe ₃ O ₄ powder (JCPDS file 19-0629). | 150 |
| Figure 7.1 (A) Chemical structure of cationic CB, containing a chelating catechol group (B) interaction of CB with NiFe ₂ O ₄ particles: chelating bonding with M (Ni, Fe), and (C) unzipping mechanism of MWCNTs dispersion using CB, decoration of MWCNTs and NiFe ₂ O ₄ by CB interaction with both materials. | 161 |
| Figure 7.2 X-ray diffraction patterns of (a) mixture of NiFe ₂ O ₄ with MWCNTs and (b) NiFe ₂ O ₄ -MWCNTs composite, prepared using CB for $\gamma=1$ in comparison with JCPDS file 22-1012 and 58-1638. | 162 |
| Figure 7.3 FTIR spectrum data for (a) mixture of NiFe ₂ O ₄ with MWCNTs and (b) NiFe ₂ O ₄ -MWCNTs composite, prepared using CB, for $\gamma=1$ | 163 |
| Figure 7.4 (A-D) TEM images of NiFe ₂ O ₄ -MWCNT ($\gamma=1$) prepared using CB and related EDX data: (A,C) TEM images at different magnifications, (B) EDX line scan for Fe and Ni for the line shown in (A); (D) EDX mapping for elements (Ni, Fe, C, O) for the image shown in (C). | 164 |

| | |
|--|-----|
| Figure 7.5 (A) CVs at a scan rate of 2 mV s^{-1} , (B) C_s versus scan rate, (C) EIS Nyquist plot, (D) C_s' versus frequency and (E) C_s'' versus frequency for electrodes, containing (a) 20 mg cm^{-2} NiFe_2O_4 (b) 20 mg cm^{-2} MWCNTs, and (c) a mixture of 20 mg cm^{-2} NiFe_2O_4 and 20 mg cm^{-2} MWCNTs . | 166 |
| Figure 7.6 (A) CVs at scan rate of 5 mV s^{-1} , (B) capacitance versus scan rate, (C) EIS Nyquist plot, (D) C_s' versus frequency and (E) C_s'' versus frequency for NiFe_2O_4 -MWCNTs electrodes with $\gamma = 1.5$, prepared (a) without CB (b) using CB as a dispersant. | 168 |
| Figure 7.7 (A) CVs at scan rate of 10 mV s^{-1} , (B) capacitance versus scan rate, (C) EIS Nyquist plot, (D) C_s' versus frequency and (E) C_s'' versus frequency for NiFe_2O_4 -MWCNTs electrodes prepared using CB for (a) $\gamma = 1$, (b) $\gamma = 2.5$ and (c) $\gamma = 4$. | 169 |
| Figure 7.8 (A) Charge-discharge curves at current densities of 3 mA cm^{-2} and (B) 40 mA cm^{-2} , (C) capacitance versus current density for NiFe_2O_4 -MWCNTs composites with (a) $\gamma = 1$ (b) $\gamma = 2.5$, and (c) $\gamma = 4$. (D) (a) Capacitance retention and (b) Coulombic efficiency versus cycle number for $\gamma = 1$. | 170 |
| Figure 7.9 (A) CVs at scan rate of 5 mV s^{-1} , (B) C_s and C_m versus scan rate, (C) EIS Nyquist plot, (D) C_s' versus frequency and (E) C_s'' versus frequency for electrodes by 40 mg of NiFe_2O_4 /MWCNTs for $\gamma = 1$, prepared by physical mixing and probe sonication of (a) 5 min (b) 10 min . | 183 |

List of tables

| | |
|---|-----|
| Table 1.1 Carbon-based materials properties used in EDLCs. | 38 |
| Table 1.2 Metal oxide materials for pseudocapacitors electrodes [14, 30- 33]. | 40 |
| Table 5.1 Fe ₃ O ₄ -CNT samples used in this investigation. | 124 |
| Table 6.1 Detailed results for CVs, the average C _s , C _m versus scan rates capacitance vs. scan rate for (a) M-CB-MWCNT, (b) M-FH-CB-MWCNT, (c) M-PV- MWCNT,(d) M-AA-MWCNT and (e) M-CP-MWCNT electrodes. | 151 |
| Table 6.2 Detailed results for GCD, the average C _s , C _m versus scan rates capacitance vs. scan rate for (a) M-CB-MWCNT, (b) M-FH-CB-MWCNT, (c) M-PV- MWCNT,(d) M-AA-MWCNT and (e) M-CP-MWCNT electrodes. | 152 |

List of abbreviations and symbols

| | |
|--------------------|--|
| A, mA (unit) | Ampere, milliamp |
| AC, ACNTs, AMWCNTs | Activated Carbon nanotubes |
| AM | Active mass |
| C_s | Areal normalized specific capacitance |
| C_m | Mass normalized specific capacitance |
| C_s' | Real component of complex capacitance |
| C_s'' | Imaginary component of complex capacitance |
| CA | Caffeic acid |
| CAS | Cholic acid sodium salts |
| C | Capacitance |
| C° | Temperature in Celsius |
| C_{Cell} | Overall cell capacitance |
| Cdl | Capacitance from double layer |
| C_{+ve} | Capacitance of positive electrode |
| C_{-ve} | Capacitance of negative electrode |
| CB | Celestine blue dye |
| CNT | Carbon nanotubes |
| CV | Cyclic voltammetry , cyclic voltammogram |
| CCP | Chemical co-precipitation |
| CP | M-cresol purpule |
| C, μC (unit) | Coulomb, micro coulomb |
| DI | Deionized |
| DM-CNT | Dried magnetite carbon nanotubes |
| DLS | Dynamic light scattering |
| EDLC | Electrochemical double layer capacitor |
| EIS | Electrochemical impedance spectroscopy |
| ESs | Electrochemical supercapacitors |
| EM-CNT | Extracted magnetite carbon nanotubes |

| | |
|--------------------|---|
| ESR | Equivalent series resistance |
| EDX | Energy dispersive x-ray spectroscopy |
| EPD | Electrophoretic deposition |
| ϵ_0 | Permittivity in vacuum |
| ϵ_r | Permittivity between electrodes |
| E | Electrode potential |
| E° | Standard electrode potential |
| E _{total} | Total energy stored in a capacitor |
| F | Farad , Faraday constant |
| FDCNT | Fe ₃ O ₄ -decorated CNT |
| <i>f</i> | Frequency |
| FTIR | Fourier-transform infrared spectroscopy |
| g, mg, µg (unit) | Gram, milligram, microgram |
| Gamma (γ) | Relative mass ratio (nanoparticle/MWCNTs) |
| h (unit) | Hours |
| Hz (unit) | Hertz |
| I | Current |
| IEP | Isoelectric point |
| ILQs | Ionic Liquids |
| IHP | Inner Helmholtz plane |
| K (unit) | Temperature in Kelvin |
| L (unit) | Liter |
| MWCNTs | Multi-walled carbon nanotubes |
| M-CNTs | Magnetized carbon nanotubes |
| MNP | Magnetic nanoparticles (Fe ₃ O ₄) |
| M | Molar concentration |
| MOPC | Magnetically ordered pseudocapacitors |
| m | Mass of active materials |
| m (unit) | Meter |
| NPs | Nanoparticles (Fe ₃ O ₄ or NiFe ₂ O ₄) |

| | |
|---------------------|---|
| OHP | Outer Helmholtz plane |
| PELLI | Particle extraction through liquid-liquid interface |
| PVB | Polyvinyl butyral |
| PM | Physical mixing |
| pH | Degree of acidity ($-\log H^+$) |
| PC | Propylene carbonate |
| Q | Charge stored |
| R | Resistance |
| s (unit) | Second |
| SCE | Saturated calomel electrode |
| SDS | Sodium dodecyl sulfate |
| SEM | Scanning electron microscopy |
| S_p | Power density |
| S_E | Energy density |
| STEM | Scanning transmission electron microscope |
| SWCNT | Single-walled carbon nanotube |
| T | Temperature |
| TEM | Transmission electron microscope |
| TEMABF ₄ | Triethylmethylammonium tetrafluoroborate |
| δ_M | Relative mass ratio (material/current collector) |
| UPD | Under potential deposition |
| V (unit) | Volt |
| V | Voltage |
| XRD | X-ray diffraction |
| Z' | Real part of impedance |
| Z'' | Imaginary part of impedance |

Chapter 1

Literature review

1.1 Introduction

A rapid increase in the human population causes many economic problems; one of them is the enormous rate of energy consumption compared to the limitations of sources. The reason for that could be climate change, pollution, and the depletion of natural energy resources such as fossil fuels [1].

Recently, research and development organizations are trying to discover new economic energy sources and develop efficient mechanisms for the existing energy storage systems [2].

Classifications of the energy storage systems can be divided into chemical, electrochemical, thermal, and mechanical systems [1, 2]. The traditional electrochemical energy storage systems (batteries and capacitors) are used for many daily important applications, like electronic devices, electrical systems, and hybrid vehicles. These traditional systems have some imperfections, such as the large size of the device, operational time limitations, and performance range [2]. Therefore, trying to meet the requirements for future aims, many effective technologies for electrochemical energy storage and conversion systems have become a concern for all developers and inventors, especially the electrochemical supercapacitors with different types, as shown in (Figure 1.1) [3].

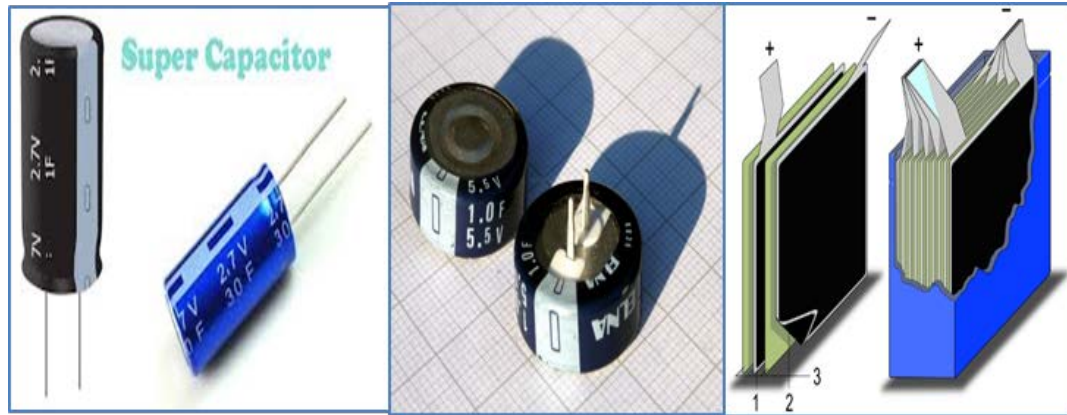


Figure 1.1 Different designs of electrochemical supercapacitors (ESs) [3].

The electrochemical supercapacitor (ESs) is one of the modern energy storage systems that offer a balance between power and energy densities, in which the energy storage mechanism depends on one of two main mechanisms; electrostatic double layer (EDLCs) and pseudo capacitance [3]. The classification of the (ESs) can be presented as (EDLCs), Pseudo, and hybrid capacitors depending on the type of the used active materials beside the working mechanism. To optimize (EDLCs) and pseudocapacitor's advantages, such as high conductivity, stability, and relatively high performance; this research investigates the hybrid asymmetric supercapacitors using different composites/fabrication techniques. These investigations include composites of magnetized carbon nanotubes $\text{Fe}_3\text{O}_4/\text{MWCNTs}$ (M-CNTs) and nickel ferrite carbon nanotubes $\text{NiFe}_2\text{O}_4/\text{MWCNTs}$ using different synthesizing methods and a higher mass ratio of (nanoparticles /MWCNTs).

1.2 Fundamentals

Power and energy densities, cyclic stability, and charge-discharge efficiency are considered important parameters that govern an energy storage device's performance. The relation between power and energy densities vs discharge time is illustrated in the Ragone plot shown in (Figure 1.2) [5].

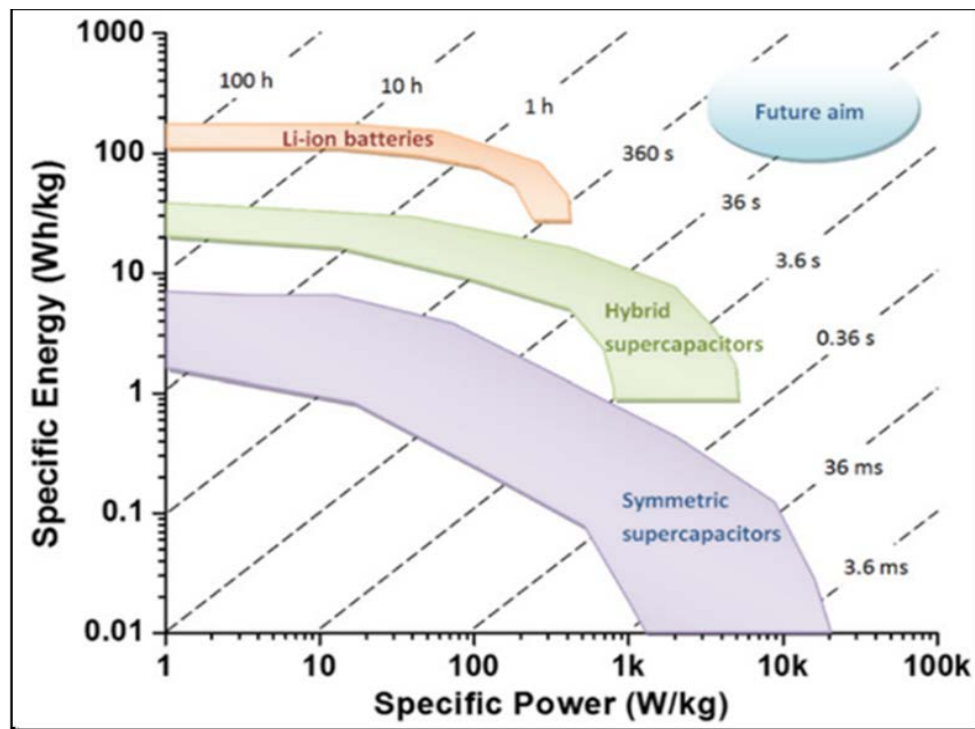


Figure 1.2 Ragone plot for the main energy storage devices, relative discharge time in the dashed line [5].

To further explain fundamentals and different parameters that govern the (ESs), the conventional electrostatic capacitor is shown in (Figure 1.3). It consists of two conductive current collector plates (electrodes), separated by an insulating dielectric plate. Initially, the electrodes are electrically neutral, and at the point of applying the voltage, the polarization

and re-orientation processes happen to the dielectric material where the opposite charges accumulate on the surfaces of each plate and the produced electric field allows the capacitor to store energy [6].

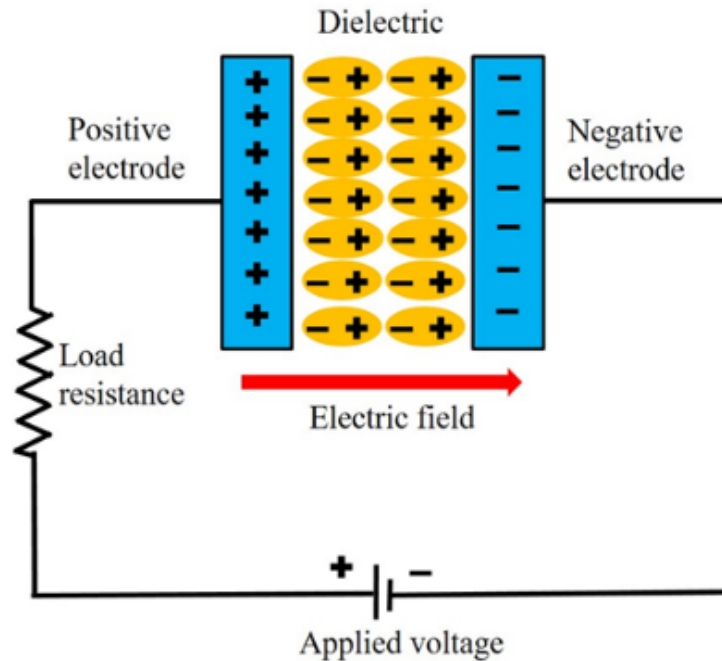


Figure 1.3 Schematic of simple conventional electrostatic capacitor [6].

One of the main advantages of the ideal capacitor is the stability of the capacitance value C (Farad). This value is defined by the relationship of accumulated charges Q on a certain electrode and the applied voltage V between the two electrodes that could be calculated by Eq. 1.1 [7].

$$Q = C V \quad (\text{Eq. 1.1})$$

Where Q is the charge stored, V is the voltage across the plates, and C is the capacitance of the dielectric capacitor.

For a typical capacitor, C is proportional to the ratio of the surface area A of each electrode and the distance between the electrodes d , the proportionality constant is the permittivity and it can be demonstrated as follows:

$$C = \epsilon_0 \epsilon_r \frac{A}{d} \quad (\text{Eq. 1.2})$$

Where ϵ_0 content represents the permittivity of insulating material in the free space (vacuum) (F m^{-1}) and ϵ_r represents the permittivity of it between the electrodes [7, 8]. Two important parameters can be used to identify the performance of a capacitor, the power and energy values, which can be expressed in the term of specificity (mass/volume) as power and energy densities. Equations 1.3 and 1.4 can express the stored energy E and power P of a capacitor and it is obvious that the stored energy depends on the capacitance and the voltage between the plates.

$$E = \frac{1}{2} CV^2 \quad (\text{Eq. 1.3})$$

$$P = IV = \frac{V^2}{4 \times ESR} \quad (\text{Eq.1.4})$$

An electric circuit with external load resistance R in series can be used to calculate the power of a capacitor, in addition to internal resistance, depends on various components of the capacitor, such as dielectric material, current collector, and the electrodes, which represented in the form of equivalent series resistance (ESR) [7, 8]. Conventional capacitors have a high power density relative to the electrochemical supercapacitors (ESs), while (ESs) have a much higher energy density that attracts more people's attention [7, 8].

1.3 Classifications of electrochemical supercapacitors (ESs)

Electrochemical supercapacitors (ESs) are one of the modern energy storage systems that offer a balance between power and energy densities. Figure 1.4 shows the classifications of the (ESs), in which the (ESs) can be divided into three main categories electrostatic double-layer (EDLCs), Pseudo, and hybrid capacitors and that is according to the type of active material beside the mechanism of the energy storage. These categories depend on one of the two main mechanisms of storage mechanisms EDLCs / pseudocapacitance or in most cases a combination of them [9].

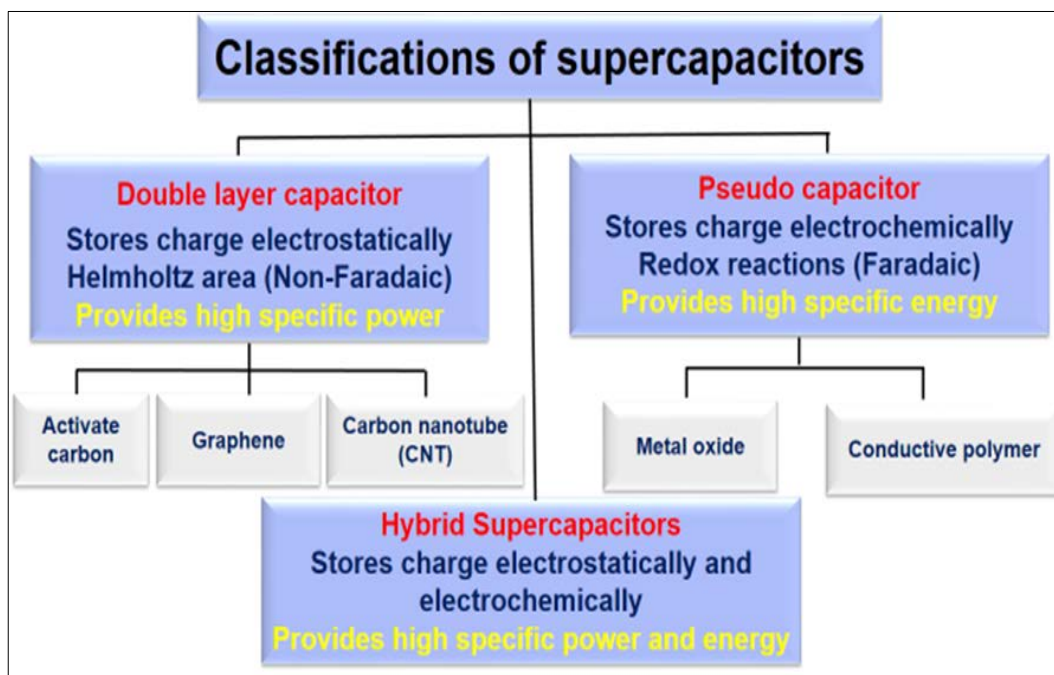


Figure 1.4 Classifications of electrochemical supercapacitors (ESs).

According to the nature of the active materials and the mechanism of the energy storage, (ESs) can be classified as symmetric or asymmetric hybrid. The symmetric supercapacitors consist of the same kind of materials or the same mechanism of the energy storage system

and the asymmetric one depends on combinations of different energy storage mechanisms or material types [10].

1.3.1 Electrostatic double layer capacitors (EDLCs)

Electrostatic double-layer capacitors (EDLCs) are the main commercial product of (ESs), in which the storage mechanism relies on the separation of charge in a Helmholtz double layer at the interface between the surface of a current collector electrode and an electrolyte [9]. The most popular (EDLCs) depend on the fabrication of electrodes with an active mass loading of the carbon-based materials, such as carbon nanotubes, graphene, and activated carbon. These porous carbon materials usually have surface areas in the range of 500-3000 $\text{m}^2 \text{g}^{-1}$, and theoretically, these electrodes have theoretical C around 15-50 ($\mu\text{F cm}^{-2}$) or above 500 F g^{-1} in aqueous electrolytes. However, the obtainable capacitances for carbon-based materials are often below 50 F g^{-1} due to limited electrolyte access into pores and low electrical conductivity [11].

Despite the small capacitance of these types of active materials, the (EDLCs) mechanism is a neat electrostatic action and there is no phase change, which allowed them to have a remarkably long cyclic life [12]. The dependence on these materials is due to their high surface area, good conductivity, and ability to be functionalized with other materials, in addition to their advantage of enhancing the specific power. Figure 1.5 shows a simple schematic representation for symmetric (EDLCs) of pure carbon-based materials. It consists of a positive and a negative electrode immersed in an electrolyte, which offers a higher capacitance per volume using high surface area porous carbon materials as active materials [11,12].

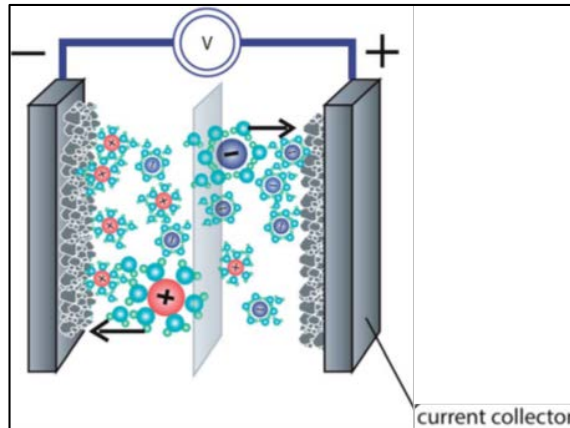


Figure 1.5 Schematic of EDLC [11].

The charge-discharge mechanism revealed from the pure electrostatic charges accumulation and separation at the electrode/electrolyte interface on both electrodes. Increasing the capacitance resulted from the declination of the potential through an interface layer and hence increasing the charges that are called double layer that is shown in (Figure 1.6) [3, 12].

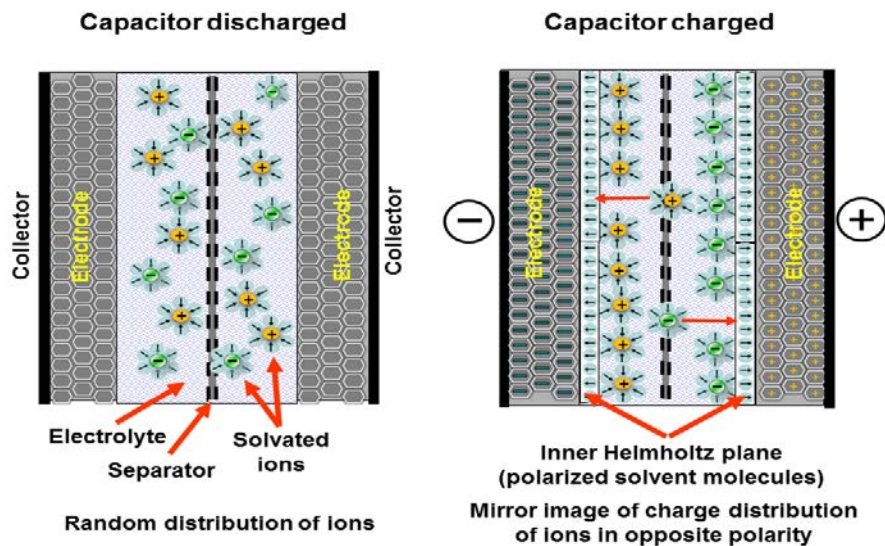


Figure 1.6 Schematics of EDLC during the charge-discharge cycles [3].

1.3.2 Electrochemical pseudocapacitors

Pseudocapacitors could be considered as the new approach for the development of the commercial products for (ESs) [13], in which the storage of the energy is achieved by a faradaic electron charge-transfer with redox reactions as shown in Figure 1.7 [3,14].

Pseudocapacitance with specifically adsorbed ions

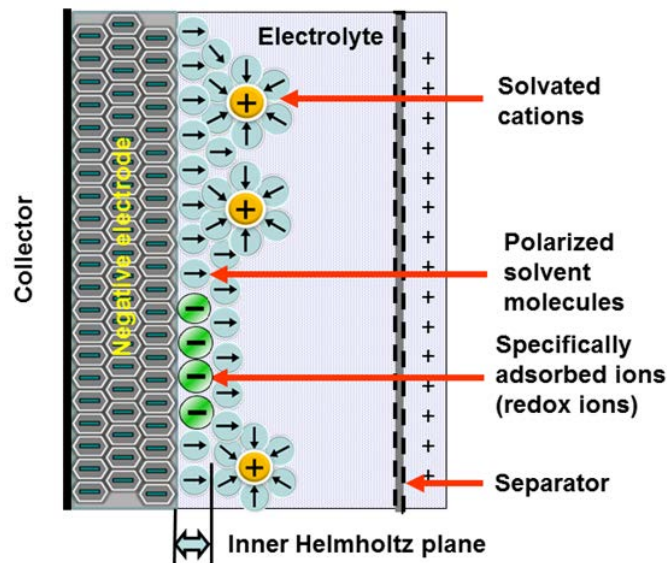


Figure 1.7 Schematic of mechanisms for pseudocapacitance [3].

The active materials for pseudocapacitors are redox materials with high specific energy storage capacities such as transition metal oxides and conductive polymers. Pseudocapacitors have many advantages, such as relatively higher energy density due to the principle that the faradaic process is normally slower than the non-faradaic process. Another advantage is the efficient cyclic stability and the poses of a fast charge-discharge cycle that makes them convenient for modern applications compared to conventional capacitors or batteries [10].

Figure 1.8 shows several faradaic mechanisms proposed by Conway, which can result in pseudocapacitive behavior for capacitors [10, 15-19]. The first one is under potential deposition (UPD), which occurs when metal ions form an adsorbed monolayer at a different metal surface well above their redox potential. The deposition of lead on a gold surface is a representative example of UPD. The second type is the redox pseudocapacitance, this occurs during the process of the electrochemical adsorption of ions on the surface or absorption near the surface of material accompanied by a faradaic charge transfer. Transitional metal oxide, such as Fe_3O_4 , NiFe_2O_4 , RuO_2 , Mn_3O_4 , MnO_2 , NiO , etc., as well as a conductive polymer, such as polyaniline and polypyrrole, are classified as the redox pseudocapacitive materials. The third one is the intercalation pseudocapacitance, which results from ion intercalation into the tunnels or layers of a redox-active material accompanied by a faradaic charge transfer but without crystallographic phase change [15].

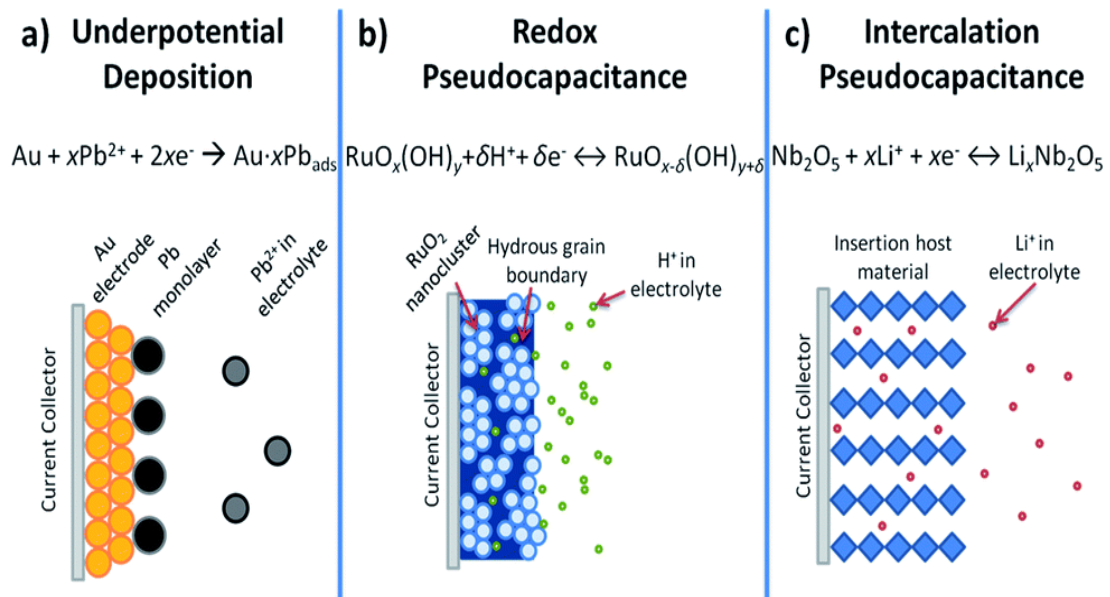


Figure 1.8 Various reversible redox mechanisms for pseudocapacitance [10].

1.3.3 Hybrid (asymmetric) supercapacitors

Typically, electric double-layer capacitors (EDLCs) and pseudocapacitors can be classified as symmetric supercapacitors as usually both positive and negative electrodes using the same type of material. However, to optimize the advantages of (EDLCs) and pseudocapacitors, recent researches tried to develop a combination between both types that released the newest category of the (ESs) named hybrid asymmetric supercapacitors [20]. The hybrid supercapacitors have relatively high specific energy as well as high specific power that fills the gap between the symmetric supercapacitors and Li-ion batteries. Figure 2.8 shows schematic structure and principles of hybrid asymmetric supercapacitor and illustrates electrostatic and electrochemical mechanisms of energy storage mechanisms [21].

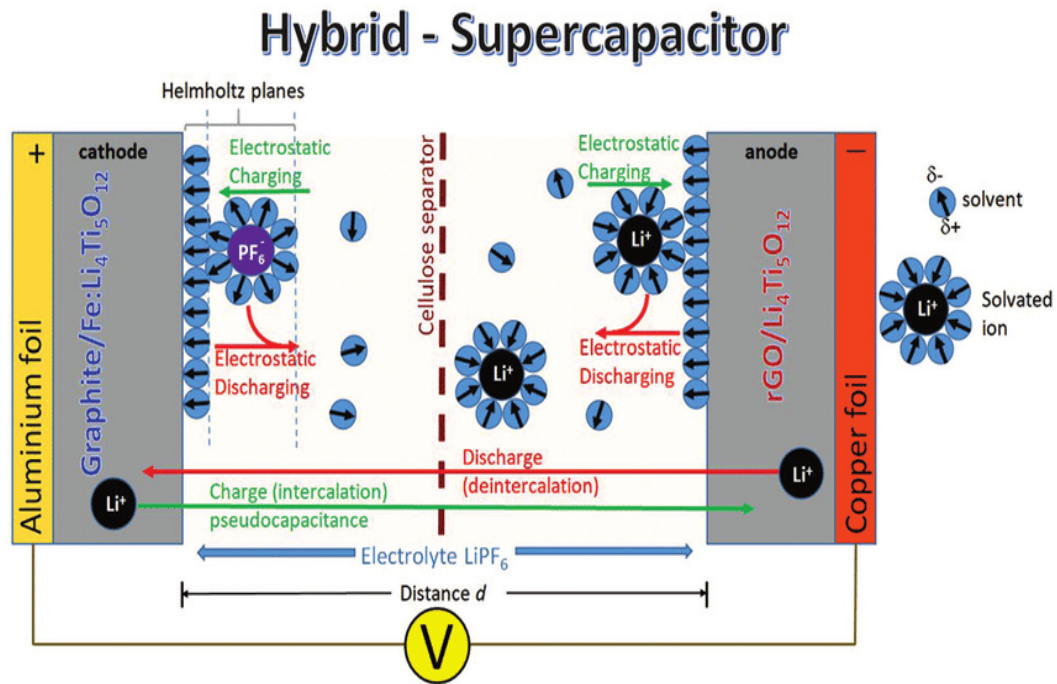


Figure 1.9 Schematic structure and principles of a hybrid asymmetric supercapacitor [21].

The charge storage based on the pseudo mechanism is not limited to the surface only but also to the near-surface region where ions can diffuse into the active materials. The pseudo mechanism involves reversible redox reaction (Faradaic) during the charging or discharging process, in which the charges pass through the electrode /electrolyte interface; thus, the slow faradic process hindered the power performance. Conversely, EDLCs, which are based on electrostatic charge storage mechanism (non-Faradaic), whereas the charges just accumulate at the electrode/electrolyte interface in EDLCs [22].

The fabrication of efficient devices mainly depends on asymmetric hybrid supercapacitors, which optimize both high energy and power densities. This performance could be reached by a combination of two different electrode materials for both electrodes to fabricate a device. For instance, the transition metal oxide/carbon-based and conductive polymer/carbon-based material. Consequently, this structure enlarges the overall cell potential and results in higher energy density as well as power density [14, 22].

1.4 Active materials for supercapacitors applications

Many composites were developed to fill the gap in the performance between the battery and conventional capacitors. In other words, the development of different composite materials that could exhibit combined energy storage mechanisms (EDLC/Pseudo) [22]


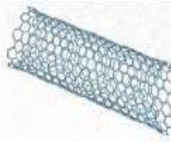
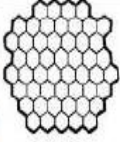

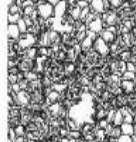

1.4.1 Carbon-based materials

It was mentioned that EDLCs performance is controlled by the structure and surface area of active materials. For example, carbon-based materials have some advantages such as high surface area, good conductivity, high thermal stability, magnificent

corrosion resistance, and controllable porous structure that make them excellent candidates as active materials in EDLCs and as additives in pseudocapacitors [23].

Table 1 is a summary of different carbon materials and their related properties for EDLCs, such as carbon nanotube, graphene, activated carbon, and graphite [24-27].

Table 1.1 Carbon-based materials properties used in EDLCs.

| Material | Carbon onions | Carbon nanotubes | Graphene | Activated carbon | Carbide derived carbon | Templated carbon |
|------------------------|--|--|--|---|--|--|
| Dimensionality | 0-D | 1-D | 2-D | 3-D | 3-D | 3-D |
| Conductivity | High | High | High | Low | Moderate | Low |
| Volumetric Capacitance | Low | Low | Moderate | High | High | Low |
| Cost | High | High | Moderate | Low | Moderate | High |
| Structure |  |  |  |  |  |  |

1.4.2 Redox-based materials

Compared to EDLCs, pseudocapacitors have a relatively higher capacity. Based on a redox reaction, the charges can accumulate both in an electrostatic way and in a faradaic reaction way [29, 30]

1.4.2.1 Conducting polymers

Conducting polymers have less pollution, easy fabrication and high conductivity, so they attract much attention in recent years. The popular conducting polymers are (i) polypyrrole (PPy), (ii) polyaniline (PAni), (iii) polythiophene (PTh), and (iv) poly(3,4-ethylene dioxythiophene) (PEDOT); Figure 1.10 shows their different molecular structures [31].

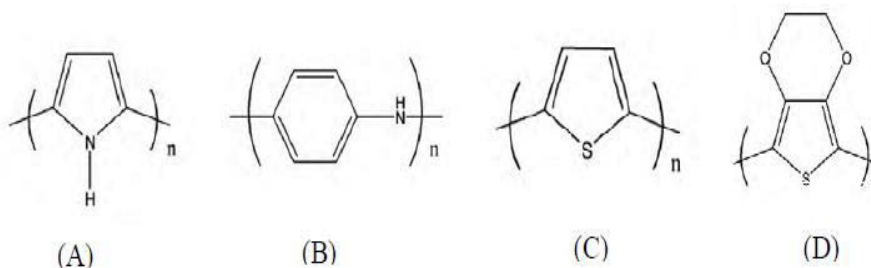


Figure 1.10 Various conducting polymer structures. (A) (PPy), (B) (PANi), (C) (PTh) and (D) (PEDOT) [31].

In the charge/discharge process, the charges are accumulated by the redox reaction-taking place in the bulk volume of the film, instead of just on the surface as the case in carbon. Therefore, the specific capacitance of (ESs) made by this kind of material is relatively high. However, there is a limitation of the conductive polymers that they can only be used within a rigid potential window [26].

1.4.2.2 Transition metal oxide materials

Table 1.2 below shows the common metal oxide materials for pseudocapacitors electrodes. It is obvious that RuO_2 has a high conductivity as well as a high capacitance. However, this kind of material is limited by its dangerous hazards and high cost. Thus, to replace RuO_2 , inexpensive and non-toxic materials such as manganese oxide (MnO_2), vanadium oxide (V_2O_5), magnetite (Fe_3O_4), and nickel oxide (NiO) have been explored as pseudocapacitive materials. Among the metal oxides, Fe_3O_4 is chosen as the electrode material for supercapacitors due to its added merits such as high theoretical specific capacitance (2299 F g^{-1}), large potential window (-1.2 to 0.25 V), natural abundance, low cost, less toxicity, and ferrimagnetic properties [32, 33].

Table 1.2 Metal oxide materials for pseudocapacitors electrodes [14, 30 - 33].

| Metal oxide | Potential range (V) | Theoretical capacitance (F/g) |
|------------------------------------|----------------------------|--------------------------------------|
| MnO₂ | 0.90 | 1380 |
| NiO | 0.50 | 2584 |
| Co₃O₄ | 0.45 | 3560 |
| V₂O₅ | 1.00 | 2120 |
| RuO₂ | 1.23 | 2200 |
| Fe₃O₄ | 1.45 | 2299 |
| Mn₃O₄ | 1.10 | 1450 |

1.5 Mass loadings of electrodes

Despite the numerous attempts on the fabrication of advanced transition metal oxide composite electrodes, poor conductivity is one of the biggest challenges for metal oxide electrodes to become a practical application. It was demonstrated in the literature that Fe₃O₄ based composites thin-film electrodes could exhibit close to the theoretical capacitance of 215 F g⁻¹; however, the mass loading of the electrode was merely 4.3 mg cm⁻² [32]. It was pointed out that increasing mass loadings of electrodes drastically reduced the capacitances. He et al. have shown that by increasing the mass loading of MnO₂-graphene nanocomposites from 0.1 to 9.8 mg cm⁻², the capacitances decreased from 440 to 150 F g⁻¹ [32]. Higher mass loadings also reduce the performance of electrodes at higher scan rates due to poor electrolyte access. Another factor is the ratio of active materials mass to current collector mass (R). For thin-film electrode with 5 mg cm⁻² mass loading, the R ratio is 3.11x10⁻⁵ [33]. As the mass loadings increase, the R ratio becomes larger and more practical. However, there is a balance between a high R ratio and high capacitances.

Gogotsi et al. have suggested that a practical mass loading of electrodes should be above 10 mg cm⁻², such that the results are comparable on the Ragone plot [5]. Therefore, new current collectors and strategies must be employed to increase the R_m ratio and preserve capacitive performance.

1.6 Dispersion of metal oxides

It was mentioned that high active surface area is an important factor in achieving high capacitance. However, in the colloidal fabrication of metal oxide nanoparticles, agglomeration of particles becomes one of the major challenges to utilize all surface areas. The driving force of agglomeration is the minimization of the surface energy of particles to be thermodynamically stable [34]. The drying procedure also promotes agglomeration due to the occurrence of condensation reactions between surface hydroxyl groups on the particles. When a solid particle emerges in solution, a surface charge will develop by either adsorption and desorption of ions or dissociation and substitution of surface charged species. Once the surface charge is developed, electrostatic repulsion will segregate positively and negatively charged species within the vicinity. Depending on the pH of the electrolyte, the surface of particles can be positively or negatively charged by adsorption of charge determining ions given by Eq.1.5 and Eq.1.6.

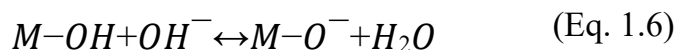
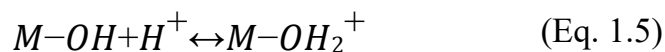


Figure 1.11 shows the general surface charge vs the pH value and the isoelectric point (IEP), where the concentration of charge determining ions correspond to a charge-neutral surface and the IEP is different for various materials. At pH above the IEP, the reaction in Eq.1.6 dominates and yields a negatively charged surface, which is the case for the CCP synthesis of MNP Fe_3O_4 in DI water at pH 9. The surface charge developed by immersing particles in solutions can stabilize the suspension to a certain extent, and it is commonly referred to electrostatic stabilization [34].

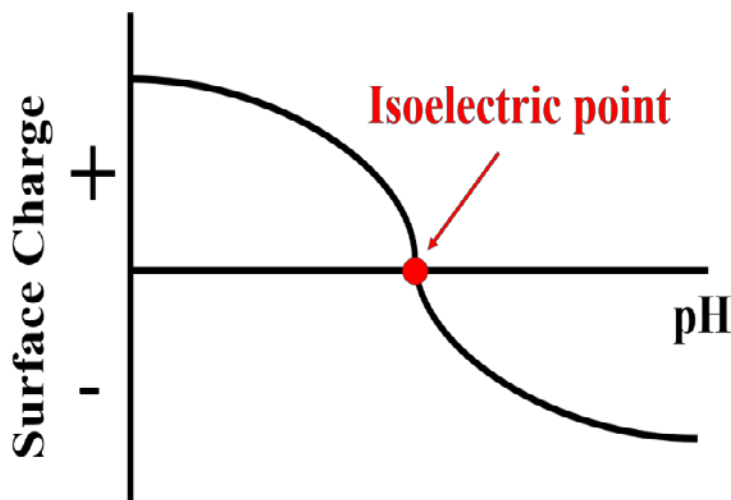


Figure 1.11 Schematic of surface charge of particles as a function of pH [34].

In many cases, pure electrostatic repulsion is insufficient to provide good stabilization of colloids. Therefore, other stabilization techniques such as steric stabilization are employed. Steric stabilization typically uses polymers to act as a diffusion barrier for growth species, which can narrow the size distribution of particles as well as dispersion of colloids. There are three types of polymers based on their interactions with particles, anchored polymers, adsorbing polymers, and non-adsorbed polymers [34, 35].

Anchored polymers are polymers that interact with particles irreversibly by one end only; adsorbing polymers adsorbed weakly on particles surface at random points of the polymers, and non-adsorbed polymers do not interact with particles surface and do not provide any steric stabilization. Anchored polymers are superior compared to adsorbing polymers, as adsorbing polymers can adsorb and bridge to other particles [36, 37]. Therefore, strong interactions with particles surface are an ideal property for the dispersant of particles. It has been demonstrated by Liu et al. that organic molecules with catechol group can provide strong adsorption to metal oxide particles for electrophoretic deposition (EPD). The investigation involved the analysis of carboxylic acids with different positions and amounts of hydroxyl groups on the aromatic ring. The acids that were investigated were caffeic acid (CA), trans-cinnamic acid (TCA), *p*-coumaric acid (PCA), and 2,4 di-hydroxycinnamic acid (DCA) and their chemical structure is shown in Figure 1.12. CA was the only acid that allowed the successful deposition of MnO₂ particles using EPD [34, 35]. CA belongs to the catechol family, which contains an aromatic ring with two adjacent hydroxyl groups. Similar molecules can be found in protein macromolecules of mussels, containing catechol amino acid L-3-4dihydroxyphenylalanine (DOPA), adsorbing strongly to different substrates under wet conditions [35, 36].

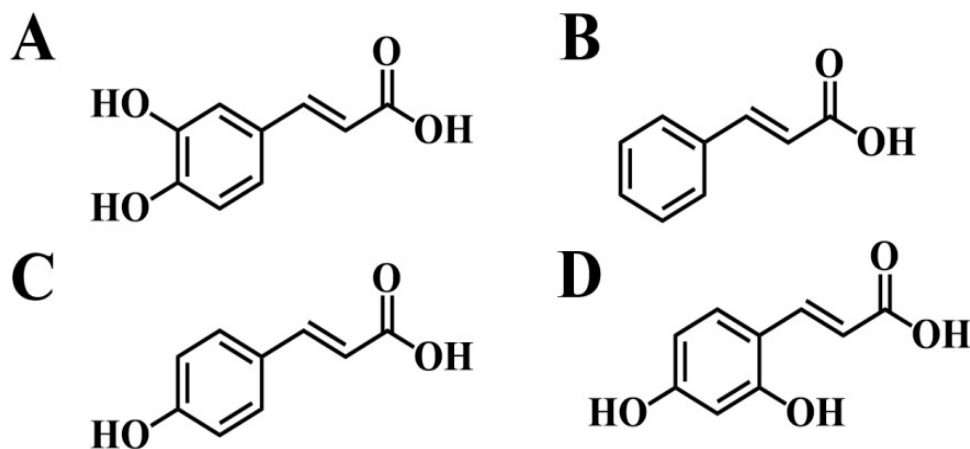


Figure 1.12 Chemical structures of (A) CA, (B) TCA, (C) PCA, and (D) DCA [35].

Ata et al. have suggested a mechanism to describe superior adhesion of dispersants to metal oxide surface in which the strong adsorption to metal oxide particles was attributed to strong chelating and bridging mechanisms [37]. Figure 1.13 shows some multifunctional dispersing agents; some of them are positively charged molecules and others are negatively charged. The positively charged ones such as 6-phosphonohexanoic acid (PHA) and pyrogallol red (PGR) could be used in the process of MnO_2 dispersion with advanced adsorption mechanism, and the negatively charged like azure A chloride (AZA) and Nile Blue chloride (NB) that could be used in dispersion with advanced adsorption mechanism for MWCNTs and Fe_3O_4 [37]. The presence of adjacent hydroxyl groups is crucial to strong bonding with metal oxide surface and for this reason, TCA, PCA, and DCA were unable to provide strong adhesion [35, 37].

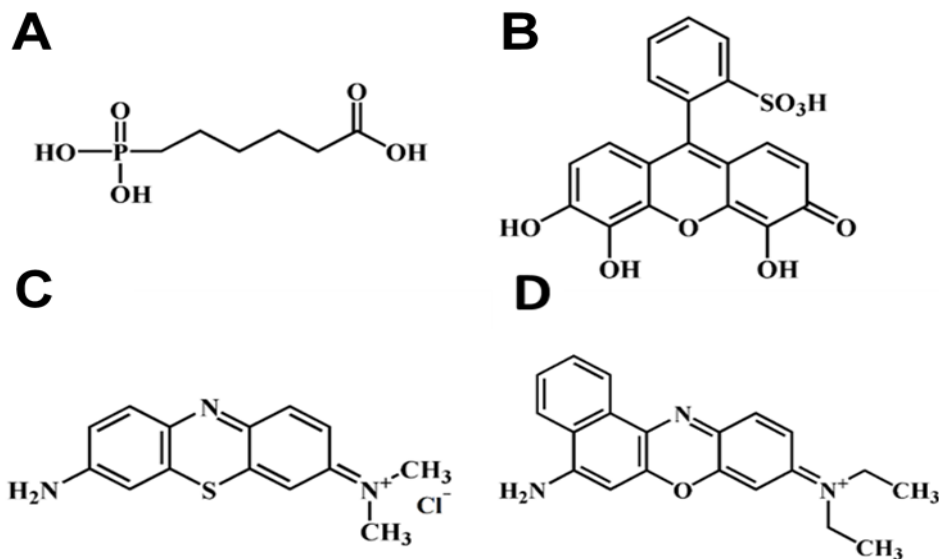


Figure 1.13 Chemical structures of (A) PHA, (B) PGR, (C) AZA, and (D) NB [35,37].

1.7 Dispersion of MWCNTs

Carbon nanotubes (MWCNTs) tend to form bundles due to Van der Waals attractions and show poor solubility in aqueous and organic solvents [38,39]. There are several methods to disperse MWCNTs, and they typically involve covalent and non-covalent surface modifications. Covalent surface modifications involve surface functionalization by acid oxidation [40]. Aviles et al. have performed acid oxidation for MWCNTs using different oxidants and concentrations, such as H₂SO₄ and HNO₃. They have demonstrated that HNO₃ was able to oxidize the MWCNTs surface by introducing oxygen-containing functional groups on the surface [39]. The presence of functional groups led to a reduction of Van der Waals attractions between bundles and allowed separation and dispersion of MWCNTs. However, acid oxidation can reduce the length of MWCNTs and damage the surface continuity, which in turn degrades the mechanical and

electrical performance of MWCNTs [41]. Another approach to disperse MWCNTs is by non-covalent surface modifications, which avoid the performance degradation caused by surface functionalization [42]. Non-covalent surface modifications typically involve the use of polymers and head-tail surfactants as dispersing agents. The driving force of adsorption is the hydrophobic interactions of MWCNTs surfaces with long hydrocarbons chain in polymers and head-tail surfactants, and the hydrophilic groups give rise to dispersion [42]. However, it is difficult to avoid polymer wrapping of MWCNTs dispersed using polymers, resulted in an insulating polymeric layer on MWCNTs. Moreover, it was demonstrated that a large quantity of head-tail surfactants is required to achieve dispersion using sodium dodecyl sulfate (SDS) as a model of head-tail surfactant. Therefore, there is a need for efficient dispersants for MWCNTs, which do not compromise the structure and chemical integrity of MWCNTs [40-42].

1.8 Electrolytes for electrochemical supercapacitors (ESs)

One of the most valuable parameters in the ESs applications is the energy density enhanced electrolytes [43, 44]. The progress in the electrolytes could be considered as essential as the improvement of electrode materials because the potential window of electrolyte directly enhances the energy density [43].

In addition to the influence on energy density, the properties of electrolytes are contributed to the overall performance of ESs. Figure 1.14 illustrates the relation between different properties of electrolytes and some parameters that could judge the performance of ESs, such as capacitance, power density, etc. [43, 45].

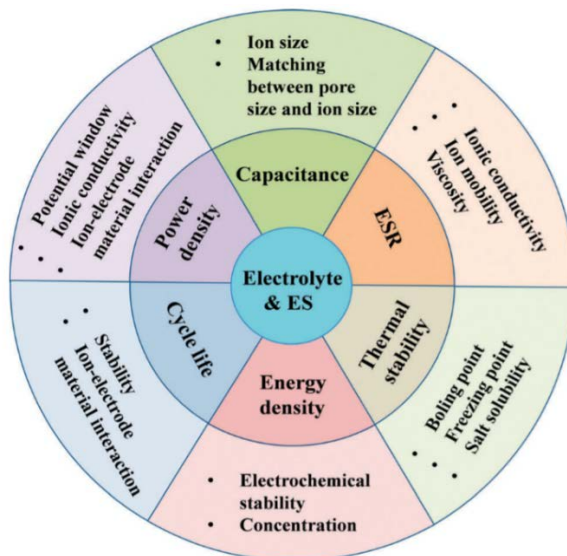


Figure 1.14 Effects of the properties of the electrolyte on the ESs performance [43].

Electrolytes could be classified into three main types; aqueous electrolytes, organic electrolytes, and ionic liquids-based electrolytes [43, 46]. Aqueous electrolytes and organic electrolytes are the most common electrolytes for ESs applications [43, 47].

1.8.1 Aqueous electrolytes

There are some advantages of the aqueous electrolytes compared to other types (organic – ionic) that make this type of electrolytes are widely used, such as the lower resistance, low cost, higher conductivity, and the high solubility of salts [43, 44, 48]. Normally, the resistivity of aqueous electrolytes is lower than that of organic electrolytes (for example, 1M H₂SO₄ has a conductivity of 0.8 S cm⁻² at 25 °C), which is beneficial for the ESR [43, 44]. The main deficiencies of aqueous electrolytes are their small electrochemical stable potential window, which results in thermodynamic water decomposition at 1.229 V and low over potential, hydrogen evolution at the negative electrode with oxygen evolution at

positive electrode voltage that limits the window of aqueous electrolytes to around 1.2 V [43,48]. As shown in Figure 1.15, developments could extend the voltage window successfully was extended to 1.6 - 2.2 V by indicates that the asymmetric cell can be designed by choosing two different materials with different integrated potential voltage windows [43,46, 48].

The main divisions of aqueous electrolytes are neutral, acidic, and alkaline solutions. Electrolytes such as Na_2SO_4 , NH_4Cl , H_2SO_4 , KOH , and NaOH are mostly used in ESs applications due to high conductivity and ion transport mechanisms [48]. Neutral electrolytes are suitable for hybrid ESs with a wide voltage window. Furthermore, neutral electrolytes could be considered as a lower environmentally hazards assessment and low cost compared to acidic and alkaline. Among these electrolytes, Na_2SO_4 has been considered as the promising candidate for pseudocapacitors electrodes [44,47,48].

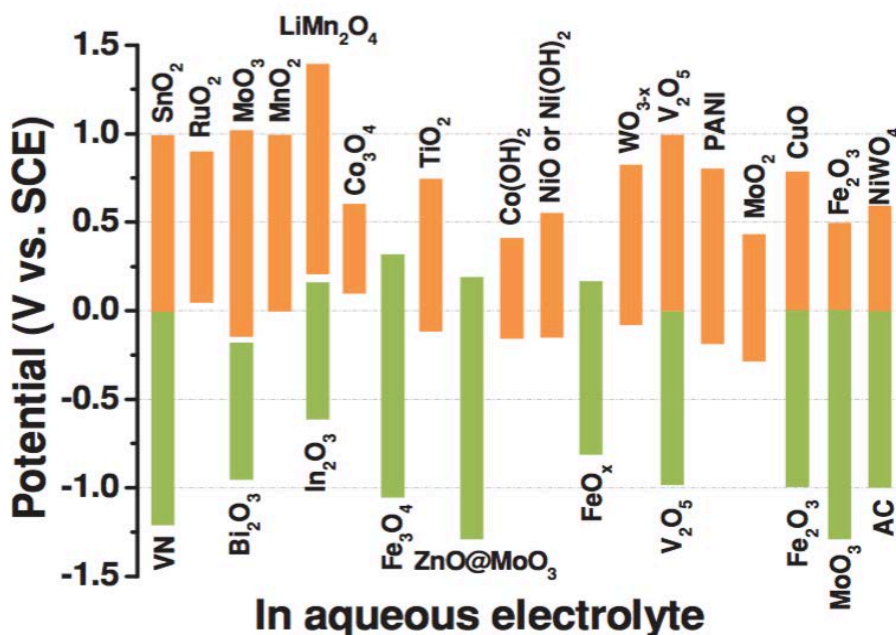


Figure 1.15 Potential windows of various electrode materials in aqueous electrolyte [48].

1.8.2 Organic electrolytes

The electrochemical performance of ESs that utilizes organic electrolytes is relying on the ion size, viscosity, conductivity, and electrochemical stability of the voltage window of the electrolyte [43]. In the presence of organic electrolytes, the ESs performance provides a relatively higher operation voltage window of about (2.2-2.8V) compared to aqueous electrolytes; therefore, the overall performance by exploiting the organic electrolytes shows enhanced energy density [43, 44]. However, ESs based on organic electrolytes obtained higher resistivity (20-60 Ω), low conductivity, and higher cost [43, 44, 47]. Propylene carbonate (PC) and triethylmethylammonium tetrafluoroborate (TEMABF₄) are the most commonly used solvents. PC-based electrolytes are considered lower in the environmental hazards and can contribute to the conductivity and the voltage window as well [43, 47].

1.8.3 Ionic liquid electrolytes

Ionic liquids (ILQs) are salts that exist as liquid at temperatures below 100°C and composed of a combination of organic cations and organic/inorganic anions. They are promising candidates for ESs because of their high thermal and chemical stability, non-flammable and non-corrosive properties, wide voltage window (~3.5–6 V), higher ionic conductivity relative to the organic electrolyte, and non-toxicity [49]. Ionic liquids (ILQs) promotes higher energy density because of the wider voltage range. Moreover, the high ionic concentration of (ILQs) has possibly reduced the electrolyte consuming problem, which significantly improved capacitor performance. Despite all these advantages, ILQs are too expensive for commercial applications and they are also hygroscopic that limits the handling of them and must be handled in the inert atmosphere [50].

Chapter 2

Problem statement and objectives

2.1 Gaps in the field of asymmetric hybrid supercapacitors

Based on the literature review, some gaps and problems have been found in the application of electrochemical supercapacitors that need more studies, especially the asymmetric hybrid type. We could summarize that, some of those problems are related to the structure of active materials and others to the design of the electrodes and devices.

2.1.1 Difficulties for dispersion of MWCNTs and agglomeration of MNPs

Carbon nanotubes (MWCNTs) have high relative conductivity and large surface area; however, their low specific capacitance limits their performance within the (ESs) [51]. On the other hand, MNPs such as NiFe_2O_4 and Fe_3O_4 could be considered as one of the most pseudocapacitive materials with high theoretical specific capacitance but poor electronic conductivity [51,52].

To optimize the advantages MNPs/MWCNTs composites in (ESs) application, NPs and MWCNTs particles should be as homogeneous as possible in addition to the reduction of the agglomeration of the particles [52,53]. Agglomeration of particles reduces the electrochemical performance by hinder the diffusion of ions into the electrodes. That agglomeration can be formed during the drying step of the composites, in addition to the presence of MWCNTs that always tend to aggregate easily [54,55]. Particle aggregation is governed by the reduction in particle surface area and condensation of the surface OH groups [54].

To address these problems, some attempts have demonstrated improvements and achieved high capacitances comparable to theoretical capacitances [33]. Several works have been focused on the covalent modification by generating acidic groups on the surface of MWCNTs to disperse them electrostatically and that's through the oxidation of MWCNTs in strong acids [55]. Non Covalent functionalization methods are also utilized to disperse MWCNTs [56]. However, these strategies not only generate defects to MWCNTs but also reduces their mechanical properties, electronic conductivity and result in fractures [19, 20]. Therefore, new efficient processing techniques should be developed to fabricate electrodes with reduced agglomerated particles [56, 57].

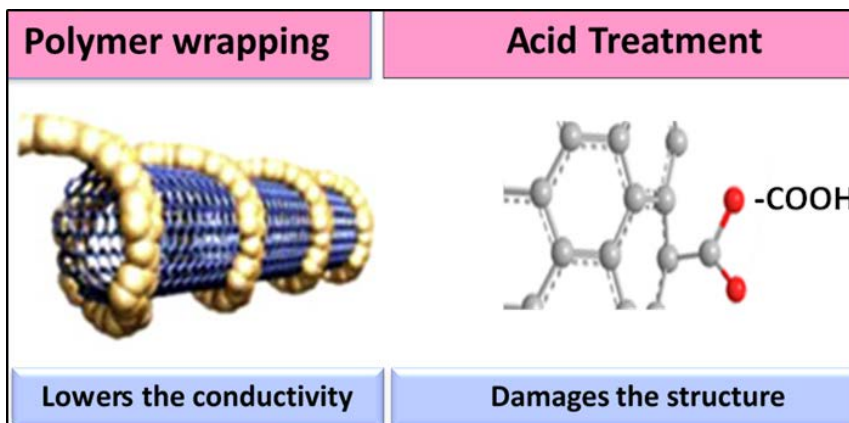


Figure 2.1 Schematic for surface modifications of MWCNTs [56].

2.1.2 Low performance at high active mass loading

The success in the supercapacitor technology developments depends on the ability to utilize high specific capacitance of advanced materials with high active mass loadings [58]. The important task is to achieve good electrochemical performance at a high ratio of the active material mass to the current collector mass (δ_M) [58, 59].

Metallic current collectors offer the benefits of high conductivity and low contact resistance [58-60]. However, the typical δ_M values for 1-5 mg cm⁻² films of active materials impregnated in metal foil current collectors lie below 0.01- 0.02.

Figure 2.2 shows the CV profile for asymmetric device which shows the effect of increasing the active mass loadings [33]. Significantly, higher active mass loadings and (δ_M) values are required for practical applications but without the limitation of decreasing the capacitance performance. The area normalized capacitance is another important parameter for the characterization of capacitor electrodes with high active mass loadings, especially for practical applications [8]. A high area normalized capacitance must be achieved with a low electrical resistance of the electrodes. Therefore, new current collectors and techniques should be developed to achieve high performance at high active mass loadings [33].

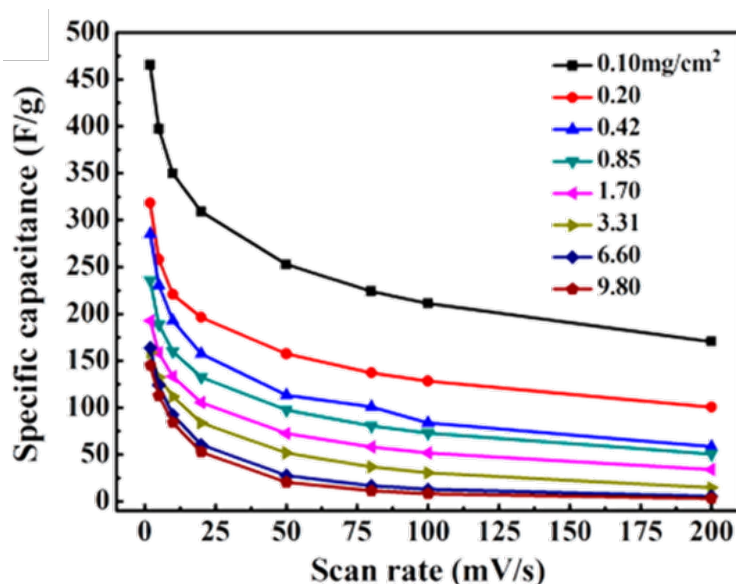


Figure 2.2 CV profile for asymmetric device shows the effect of increasing the active mass loadings [33].

2.1.3 Low capacitance of negative electrodes (unmatched capacitance)

In recent years, significant progress was achieved in the development of positive electrodes for supercapacitor devices [61]. However, the capacitance of negative electrodes is significantly lower compared to positive ones [62]. As a typical material for the positive electrode, MnO_2 provides a high specific theoretical capacitance of 1380 F g^{-1} [63]. However, typical negative electrode materials such as activated carbon and Fe_2O_3 have very low capacitance for around 100 F g^{-1} [64, 65]. As a result, the total device capacitance is limited by the low capacitance of negative electrodes as shown in (Figure 2.3) [62]. So advanced negative electrodes with new active materials such as magnetite (Fe_3O_4) that have high specific capacitance should be developed, magnetite has high theoretical specific capacitance (2299 F g^{-1}), a large potential window (-1.2 to 0.25 V), and a better cyclic stability in the range of negative electrodes [14, 65].

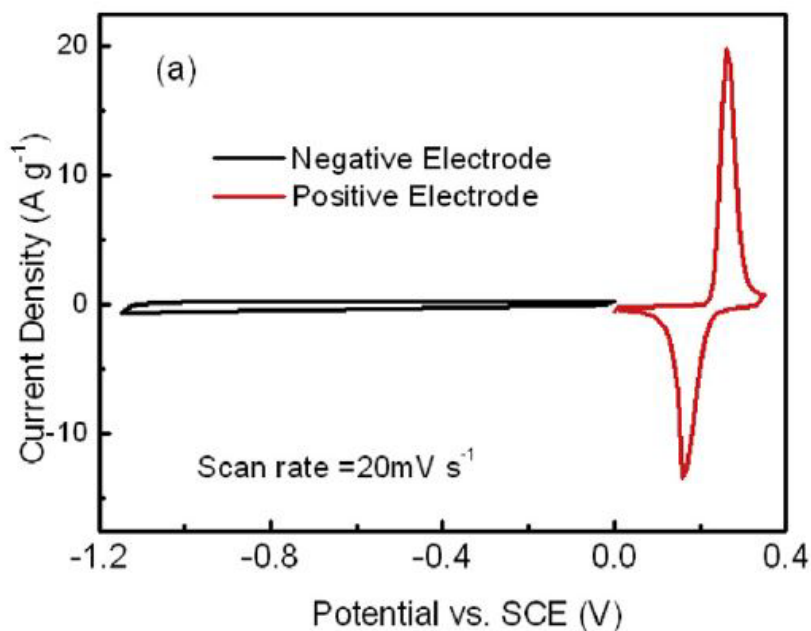


Figure 2.3 CV profile for an asymmetric device shows the unmatched capacitance [62].

2.2 Objectives

Our objectives toward addressing the main problems in the (ESs) field are as follow:

- Long term:
 - Development of asymmetric hybrid supercapacitor electrodes and devices with enhanced performance at high active mass loading.
- Short term:
 - Development of advanced composites materials (Fe_3O_4 - MWCNTs) and (NiFe_2O_4 - MWCNTs) for supercapacitors negative electrodes.
 - Development of advanced colloidal methods for the fabrication of composite materials for supercapacitors.
 - Development and testing of advanced asymmetric devices with large, stable voltage window.

Chapter 3

Methodology and experimental work

3.1 Synthesis of the M-CNTs by chemical co-precipitation (CCP) and liquid-liquid extraction method (PELLI)

Figure 3.1 shows the schematic diagram for the synthesis steps of Fe_3O_4 -ACNTs (M-CNTs) composite materials using the liquid-liquid extraction method [62]. The adsorption depends on the electrostatic interaction and chemical heterocoagulation. Palmitic acid (PA) has been used as an extractor that depends on chemical heterocoagulation (chelation or bridging) through the specific chemical group (carboxylic group) with the metal ions of the M-CNTs that were precipitated from their salts by using the chemical co-precipitation (CCP).

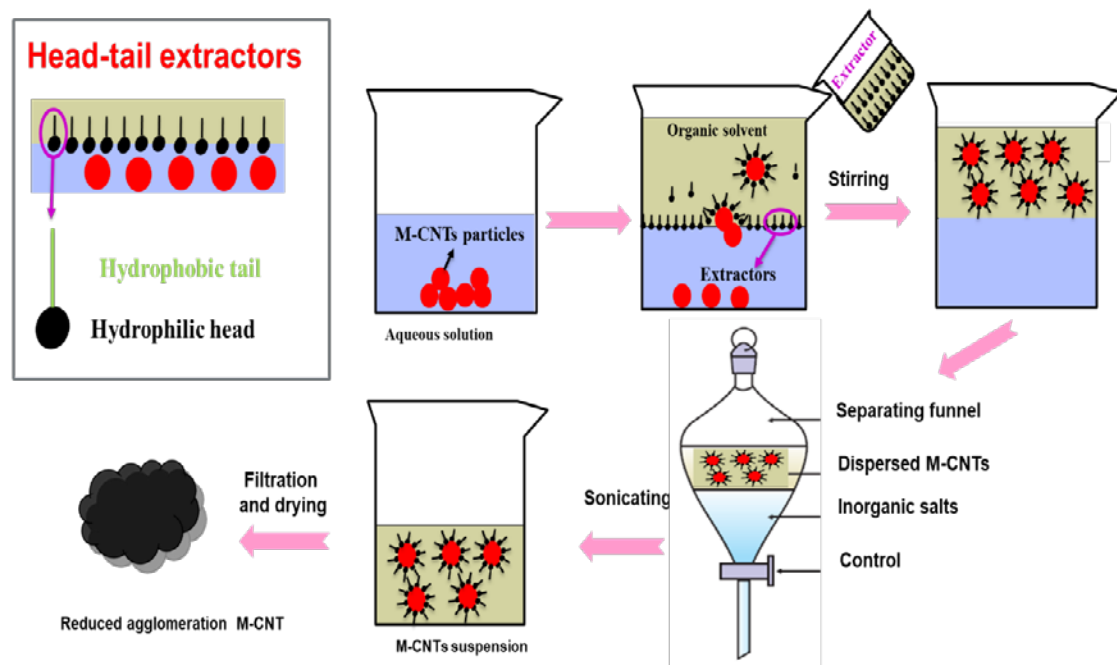


Figure 3.1 Schematic for the fabrication of M-CNTs composite by liquid-liquid extraction methods.

3.2 Synthesis of the MNPs coated MWCNTs using multifunctional dispersants

Figure 3.2 shows the procedures of Synthesis of MNPs coated MWCNTs by using the CCP method and multifunctional dispersants. In the given schematic, M-CNTs with CB dye were presented in which Fe^{2+} , Fe^{3+} salts, MWCNTs aqueous solutions, and ammonium hydroxide solutions have been used [37].

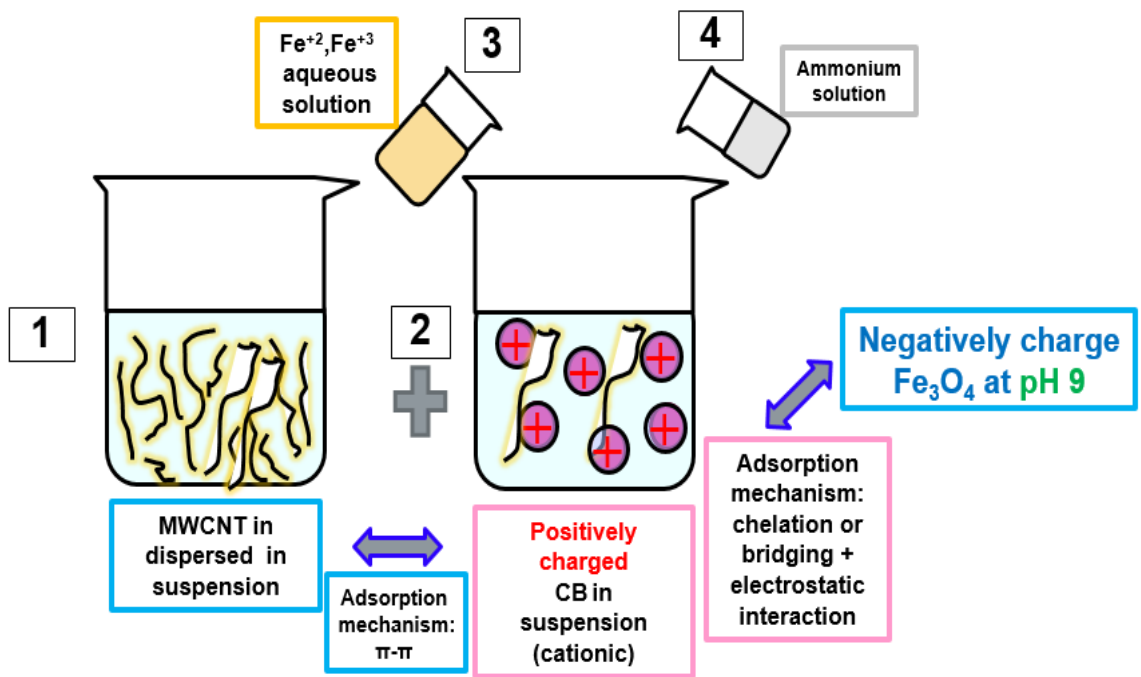


Figure 3.2 Schematic for the fabrication of M-CNTs composites by using multifunctional dispersant.

3.3 Material characterization

Several characterization techniques have been used to analyze the different parameters related to the materials synthesis and modifications processes as follow:

3.3.1 X-ray diffraction (XRD)

X-ray diffraction (XRD) analysis has been performed on the prepared sample, using the Bruker D8 DISCOVER instrument comprising DAVINCI diffractometer and Co-K α radiation. The raw data were collected over a 2θ value then processed and analyzed using GADDS and EVA software by Bruker to generate a data file with intensity and corresponding 2θ value.

3.3.2 Transmission electron microscope (TEM)

Transmission electron microscope and scanning transmission electron microscope (STEM) were performed using a JEOL 2010F to study the morphology of the samples in addition to the elemental analysis that was done using STEM/EDX line and map scan.

3.3.3 RAMAN spectroscopy

Raman spectroscopy analyses were carried out using a laser wavelength of 514 nm (Renishaw BZ02- Spectra-Physics Lasers, USA). It was done for all synthesized, as purchased, and composite samples.

3.3.4 FTIR spectroscopy

FTIR measurements were carried out on a Bruker Vertex 70 spectrometer in the wavenumber range of 400 - 2000 cm⁻¹.

3.4 Electrode fabrication by impregnation

The suspensions of active materials in ethanol solvent containing PVB were used for the impregnation of Ni foams.

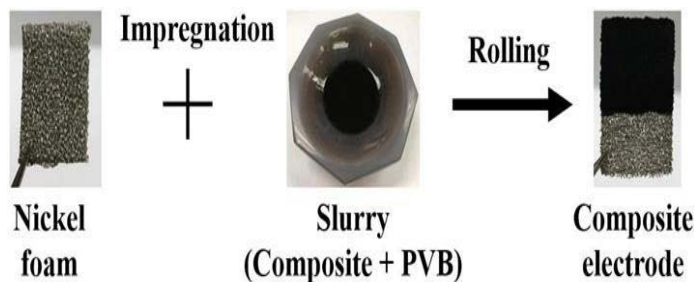


Figure 3.3 Schematic of composite electrode fabrication using slurry impregnation [34].

3.5 Electrochemical characterization

Three main techniques of electrochemical analyzing that have been done are cyclic voltammetry (CV), electrochemical impedance spectroscopy (EIS), and Galvanostatic charge-discharge as follows:

3.5.1 Cyclic voltammetry

Cyclic voltammetry (CV) of single electrodes and for the device have been performed in 0.5 M Na_2SO_4 aqueous electrolyte using a potentiostat (PARSTAT 2273, Princeton Applied Research) shown in Figure 3.4 (A). Single electrodes were tested using three electrodes setup, where standard calomel electrode (SCE) was used as the reference electrode and platinum gauze as the counter electrode as shown in Figure 3.4(B), and the setup for the device is shown in Figure 3.4(C). The integral capacitances $C_s = Q/\Delta V_s$ and $C_m = Q/\Delta V_m$ were calculated using half the integrated area of the CV curve to obtain the charge Q and subsequently dividing the charge Q by the width of the potential window ΔV and electrode area S .

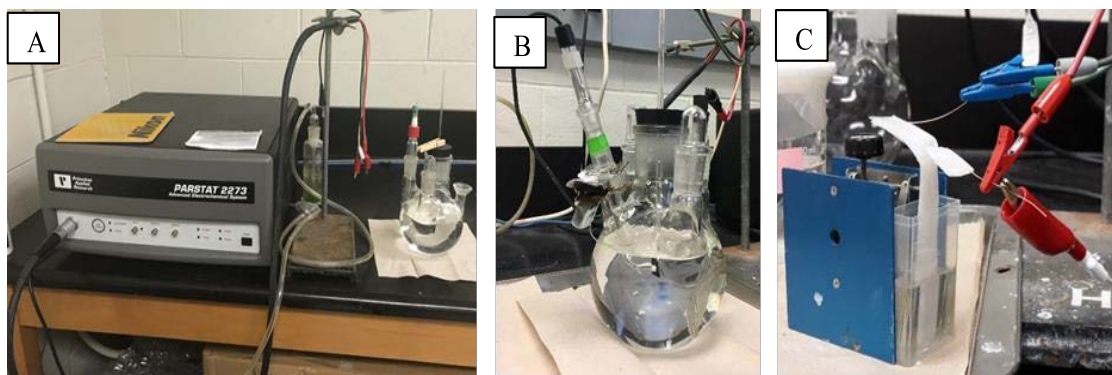


Figure 3.4 (A) Potentiostat (PARSTAT 2273, Princeton Applied Research), (B) The three electrodes cell setup, and (C) The supercapacitor device testing setup.

3.5.2 Electrochemical impedance spectroscopy

The electrochemical impedance spectroscopy (EIS) has been carried out using the PARSTAT 2273 potentiostat shown in Figure 3.4 (A). The alternating current measurements of complex impedance $Z^* = Z' - iZ''$ were performed in the frequency range of 10 mHz to 100 kHz at the amplitude of the signal of 5 mV. The complex differential capacitance $C_s^* = C_s' - iC_s''$ has been calculated from the impedance data as $C_s' = Z''/\omega|Z|2S$ and $C_s'' = Z'/\omega|Z|2S$, where $\omega = 2\pi f$ (f-frequency). The relaxation times $\tau = 1/\omega_m$ were calculated from the frequency to correspond to the maxima of C [7, 8].

3.5.3 Galvanostatic charge-discharge spectroscopy

Galvanostatic charge-discharge for single electrodes has been investigated in three-electrode cells by the analyzer (biologic VMP 300) shown in Figure 3.5 (A) using 0.5 M Na_2SO_4 aqueous electrolytes solutions. The counter electrode was a platinum gauze, and the reference electrode was a standard calomel electrode (SCE).

The charge-discharge behavior of the asymmetric device has been evaluated using the battery analyzers BST8-MA and BST8-3 (MTI Corporation, USA) shown in Figure 3.5 (B) at different current densities. Cyclic stability has been performed at a constant current density.

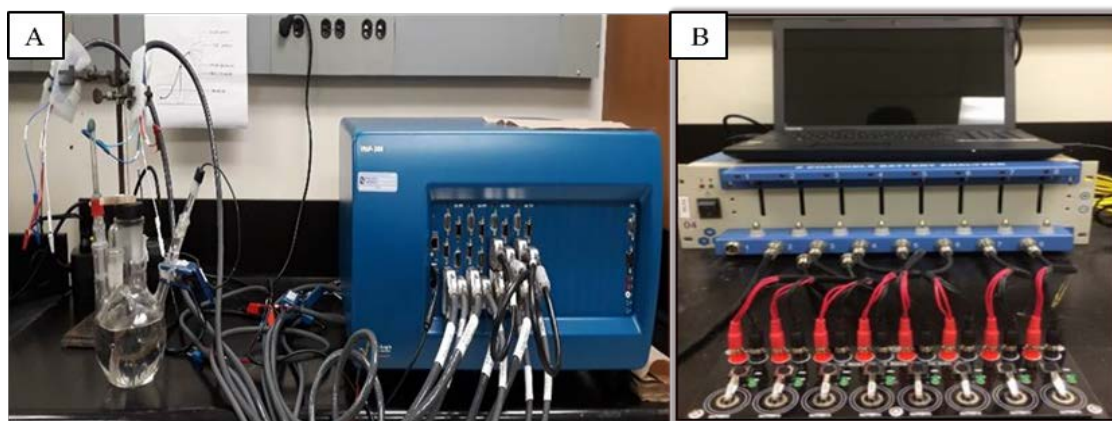


Figure 3.5 (A) Charge-discharge setup for single electrodes using analyzer (biologic VMB 300), (B) Battery analyzers (MTI Corporation, USA).

3.6 References

- [1] Mukrimin Sevket Guneya, Y.T., “Classification and assessment of energy storage systems”. *Renewable and Sustainable Energy Reviews* 75 1187–1197, 2017.
- [2] H. Ibrahima, A.I., J. Perron, “Energy storage systems characteristics and comparisons”. *Renewable and Sustainable Energy Reviews* 12 1221–1250, 2008.
- [3] [HTTPS://en.wikipedia.org/wiki/Supercapacitor](https://en.wikipedia.org/wiki/Supercapacitor).
- [4] Sinan N, U.E., “Fe₃O₄/carbon nanocomposite: investigation of capacitive & magnetic properties for supercapacitor applications”. *Materials Chemistry and Physics*. 183:571-579., 2016.
- [5] Li, X.a.B.W., “Supercapacitors based on nanostructured carbon”. *Nano Energy*, 2(2): p. 159-173, 2013.
- [6] W. D. Callister, M.S.a.E.A.I., 8th ed. John Wiley & Sons Inc.
- [7] B. E. Conway, V.B., and J. Wojtowicz, “The role and utilization of pseudocapacitance for energy storage by supercapacitors”. *Power Sources*, vol. 66, no. 1–2, pp. 1–14, 1997.
- [8] C. J. Wallar, “Colloidal fabrication of advanced oxide composite materials for supercapacitors”. Thesis, MSE , McMaster University, August 2017.
- [9] Gogotsi, Y.a.P.S., “True performance metrics in electrochemical energy storage”. *Science*, 334(6058): p. 917-918, 2011.
- [10] Augustyn, V., P. Simon, and B. Dunn, “Pseudocapacitive oxide materials for high-rate electrochemical energy storage”. *Energy & Environmental Science*, 7(5): p. 1597-1614, 2014.
- [11] K. Jost, G.D.a.Y.G., “A review on textile energy storage in perspective”. *The Royal Society of Chemistry*, 10.1039/c4ta00203b, 2014.

- [12] Xiong Z., H.Z., Chen Li, Kai Wang, Xianzhong S. and Yanwei Ma., “A review recent advances in porous graphene materials for supercapacitor applications”. The Royal Society of Chemistry, 45862 | RSC Adv., 2014.
- [13] Kötzt, R. and M. Carlen, “Principles and applications of electrochemical capacitors”. *Electrochimica Acta*, 45(15): p. 2483-2498, 2000.
- [14] Ri Chen, Miao Yu, Rakesh P Sahu, Ishwar K Puri, Igor Zhitomirsky, “The development of pseudocapacitor electrodes and devices with high active mass loading”. *Advanced Energy Materials*, vol. 10, issue 20 pp. 1903848, 2020.
- [15] Kokkinidis, G., “Underpotential deposition and electrocatalysis”. Elsevier, 1986.
- [16] Green, C.L. and A. Kucernak, “Determination of the platinum and ruthenium surface areas in platinum– ruthenium alloy electrocatalysts by underpotential deposition of copper. I. Unsupported catalysts”. *The Journal of Physical Chemistry B*, 106(5): p. 1036-1047, 2002.
- [17] Lorenz, W., et al., “The formation of monolayer metal films on electrodes”. *Journal of The Electrochemical Society*, 121(9): p. 1167-1177. 1974.
- [18] Liu, Y., “Fabrication of composite electrodes and supercapacitor devices”. Thesis, McMaster University, 2016.
- [19] Shi, K., “Advanced materials for energy storage in supercapacitors and capacitive water purification”. Thesis, McMaster University, 2016.
- [20] Ma, S., et al., “A novel concept of hybrid capacitor based on manganese oxide materials”. *Electrochemistry Communications*, 9(12): p. 2807-2811. 2007.
- [21] Sergej R., a.E.H., Seda G.,a,b Mike C.,a Nora K., “Synergetic effects of Fe³⁺ doped spinel Li₄Ti₅O₁₂ nanoparticles on reduced graphene oxide for high surface electrode hybrid supercapacitors”. *The Royal Society of Chemistry* 45862 | RSC Adv.10.1039/, 2018.

- [22] Paula N. , M.A., Rebeca M., Jesús P. , “ Insights into the energy storage mechanism of hybrid supercapacitors with redox electrolytes by electrochemical impedance spectroscopy”. *Electrochimica Acta* 263, 2018.
- [23] A. G. Pandolfo and A. F. Hollenkamp, J., “Carbon properties and their role in supercapacitors”. *Power Sources*, vol. 157, no. 1, pp. 11–27, , 2006.
- [24] Xu, B., et al., “Activated carbon fiber cloths as electrodes for high performance electric double layer capacitors”. *Electrochimica Acta*. 52(13): p. 4595-4598, 2007.
- [25] Kim, S.U. and K.H. Lee, “Carbon nanofiber composites for the electrodes of electrochemical capacitors". *Chemical Physics Letters*, 400(1): p. 253-257, 2004..
- [26] Sivakkumar, S., et al., "Performance evaluation of CNT/polypyrrole/MnO₂ composite electrodes for electrochemical capacitors". *Electrochimica Acta*, 52(25): p. 7377-7385, 2007.
- [27] L. Borchardt, M.O., and S. Kaskel, “Tailoring porosity in carbon materials for supercapacitor applications”. *Mater Horiz*, vol. 1, no. 2, pp. 157–168, 2014.
- [28] Endo, M., et al., “Capacitance and pore size distribution in aqueous and nonaqueous electrolytes using various activated carbon electrodes”. *Journal of the Electro chemical society*, 148 (8): p. A910 A914, 2001.
- [29] Zhi, M., et al., “ Nanostructured carbon metal oxide composite electrodes for supercapacitors”. A review, *Nanoscale*, 5 (1): p. 72 88., 2013.
- [30] Arul, V.D.N.a.N.S., “ Progress and development of Fe₃O₄ electrodes for supercapacitors”. *Mater. Chem. A*, 4, 10767, 2016,.
- [31] Chi-yuen H. , Chi-wai K. , Chee-leung M. , and Kam-hong C., “ An introductory review of textile-based flexible supercapacitors”, *Processes* 7, 922; Doi:10.3390/pr7120922, 2019.

- [32] Yinxiang Zeng, M.Y., Yue M., Pingping F., Xihong Lu, and Yexiang T., “ Iron-based supercapacitor electrodes: advances and challenges ”. *Adv. Energy Mater.* 6, 1601053, 2016.
- [33] Y. He, W. Chen, X. Li, Z. Zhang, J. Fu, C. Zhao and E. Xie, “ Freestanding three-dimensional graphene/MnO₂ composite networks as ultralight and flexible supercapacitor electrodes ”. *ACS Nano*, vol. 7, no. 1, pp. 174-182, 2013.
- [34] Ryan Poon, “ Fabrication of advanced electrode materials for electrochemical supercapacitor applications ”. PhD Thesis , MSE, McMaster University, December 2019.
- [35] Y. Liu and I. Zhitomirsky, “Aqueous electrostatic dispersion and heterocoagulation of multiwalled carbon nanotubes and manganese dioxide for the fabrication of supercapacitor electrodes and devices” . *RSC Adv*, vol. 4, no. 85, pp. 45481–45489, 2014.
- [36] L. Hamming, X.F., P. Messersmith, and L. Brinson, “Mimicking mussel adhesion to improve interfacial properties in composites”. *Compos. Sci. Technol.*, vol. 68, no. 9, pp. 2042–2048, 2008.
- [37] M. S. Ata, Y.L.a.I.Z., “A review of new methods of surface chemical modification, dispersion and electrophoretic deposition of metal oxide particles ”. *The Royal Society of Chemistry*: 10.1039, 2014.
- [38] G. Cao and Y. Wang, “ Nanostructures and nanomaterials: synthesis, properties, and applications ”. Ed. Hackensack, NJ: World Scientific, 2011.
- [39] F. Avilés, J.V.C.-R., L. Moo-Tah, A. May-Pat, and R. Vargas- Coronado, “Evaluation of mild acid oxidation treatments for MWCNT functionalization”. *Carbon*, vol. 47, no. 13, pp. 2970–2975, 2009.
- [40] B. Vigolo, “ Macroscopic fibers and ribbons of oriented carbon nanotubes ”. *Science*, vol. 290, no. 5495, pp. 1331–1334, 2000.
- [41] Gamby, J., et al. “ Studies and characterisations of various activated carbons used for carbon/carbon supercapacitors. *Journal of power sources* ”. 101 (1): p. 109 116., 2001.

- [42] Mustafa S. Ata, R.P., Aseeb M. Syed, Jordan Milne, Igor Zhitomirsky, “New developments in non-covalent surface modification, dispersion and electrophoretic deposition of carbon nanotubes”. *Carbon* 130, 2018.
- [43] C. Zhong, Y. D. Deng, W. B. Hu, J. L. Qiao, L. Zhang, and J. J. Zhang, “A review of electrolyte materials and compositions for electrochemical supercapacitors”. *Chemical Society Reviews*, vol. 44, pp. 7484-7539, 2015.
- [44] F. Beguin, V. Presser, A. Balducci, and E. Frackowiak, “ Carbons and electrolytes for advanced supercapacitors”. *Advanced Materials*, vol. 26, pp. 2219-2251, Apr 2014.
- [45] X. L. Wang, A. B. Yuan, and Y. Q. Wang, “ Supercapacitive behaviors and their temperature dependence of sol-gel synthesized nanostructured manganese dioxide in lithium hydroxide electrolyte”. *Journal of Power Sources*, vol. 172, pp. 1007-1011, Oct 25 2007.
- [46] M. Galinski, A. Lewandowski, and I. Stepniak, “ Ionic liquids as electrolytes”. *Electrochimica Acta*, vol. 51, pp. 5567-5580, Aug 15 2006.
- [47] L. H. Su, L. Y. Gong, H. T. Lu, and Q. Xu, “ Enhanced low-temperature capacitance of MnO₂ nanorods in a redox-active electrolyte”. *Journal of Power Sources*, vol. 248, pp. 212-217, Feb 15 2014.
- [48] Yan, J., Wang, Q., Wei, T., and Fan, Z., 2014, “ Recent advances in design and fabrication of electrochemical supercapacitors with high energy densities”. *Adv. Energy Mater.*, 4(4). 4, 1300816A 2014,
- [49] Pandey, G. P., Kumar, Y., and Hashmi, S. A., 2010, “ Ionic liquid incorporated polymer electrolytes for supercapacitor application”. *Indian Journal of Chemistry*, Vol. 49A, p. 743-751, Jun 2010.
- [50] Bashir, S., et al., “ Synthesis of α and β FeOOH iron oxide nanoparticles in non ionic surfactant medium”. *Journal of Nanoparticle Research*, 11 (3): p. 701 706., 2009.

- [51] Sahoo, N.G., et al., “ Polypyrrole coated carbon nanotubes: synthesis, characterization, and enhanced electrical properties”. *Synthetic Metals*, . 157 (8): p. 374 379., 2007.
- [52] Xiangcun Li, Le Zhang, Gaohong He., “ Fe₃O₄ doped double-shelled hollow carbon spheres with hierarchical”. *Carbon* vol. 99, 0008-6223 , 2016.
- [53] S.M. Alshehri, J. Ahmed, A.N. Alhabarah, T. Ahamad, T. Ahmad, “ Nitrogen-doped cobalt ferrite/carbon nanocomposites for supercapacitor applications”. *ElectroChem*, 4(11) 2952-8., 2017.
- [54] He, M.a.T.M.S., “ Covalent functionalization of carbon nanomaterials with Iodonium salts”. *Chemistry of Materials*,. 28 (23): p. 8542 8549., 2016.
- [55] Esumi, K., et al., “ Chemical treatment of carbon nanotubes ”. *Carbon*, . 34 (2): 279 281., 1996.
- [56] Y. Zhu, K.S., and I. Zhitomirsky, *J. Mater.*, “Anionic dopant–dispersants for synthesis of polypyrrole coated carbon nanotubes and fabrication of supercapacitor electrodes with high active mass loading ”. *Chem. A*, vol. 2, no. 35, p. 14666, 2014.
- [57] M. M. Ramli, W.Z., S. R. P. Silva, and S. J. Henley, , “Dye-assisted dispersion of single-walled carbon nanotubes for solution fabrication of NO₂ sensors”. *AIP Adv.*, vol. 2, no. 3, p. 032165, 2012.
- [58] Chen, R., et al., “ MnO₂-carbon nanotube electrodes for supercapacitors with high active mass loadings ”. *Journal of The Electrochemical Society*, 164(7): p. A1673-A1678, 2017.
- [59] Gund, G.S., et al. , “ Low cost flexible supercapacitors with high energy density based on nanostructured MnO₂ and Fe₂O₃ thin films directly fabricated onto stainless steel”. *Scientific reports*, 2015.
- [60] Lei, Y., et al., “ MnO₂ coated Ni nanorods Enhanced high rate behavior in pseudo capacitive supercapacitor.e supercapacitor ”. *Electrochimica Acta*, . 5555(25): p. 7454(25): , 2010.

- [61] P. Yu, Z. W. Chen, R. Maric, L. Zhang, J. J. Zhang, and J. Y. Yan, “ Electrochemical supercapacitors for energy storage and delivery: Advanced materials, technologies and applications”. *Applied Energy*, vol. 153: pp. 1-2, Sep 1 2015.
- [62] H Xiangcun Li, Le Zhang, Gaohong He., “ Fe_3O_4 doped double-shelled hollow carbon spheres with hierarchical”. *Carbon* vol. 99: 0008-6223 , 2016.
- [63] Brousse, T. and D. Bélanger, “A hybrid Fe_3O_4 - MnO_2 capacitor in mild aqueous electrolyte”. *Electrochemical and Solid-state letters*, vol. 6 (11): p. A244-A248.,2003.
- [64] V.D. Nithya, N.S. Arul, “Review on $\text{-Fe}_2\text{O}_3$ based negative electrode for high performance supercapacitors, *Journal of Power Sources*, vol. 327: p. 297-318.,2016.
- [65] C.D. Lokhande, D.P. Dubal, O.S. Joo, “ Metal oxide thin film based supercapacitors”. *Current Applied Physics* vol.11(3): p. 255-270., 2011.
- [66] Silva, R.M.E., et al., “ New developments in liquid-liquid extraction, surface modification and agglomerate-free processing of inorganic particles”. *Advances in Colloid and Interface Science*, vol. 261: p. 15-27, 2018.

Chapter 4

High areal capacitance of Fe₃O₄-decorated carbon nanotubes for supercapacitor electrodes

Mohamed Nawwar^a, Ryan Poon^a, Ri Chen^b, Rakesh P. Sahu^b, Ishwar K. Puri^{a,b} and Igor

Zhitomirsky^{a*}

^aDepartment of Materials Science and Engineering

^bDepartment of Mechanical Engineering

McMaster University, Hamilton, ON, Canada, L8S 4L7

E-mail: zhitom@mcmaster.ca , Tel. 1-905-525-9140

Submitted on 26 July 2019. Published on 30 September 2019

Reprinted with Permission from Carbon Energy Journal ,Published by John Wiley &

Sons Australia, Ltd on Behalf of Wenzhou University

Copyright 2019, Reproduced with Permission from Carbon Energy Journal

4.1 Abstract

A conceptually new approach has been developed for the fabrication of magnetite (Fe_3O_4)-decorated carbon nanotubes (M-CNTs) for negative electrodes of electrochemical supercapacitors. M-CNTs were prepared by an ultrasonic-assisted chemical synthesis method, which involved dispersion of functionalized CNTs in water, Fe_3O_4 formation on the CNTs surface, and particle extraction through liquid-liquid interface (PELLI). Palmitic acid was found to be an efficient new extractor for PELLI. The slurries produced after drying and re-dispersing M-CNTs and slurries obtained using PELLI were used for electrode fabrication. The electrodes prepared using PELLI showed superior performance due to reduced particle agglomeration. Testing results provided an insight into the influence of $\text{Fe}_3\text{O}_4/\text{CNTs}$ mass ratio on the capacitance and capacitance retention at high charge-discharge rates. A capacitance of 5.82 F cm^{-2} (145.4 F g^{-1}) was achieved in Na_2SO_4 electrolyte using electrodes with high active mass of 40 mg cm^{-2} and ratio of active mass to current collector mass of 0.6. Good electrochemical performance was achieved at low impedance. The capacitance of the negative M-CNTs electrodes was comparable with capacitance of advanced positive $\text{MnO}_2\text{-CNTs}$ electrodes, which was beneficial for the fabrication of asymmetric devices. The asymmetric device has been fabricated, which showed promising performance in a voltage window of 1.6 V.

Keywords: asymmetric device, capacitance, carbon nanotube, composite, magnetite, supercapacitor

4.2 Introduction

The surface modification of carbon nanotubes (CNTs) has received significant attention ¹, ² due to many novel applications of CNTs that are decorated with various functional materials. The attractive properties of functionally decorated CNTs combine the high electrical and thermal conductivity of CNTs and their mechanical and optical properties with the functional properties of other materials. Various techniques have been developed to fabricate decorated CNTs, such as magnetron sputtering³, electrodeposition ⁴, chemical precipitation⁵, atomic layer deposition⁶, pulsed laser ablation⁷, and chemical polymerization⁸.

Functionally decorated CNTs have integrated properties of CNTs and energy storage materials for battery applications and allowed for significant improvement in the capacity ^{3,5}, cyclic stability ⁴, and conductivity of batteries⁹. Multifunctional separators for batteries have been developed using CNTs decorated with TiO₂ quantum dots ⁶. It was found that CNTs, decorated with metals¹⁰, quantum dots¹¹, and other photovoltaic materials¹² enhanced the efficiency of solar cells. Of particular interest are applications of decorated CNTs as advanced catalysts for fuel cells¹³. In the field of supercapacitor devices for energy storage, investigations have been focused on the use of polypyrrole ¹⁴, ¹⁵, activated carbon¹⁶, and oxide materials^{17,18} for the decoration of CNTs. These studies have generated interest in the decorating CNTs with Fe₃O₄ for use as electrodes of supercapacitors.

Fe_3O_4 is a promising pseudocapacitive material for negative electrodes of supercapacitors. The redox-active properties of Fe_3O_4 are related to Fe^{2+} and Fe^{3+} oxidation states. However, due to the low electronic conductivity of Fe_3O_4 and poor electrolyte access to the material surface, the specific capacitance decreases significantly with increasing active mass loading. Therefore, Fe_3O_4 is combined with conductive carbon additives to increase the overall electronic conductivity.

Fe_3O_4 electrodes containing different carbon materials, such as activated carbon^{19, 20} acetylene black²¹ graphene^{22, 23} graphite²⁴, and CNTs^{25, 26} have been developed and tested in different electrolytes, such as KOH, H_2SO_4 , Na_2SO_3 , and Na_2SO_4 . Electrodes have been used with low active mass loadings in the 1 to 9 mg cm^{-2} range^{20-22, 24, 27-31}.

Fe_3O_4 -decorated CNTs and Fe_3O_4 -CNTs composite electrodes have shown promising capacitive properties^{26, 30-33}. The enhanced performance of Fe_3O_4 -based composite electrodes has been achieved in 1M H_2SO_4 ²², 1M Na_2SO_3 ³², and 6M KOH^{27, 33} electrolytes. However, the use of Na_2SO_4 electrolyte offers benefits for fabricating asymmetric devices with a large voltage window and enhanced energy storage properties.

It has been found³⁴ that Fe_3O_4 -based negative electrodes, containing graphite and acetylene black, can complement a MnO_2 -based positive electrode in a mild Na_2SO_4 electrolyte. The complementary potential windows of the individual electrodes allows for the formation of an aqueous device^{34, 35}, operating in a voltage window of 1.8 V. A specific capacitance of 50 F g^{-1} at a mass loading of 8.8 mg cm^{-2} was determined for Fe_3O_4 negative electrode. The capacitance of the negative Fe_3O_4 electrode was significantly lower than that of positive MnO_2 electrode at the same electrode mass. In this case, larger mass of the

negative electrode was required to match total capacitance of the positive electrode. Therefore, further improvements in the technology of Fe_3O_4 electrodes are necessary to match the specific capacitance of MnO_2 electrodes and reduce the total mass of the device. Of particular importance is the development of advanced electrodes that have enhanced performance at mass loadings of about 10 to 20 mg cm^{-2} , which is required for practical applications.

The goal of this investigation was the fabrication of advanced Fe_3O_4 -decorated CNTs for application in negative electrodes with high active mass loadings and high capacitance. A conceptually new approach has been developed for the magnetite-decorated carbon nanotubes (M-CNTs) fabrication. M-CNTs were prepared by an ultrasonic-assisted chemical synthesis method, which involved dispersion of functionalized CNTs in water, Fe_3O_4 formation on the CNTs surface, and application of particle extraction through liquid-liquid interface (PELLI) for the fabrication of well-dispersed particles. Palmitic acid (PA) was found to be an efficient new extractor for PELLI. The approach developed in this investigation allowed the fabrication of electrodes with an active mass of 40 mg cm^{-2} , which demonstrated a capacitance of 5.82 F cm^{-2} (145.4 F g^{-1}). The areal capacitance obtained is significantly higher than the literature data for Fe_3O_4 -based electrodes. Moreover, high capacitance was achieved at low impedance.

Analysis of experimental data provided insight into the influence of PELLI and mass ratio $\gamma = \text{Fe}_3\text{O}_4/\text{CNTs}$ on capacitance and rate performance. The experimental results presented below indicate that the high capacitance of the Fe_3O_4 -decorated CNTs negative electrodes practically matches the capacitance of MnO_2 -CNTs positive electrodes in the Na_2SO_4

electrolyte at comparable active mass. The asymmetric capacitors, containing Fe₃O₄-decorated CNTs negative electrodes and MnO₂-CNTs positive electrodes showed promising performance.

4.3 Experimental procedures

Carbon nanotubes (CNT, Multiwalled, diameter 20-30 nm, length 1–2 μm, US Nanomaterial Inc, USA), FeCl₃.6H₂O, FeCl₂.4H₂O, NH₄OH, Palmitic acid (PA), polyvinyl butyral (PVB), Na₂SO₄, n-butanol (Sigma- Aldrich) and Ni foams (95 % porosity, Vale) were used. CNT were functionalized by treatment in concentrated nitric acid at 60 C° in ultrasonic bath for 4 hours. After washing, the acid treated CNT were dried in oven at 60 C° for 12 hours.

An ultrasonic-assisted chemical precipitation method has been used for the decoration of the activated CNTs with Fe₃O₄. In this method, acid-treated CNTs were dispersed in an aqueous solution of FeCl₂ and FeCl₃ ($\text{Fe}^{2+}:\text{Fe}^{3+} = 1:2$) under ultrasonication and pH of the solution was adjusted to 9 using NH₄OH. The concentration of the iron salts was varied to obtain mass ratio $\gamma = \text{Fe}_3\text{O}_4:\text{CNTs}$ in the range of 0.25 to 1.0. The obtained M-CNTs were used for the fabrication of electrodes.

The M-CNTs formed in an aqueous phase were filtrated. Obtained powders were washed, dried, and re-dispersed in ethanol. In another approach, M-CNTs were directly extracted to n-butanol by the PELLI method ³⁶ using PA as an extractor. The M-CNTs suspensions prepared by drying and re-dispersion or by PELLI method were used for impregnation of Ni foams. The PVB binder was added to the suspensions. The mass ratio PVB: M-CNTs was 0.03. The mass loading of 40 mg cm⁻² included the mass of M-CNTs

and PVB binder. The obtained electrodes were used as anodes for asymmetric supercapacitor cells. The procedure for the fabrication of MnO₂-CNTs cathodes was described in a previous investigation³⁷.

Electron microscopy investigations were performed using Titan 80-300 LB transmission electron microscope (TEM). X-ray diffraction (XRD) studies were performed using a Bruker D8 diffractometer and Co K α radiation. The electrochemical equipment for cyclic voltammetry, chronopotentiometry, and impedance spectroscopy testing of electrodes and devices were described in previous investigations^{38,39}. All the electrochemical testing experiments were performed using 0.5M Na₂SO₄ electrolyte.

4.4 Results and discussion

The formation of M-CNTs was confirmed by XRD, TEM and energy-dispersive X-ray spectroscopy (EDX) data. The comparison of the X-ray diffraction patterns (Figure 4.1) of Fe₃O₄ prepared without CNTs, M-CNTs and CNTs showed that M-CNTs contained peaks of both: Fe₃O₄ and CNTs.

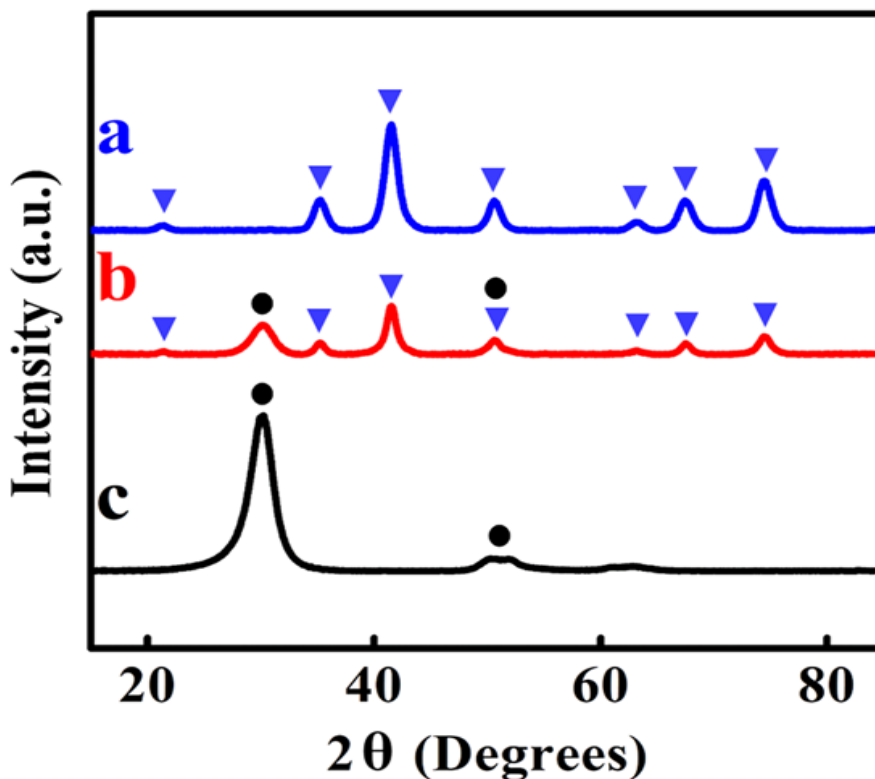


Figure 4.1 X-ray diffraction patterns of (a) Fe₃O₄ powder, (b) M-CNTs, and (c) acid - treated CNTs. ▼, JCPDS file 19 - 0629; ●, JCPDS No. 41 - 1487; M-CNTs, magnetite - decorated carbon nanotube.

Figure 4.2 (A) shows scanning transmission electron microscope of M-CNTs. The image indicates that CNTs were decorated with nanoparticles. The typical size of the nanoparticles was below 25 nm. The EDX scan Figure 4.2 (B) confirmed that the particles contained Fe. It is known that ⁴⁰ nitric acid treated CNTs contain carboxylic groups, which facilitate CNTs dispersion. We suggested that such carboxylic groups promoted Fe₃O₄ nanoparticle synthesis on the CNTs surface. The M-CNTs were used for the fabrication of negative electrodes of supercapacitors.

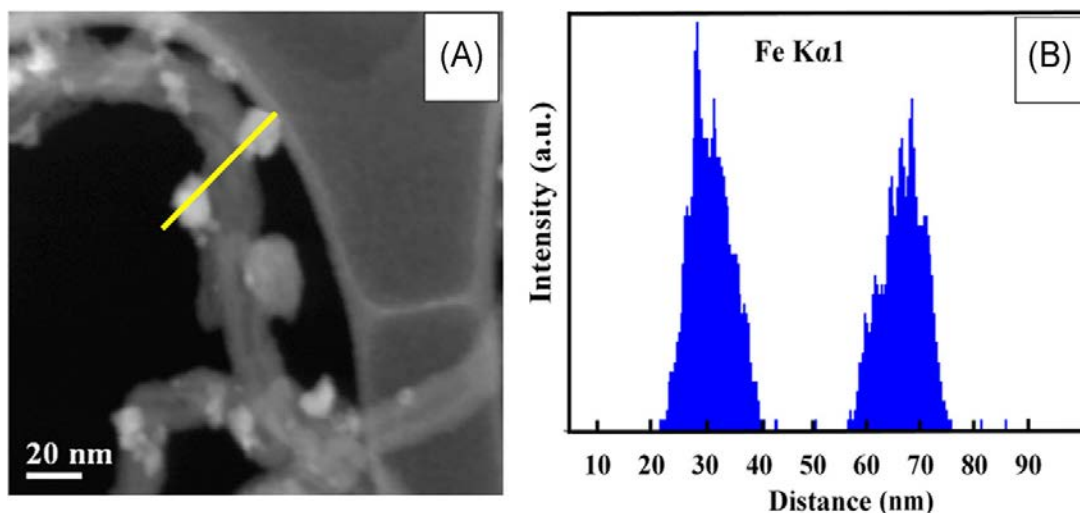


Figure 4.2 A, STEM image; B, EDX line scan for Fe (the line is shown in (A)). EDX, energy - dispersive X - ray spectroscopy; STEM, scanning transmission electron microscope.

The use of commercial Ni foam current collectors was critical for the fabrication of electrodes with high active mass loading. However, the formation of suspensions for the impregnation of Ni foam current collectors presented difficulties due to M-CNTs agglomeration that resulted from the Van der Waals and magnetic attraction forces. The high aspect ratio of M-CNTs is another factor promoting agglomeration and sedimentation. Therefore, PELLI method has been developed to reduce M-CNTs agglomeration. This method requires careful selection of an extractor, which must be soluble in an organic solvent and adsorbed on particles at the liquid-liquid interface.

The extraction efficiency was close to 100%. Figure 4.3 (A) shows a chemical structure of PA that was used as an extractor for PELLI. PA is a typical head-tail surfactant, containing a hydrophobic hydrocarbon group, which facilitated PA dissolution in n-butanol. The carboxylic group of PA allowed for PA adsorption on Fe_3O_4 by chelating or bridging bonding Figure 4.3 (B). Similar to other surfactants, PA accumulated at the liquid-liquid interface with the hydrophilic carboxylic groups exposed to the aqueous phase. The extraction mechanism involved PA adsorption on the particles at the liquid-liquid interface and particles transfer to the n-butanol phase.

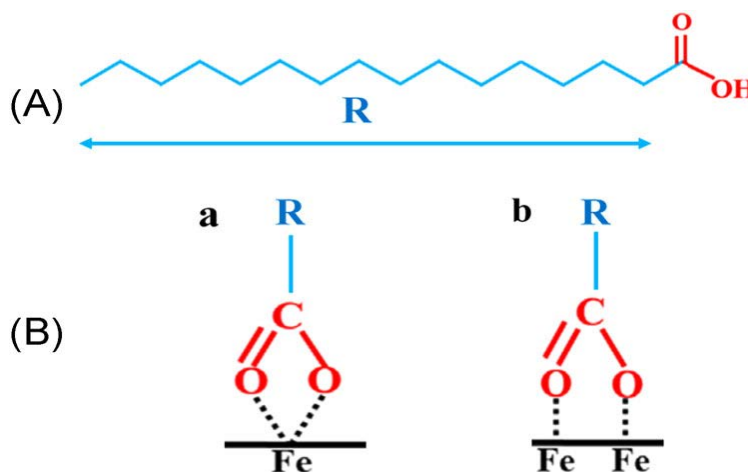


Figure 4.3 A, Chemical structure of PA; B, adsorption mechanisms, involving Fe atoms on the particle surface and carboxylic acid group of PA: (a) chelation, (b) bridging. PA, Palmitic acid.

Testing of the electrodes revealed benefits of extracted M-CNTs, as compared to dried and re-dispersed M-CNTs. Figure 4.4 compares cyclic voltammetry dependences (CVs) for electrodes with $\gamma = 0.40$ and $\gamma = 1.00$. The M-CNTs electrodes prepared using PELLI showed significantly larger CVs areas, compared with M-CNTs formed by a traditional drying and re-dispersion method at the same scan rates.

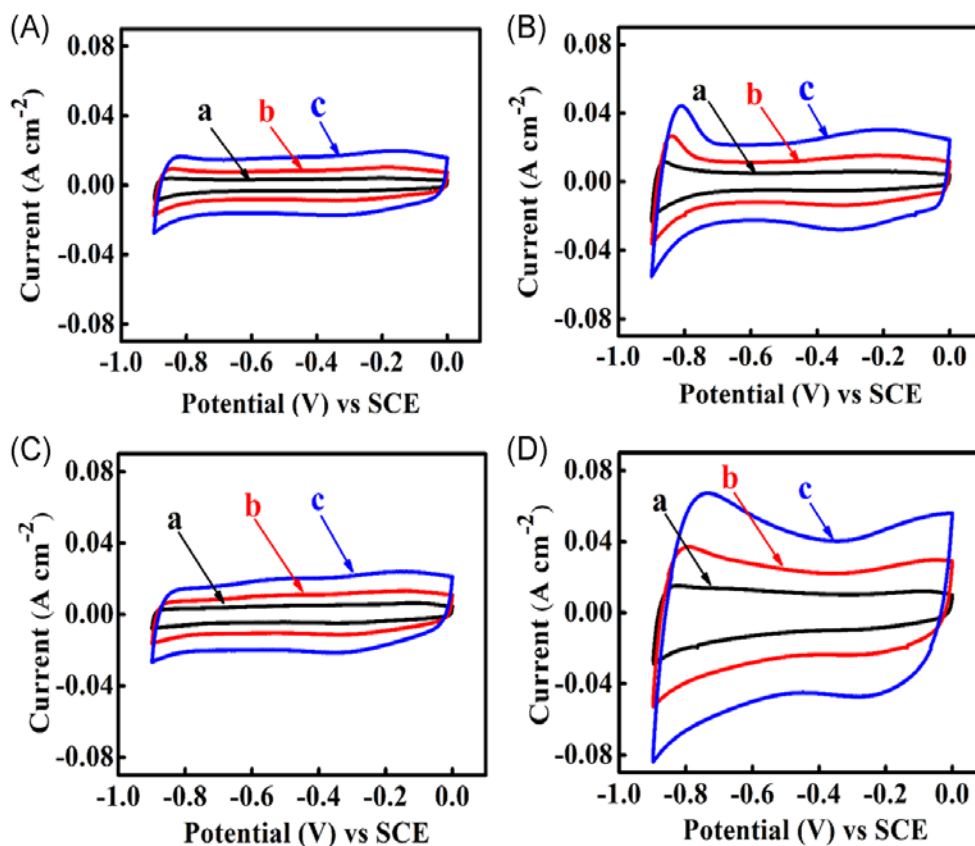


Figure 4.4 CVs at scan rates of (a) 2, (b) 5, and (c) 10 mV s^{-1} for M - CNTs electrodes, prepared (A, B) without PELLi and (C, D) using PELLi for (A, C) $\gamma = 0.40$ and (B, D) $\gamma = 1.0$. M-CNTs, magnetite - decorated carbon nanotube; PELLi, particle extraction through liquid - liquid interface.

The capacitances of the electrodes with different γ were calculated from CV data at different scan rates and presented in (Figure 4.5). The M-CNTs electrodes prepared using PELLi showed higher capacitances. The benefits of PELLi are especially evident for $\gamma = 0.7$ and $\gamma = 1$. The highest capacitance of 5.82 F cm^{-2} (145.4 F g^{-1}) was obtained at a scan rate of 2 mV s^{-1} for M-CNTs electrodes with $\gamma = 1.00$. Such electrodes showed a capacitance retention of 37% at a scan rate of 100 mV s^{-1} . The capacitance of the M-CNTs electrodes

prepared using PELLI for $\gamma = 1.00$ was significantly higher, compared with literature data for the capacitance of other Fe_3O_4 -based electrodes, which were described in Section 1.

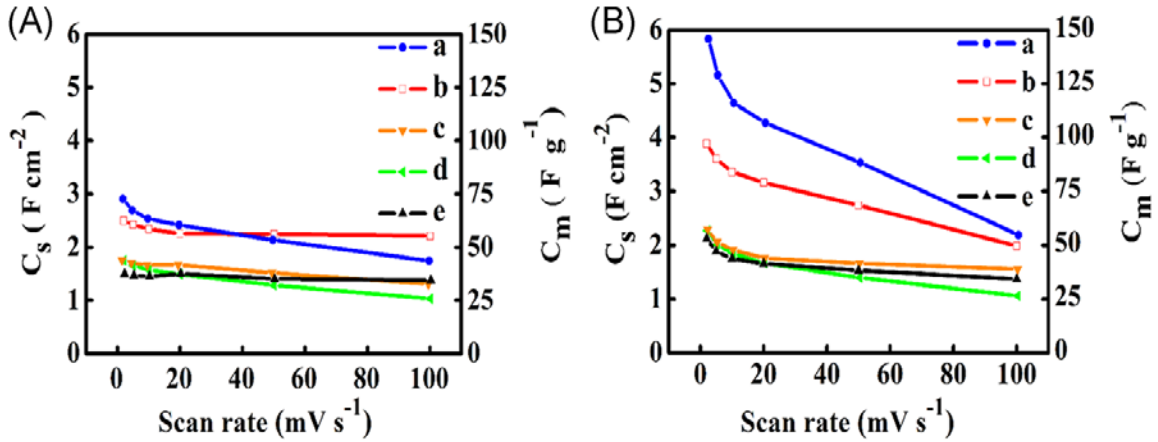


Figure 4.5 C_s and C_m vs scan rate for M-CNTs: A, prepared without PELLI and B, using PELLI for (a) $\gamma = 1.0$, (b) $\gamma = 0.70$, (c) $\gamma = 0.55$, (d) $\gamma = 0.40$, and (e) $\gamma = 0.25$. M-CNTs, magnetite-decorated carbon nanotube; PELLI, particle extraction through liquid-liquid interface.

The M-CNTs electrodes with $\gamma = 0.55$ and $\gamma = 0.7$ prepared using PELLI showed capacitances of 3.88 F cm^{-2} (97.1 F g^{-1}) and 2.12 F cm^{-2} (53.1 F g^{-1}) at 2 mV s^{-1} , and capacitance retentions of 51% and 65%, respectively. The increase in capacitance with increasing γ resulted from the higher capacitance of Fe_3O_4 , as compared with that of CNTs. However, better capacitance retention was obtained at lower γ values. The capacitance of electrodes usually decreases with increasing scan rate, especially for high active mass. Such decrease is related to diffusion limitations of electrolyte in pores of electrode material. The impregnation of electrodes without PELLI presented difficulties. In this case, the material was accumulated close to the current collector surface and blocked electrolyte access. As a result, the capacitance was low, but it was less influenced by the scan rate.

Using PELLI we enhanced capacitance significantly, especially for low scan rates and $\gamma = 1$. However, the diffusion limitations resulted in capacitance reduction with increasing scan rate and lower rate performance.

The analysis of the impedance data provides additional evidence of the beneficial effect of the decorated CNTs and the PELLI method. The M-CNTs electrodes exhibited a relatively low real part of the impedance due to good contact of Fe_3O_4 and CNTs in the decorated CNTs (Figure 4.6). The electrodes prepared using PELLI showed a lower real part of the impedance, as compared with the electrodes, prepared without PELLI. The differential capacitances C_s' , calculated from the impedance data at different frequencies were higher for the electrodes prepared using PELLI. The analysis of differential capacitances at different frequencies revealed relaxation type dispersions (Figure 4.6). The use of PELLI resulted in lower charge transfer resistance due to better impregnation of the current collectors with active material. Moreover, the electrodes prepared using PELLI showed slight increase in the relaxation frequency, as compared with the electrodes, prepared without PELLI.

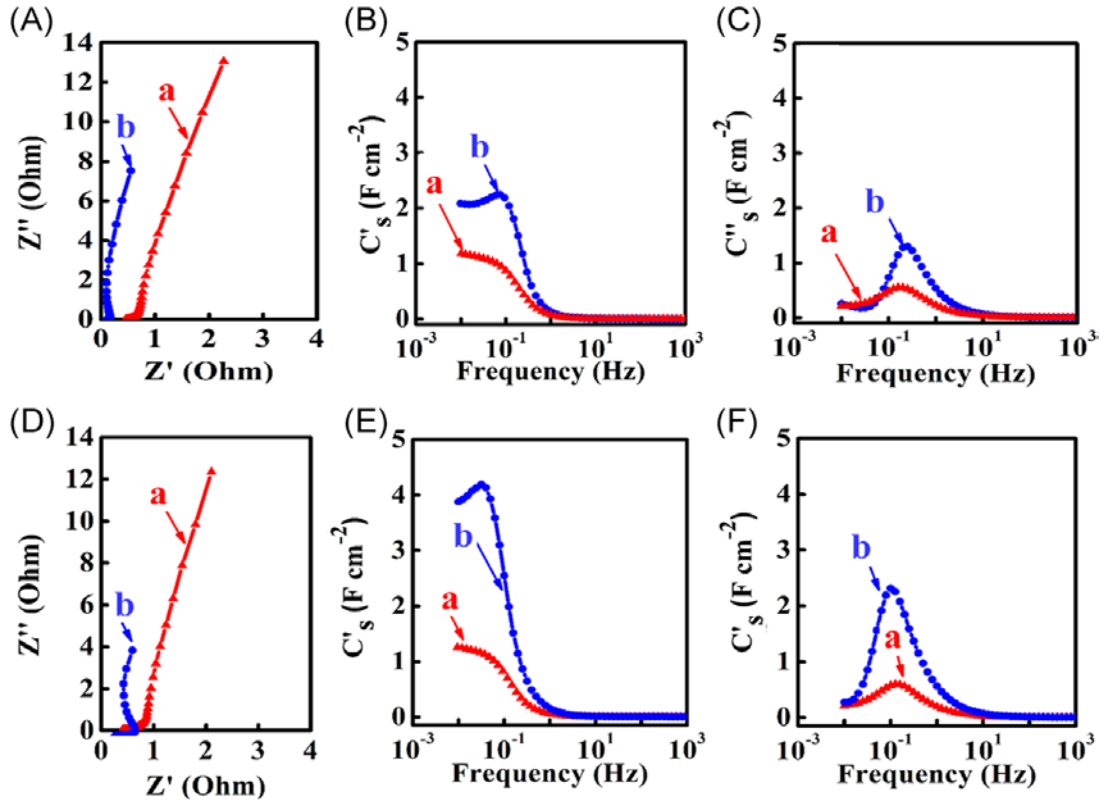


Figure 4.6 EIS data for M-CNTs electrodes, prepared (A, B, C) without PELLI and (D, E, F) using PELLI: (A, D) Nyquist plot of complex impedance and frequency dependences of (B, E) C'_s and (C, F) C''_s for (a) $\gamma = 0.40$, and (b) $\gamma = 1.00$. EIS, electrochemical impedance spectroscopy; M-CNTs, magnetite-decorated carbon nanotube; PELLI, particle extraction through liquid-liquid interface.

The chronopotentiometry data showed nearly ideal symmetrical triangular shapes of the charge-discharge curves at different current densities Figure 4.7 (A). The capacitances of the electrodes were also calculated from the constant current discharge data and presented in Figure 4.7 (B). The capacitance of 5.2 F cm^{-2} was obtained at a discharge current of 3 mA cm^{-2} for electrode, prepared using PELLI. The capacitance decreased with increasing current density to the level of 4.2 F cm^{-2} at 20 mA cm^{-2} . The electrode, prepared without PELLI showed significantly lower capacitance Figure 4.7 (B).

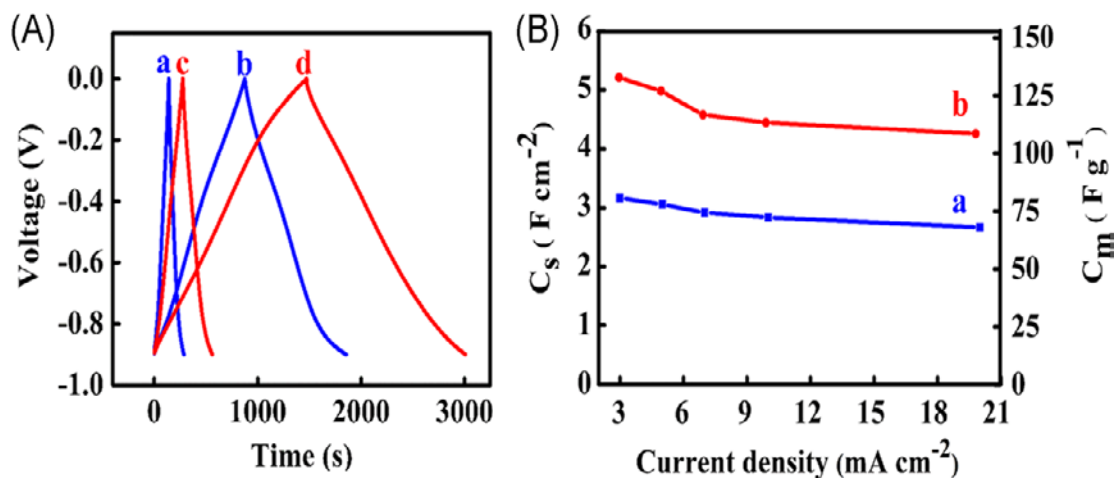


Figure 4.7 A, Charge - discharge curves for M-CNTs electrodes ($\gamma = 1.0$) prepared (a, b) without PELLI and (c, d) using PELLI at current densities of (a, c) 20 and (b, d) 3 mA cm⁻²; B, C_s and C_m vs. scan rate for M-CNTs electrodes ($\gamma = 1.0$) prepared (a) without PELLI and (b) using PELLI. M-CNTs, magnetite - decorated carbon nanotube; PELLI, particle extraction through liquid - liquid interface.

Testing results indicated that the capacitance of the electrodes depended on different parameters, such as scan rate, current density, alternating current (AC) frequency, and voltage. The comparison of the data at similar charge-discharge time revealed lower AC differential capacitance, compared with the integral capacitances, derived from the CV and chronopotentiometry data. The difference can be attributed to reduced electrolyte access to the active material at low AC voltage.

The relatively high capacitance of the electrodes prepared using PELLI is promising for the fabrication of asymmetric devices with enlarged voltage window in Na₂SO₄ electrolyte. The use of Na₂SO₄ electrolyte offers advantages, compared with Na₂SO₃.

It is known ⁴¹ that advanced materials for positive electrodes, such as MnO₂, exhibit excellent capacitive performance in Na₂SO₄. Moreover, asymmetric capacitor cells with

enlarged voltage window can be fabricated using this electrolyte. Turning again to the literature data [34] on the fabrication of $\text{Fe}_3\text{O}_4/\text{MnO}_2$ asymmetric devices, it is seen that the active mass ratio of $\text{MnO}_2/\text{Fe}_3\text{O}_4$ (R) was $R = 0.33$. The larger mass of Fe_3O_4 electrode³⁴ was necessary to match the capacitance of the positive electrode. The approach developed in our investigation allowed for significantly higher specific capacitance (145.4 F g^{-1}) of the M-CNTs electrodes, as compared with the specific capacitance of Fe_3O_4 composites (50 F g^{-1}), reported in the literature³⁴. The higher capacitance was achieved at significantly higher active mass. The high areal capacitance of 5.82 F cm^{-2} obtained at 2 mV s^{-1} for negative M-CNTs electrodes ($\gamma=1$) at active mass of 40 mg cm^{-2} was close to the capacitance of 5.81 F cm^{-2} at 2 mV s^{-1} for MnO_2 -CNTs electrode achieved³⁷ at an active mass of 35 mg cm^{-2} . Therefore, good capacitance matching can be achieved at 2 mV s^{-1} for mass ratio of negative/positive electrodes $R = 0.88$. However, MnO_2 -CNTs electrodes showed³⁷ better capacitance retention at scan rates in the range of 2 to 20 mV s^{-1} . Therefore, the mass of the negative electrode was increased to match the capacitance of the positive electrode at a scan rate of 20 mV s^{-1} . The desired ratio of $R = 0.7$ was obtained using $10 \times 10 \text{ mm}$ positive electrodes and $11 \times 11 \text{ mm}$ negative electrodes. The obtained asymmetric device showed good capacitive behavior in a voltage window of 1.6 V, as indicated by nearly box shape CVs Figure 4.8 (A).

The average electrode area was used for the calculation of areal capacitance for the device at different scan rates Figure 4.8 (B). The areal capacitance of 2.3 F cm^{-2} was obtained at a scan rate of 2 mV s^{-1} . EIS data showed that real part of the impedance increased, compared with that for the individual components Figure 4.8 (C).

The total electrode resistance included the resistance of the individual electrodes and electrolyte in pores of a separator membrane. The relaxation frequency of the device shifted to lower frequencies, as compared with the relaxation frequencies of the individual electrodes Figure 4.8 (D, E).

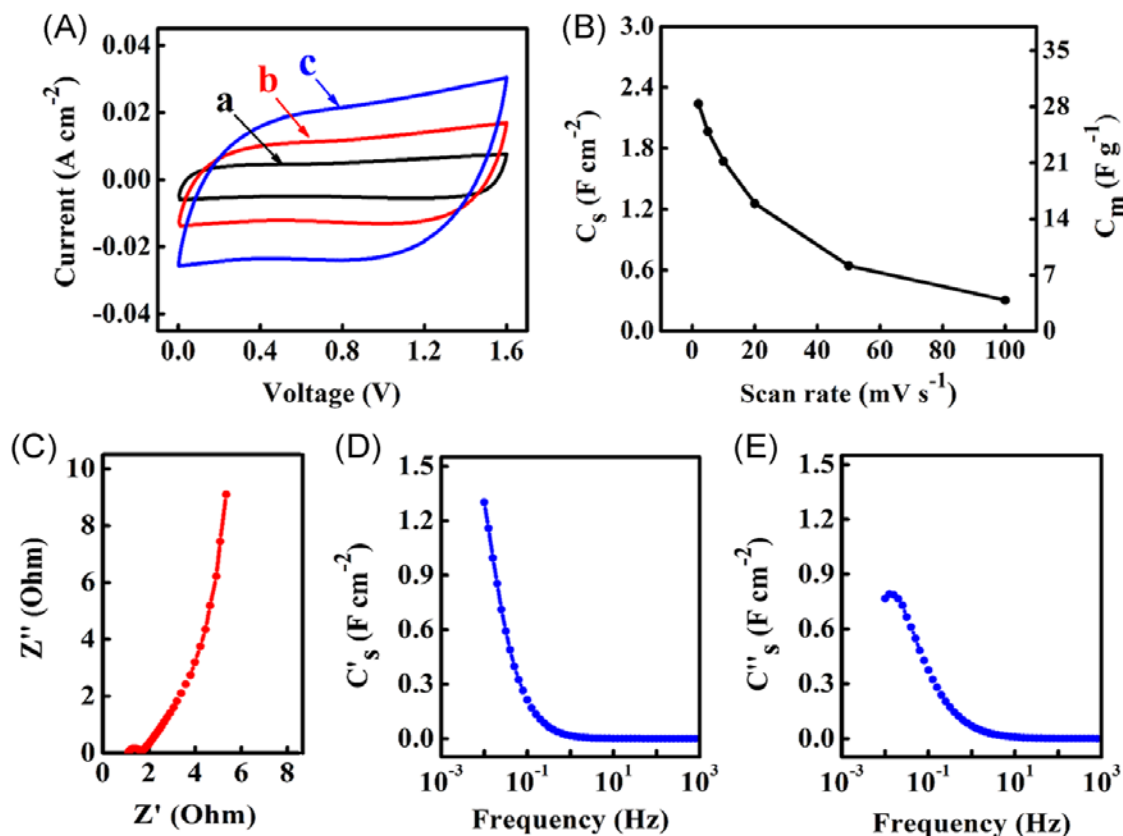


Figure 4.8 A, CVs at scan rates of (a) 2, (b) 5, and (c) 10 mV s⁻¹; B, C_s and C_m vs scan rate; C, Nyquist plot of complex impedance and frequency dependences of D, C_s' and E C_s'' for an asymmetric supercapacitor cell, containing MnO₂-CNTs as a positive electrode and M-CNTs ($\gamma = 1.0$). Prepared using PELLI as a negative electrode. M-CNTs, magnetite-decorated carbon nanotube; PELLI, particle extraction through liquid-liquid interface.

The chronopotentiometry studies showed symmetrical triangular charge-discharge curves at various current densities Figure 4.9 (A). A capacitance of 2.7 F cm^{-2} was obtained at a discharge current density of 3 mA cm^{-2} . The capacitance decreased with increasing current density Figure 4.9 (B), the capacitance retention at 50 mA cm^{-2} was 75%. The chronopotentiometry data was used to calculate the power density and energy density at different current densities.

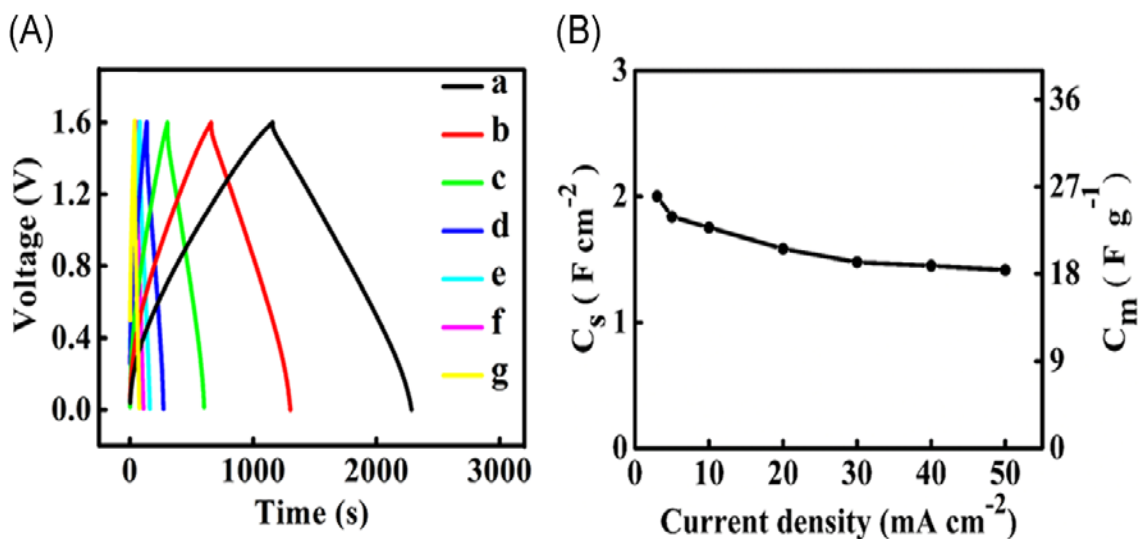


Figure 4.9 A, Charge-discharge curves at current densities of (a) 3, (b) 5, (c) 10, (d) 20, (e) 30, (f) 40, and (g) 50 mA cm^{-2} ; B, C_s and C_m vs. current density for an asymmetric supercapacitor cell, containing MnO_2 -CNTs as a positive electrode and M-CNTs ($\gamma=1.0$) prepared using PELLI as a negative electrode. M-CNTs, magnetite-decorated carbon nanotube; PELLI, particle extraction through liquid-liquid interface.

The data are presented in a Ragone plot (Figure 4.10 (A)), which indicate that relatively high power-energy characteristics were obtained for the asymmetric device with high active mass. High power energy characteristics have also been reported in other investigations⁴²⁻⁴⁴. It is important to note that specific capacitance, power density, and energy density

decrease significantly with increasing active mass. Therefore, good electrochemical performance at high active mass, achieved in our investigation, is promising for practical applications. Of particular importance is that in this investigation a high capacitance was achieved at low impedance. Another important factor is mass ratio of active mass to current collector mass (δ_M). In our investigation good electrochemical performance of M-CNTs electrodes was achieved at a relatively high $\delta_M = 0.6$. The device showed a capacitance retention of 87% after 3000 cycles and Coulombic efficiency of 100% Figure 4.10 (B).

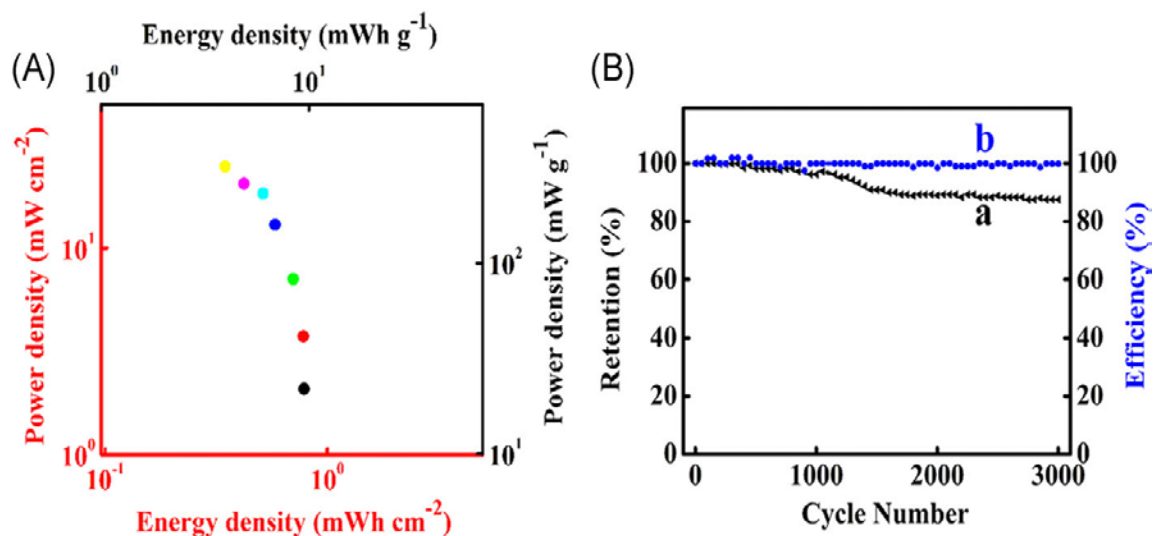


Figure 4.10 A, Ragone plot for an asymmetric supercapacitor cell, containing MnO₂-CNTs as a positive electrode and M-CNTs ($\gamma = 1.0$) prepared using PELLI as a negative electrode; B, (a) capacitance retention and (b) Coulombic efficiency vs cycle number. M-CNTs, magnetite-decorated carbon nanotube; PELLI, particle extraction through liquid-liquid interface.

4.5 Conclusions

Fe₃O₄-decorated CNTs were prepared by an ultra-sonic assisted chemical synthesis method, which involved the dispersion of functionalized CNTs in water and Fe₃O₄ nanoparticle formation on the CNTs surface. The use of PA as an extractor for PELLI facilitated the transfer of M-CNTs from an aqueous synthesis medium to an organic medium for electrode fabrication. PELLI allowed for reduced M-CNTs agglomeration and improved impregnation of Ni foam current collectors. The M-CNTs electrodes, prepared using PELLI, showed higher capacitance and lower resistance, as compared with M-CNTs electrodes prepared without PELLI. Good electrochemical performance was achieved at a high active mass loading of 40 mg cm⁻².

The highest capacitance of 5.82 F cm⁻² (145.4 F g⁻¹) was achieved for $\gamma=1$ at 2mV s⁻¹, however the electrodes with lower γ showed better capacitance retention at high scan rates. Enhanced electrochemical performance of M-CNTs electrodes was achieved at a low impedance and relatively high $\delta M = 0.6$. The capacitance of the negative M-CNTs electrodes prepared using PELLI was comparable with capacitance of advanced positive MnO₂-CNTs electrodes, which was beneficial for the fabrication of asymmetric devices. The asymmetric device has been fabricated, which showed promising performance in a voltage window of 1.6 V.

4.6 Acknowledgement

The authors gratefully acknowledge the Natural Sciences and Engineering Research Council of Canada for the financial support.

4.7 References

- [1] Pang X, Imin P, Zhitomirsky I, Adronov A. Amperometric Detection of Glucose Using a Conjugated Polyelectrolyte Complex with Single-Walled Carbon Nanotubes. *Macromolecules*. 2010;43(24):10376-10381.
- [2] Pan Y, Hu W, Liu D, Liu Y, Liu C. Carbon nanotubes decorated with nickel phosphide nanoparticles as efficient nanohybrid electrocatalysts for the hydrogen evolution reaction. *Journal of Materials Chemistry A*. 2015;3(24):13087-13094.
- [3] Guan C, Liu J, Wang Y, et al. Iron Oxide-Decorated Carbon for Supercapacitor Anodes with Ultrahigh Energy Density and Outstanding Cycling Stability. *ACS Nano*. 2015;9(5):5198-5207.
- [4] Hao M, Tang M, Wang W, Tian M, Zhang L, Lu Y. Silver-nanoparticle-decorated multiwalled carbon nanotubes prepared by poly (dopamine) functionalization and ultraviolet irradiation. *Composites Part B: Engineering*. 2016;95:395-403.
- [5] Wei W, Ruiz I, Ahmed K, et al. Silicon Decorated Cone Shaped Carbon Nanotube Clusters for Lithium Ion Battery Anodes. *Small*. 2014;10(16):3389-3396.
- [6] Chitturi VR, Ara M, Fawaz W, Ng KYS, Arava LMR. Enhanced Lithium–Oxygen Battery Performances with Pt Subnanocluster Decorated N-Doped Single-Walled Carbon Nanotube Cathodes. *ACS Catalysis*. 2016;6(10):7088-7097.
- [7] Hong HP, Kim MS, Lee YH, Yu JS, Lee CJ, Min NK. Spray deposition of LiMn_2O_4 nanoparticle-decorated multiwalled carbon nanotube films as cathode material for lithium-ion batteries. *Thin Solid Films*. 2013;547:68-71.
- [8] Ding H, Zhang Q, Liu Z, et al. TiO_2 quantum dots decorated multi-walled carbon nanotubes as the multifunctional separator for highly stable lithium sulfur batteries. *Electrochimica Acta*. 2018;284:314-320.

- [9] Imbrogno A, Pandiyan R, Barberio M, Macario A, Bonanno A, El khakani MA. Pulsed-laser-ablation based nanodecoration of multi-wall-carbon nanotubes by Co-Ni nanoparticles for dye-sensitized solar cell counter electrode applications. *Materials For Renewable and Sustainable Energy*. 2017;6(2):11 (10 pp.).
- [10] Zhu Y, Shi K, Zhitomirsky I. Polypyrrole coated carbon nanotubes for supercapacitor devices with enhanced electrochemical performance. *Journal of Power Sources*. 2014;268:233-239.
- [11] Wang T, Kaempgen M, Nopphawan P, Wee G, Mhaisalkar S, Srinivasan M. Silver nanoparticle-decorated carbon nanotubes as bifunctional gas-diffusion electrodes for zinc-air batteries. *Journal of Power Sources*. 2010;195(13):4350-4355.
- [12] Mathew A, Rao GM, Munichandraiah N. Dye sensitized solar cell based on platinum decorated multiwall carbon nanotubes as catalytic layer on the counter electrode. *Materials Research Bulletin*. 2011;46(11):2045-2049.
- [13] Kaniyoor A, Ramaprabhu S. Gold Nanoparticle Decorated Multi-Walled Carbon Nanotubes as Counter Electrode for Dye Sensitized Solar Cells. *Journal of Nanoscience and Nanotechnology*. 2012;12(11):8323-8329.
- [14] Ting N, Jingying Y, Yurong J, et al. Enhancement of the power conversion efficiency of polymer solar cells by functionalized single-walled carbon nanotubes decorated with CdSe/ZnS core-shell colloidal quantum dots. *Journal of Materials Science*. 2014;49(6):2571-2577.
- [15] Tai S-Y, Lu M-N, Ho H-P, Xiao Y, Lin J-Y. Investigation of carbon nanotubes decorated with cobalt sulfides of different phases as nanocomposite catalysts in dye-sensitized solar cells. *Electrochimica Acta*. 2014;143:216-221.
- [16] Sonkar PK, Prakash K, Yadav M, et al. Co(II)-porphyrin-decorated carbon nanotubes as catalysts for oxygen reduction reactions: an approach for fuel cell improvement. *Journal of Materials Chemistry A*. 2017;5(13):6263-6276.

- [17] Zhenhai W, Suqin C, Shun M, et al. TiO₂ nanoparticles-decorated carbon nanotubes for significantly improved bioelectricity generation in microbial fuel cells. *Journal of Power Sources*. 2013;234:100-106.
- [18] Su Y, Zhitomirsky I. Asymmetric electrochemical supercapacitor, based on polypyrrole coated carbon nanotube electrodes. *Applied Energy*. 2015;153:48-55.
- [19] Shi K, Zhitomirsky I. Fabrication of Polypyrrole-Coated Carbon Nanotubes Using Oxidant–Surfactant Nanocrystals for Supercapacitor Electrodes with High Mass Loading and Enhanced Performance. *ACS Applied Materials & Interfaces*. 2013;5(24):13161-13170.
- [20] Shi K, Ren M, Zhitomirsky I. Activated Carbon-Coated Carbon Nanotubes for Energy Storage in Supercapacitors and Capacitive Water Purification. *ACS Sustainable Chemistry & Engineering*. 2014;2(5):1289-1298.
- [21] Ojha M, Le Houx J, Mukkabl R, Kramer D, Andrew Wills RG, Deepa M. Lithium titanate/pyrenecarboxylic acid decorated carbon nanotubes hybrid - Alginate gel supercapacitor. *Electrochimica Acta*. 2019;309:253-263.
- [22] Shancheng Y, Haitao W, Peng Q, Yong Z, Zhongdang X. RuO₂/carbon nanotubes composites synthesized by microwave-assisted method for electrochemical supercapacitor. *Synthetic Metals*. 2009;159(1-2):158-161.
- [23] Du X, Wang C, Chen M, Jiao Y, Wang J. Electrochemical performances of nanoparticle Fe₃O₄/activated carbon supercapacitor using KOH electrolyte solution. *The Journal of Physical Chemistry C*. 2009;113(6):2643-2646.
- [24] Sinan N, Unur E. Fe₃O₄/carbon nanocomposite: Investigation of capacitive & magnetic properties for supercapacitor applications. *Materials Chemistry and Physics*. 2016;183:571-579.
- [25] Zeng Y, Yu M, Meng Y, Fang P, Lu X, Tong Y. Ironon magnetic properties for supercapacitor applications. *dAdvanced Energy Materials*. 2016;6(24):1601053.

- [26] Mishra AK, Ramaprabhu S. Functionalized Graphene-Based Nanocomposites for Supercapacitor Application. *The Journal of Physical Chemistry C*. 2011;115(29):14006-14013.
- [27] Sheng S, Liu W, Zhu K, et al. Fe₃O₄ nanospheres in situ decorated graphene as high-performance anode for asymmetric supercapacitor with impressive energy density. *Journal of colloid and interface science*. 2019;536:235-244.
- [28] Sayahi H, Mohsenzadeh F, Darabi HR, Aghapoor K. Facile and economical fabrication of magnetite/graphite nanocomposites for supercapacitor electrodes with significantly extended potential window. *Journal of Alloys and Compounds*. 2019;778:633-642.
- [29] Mishra AK, Ramaprabhu S. Magnetite decorated multiwalled carbon nanotube based supercapacitor for arsenic removal and desalination of seawater. *Journal of Physical Chemistry C*. 2010;114(6):2583-2590.
- [30] Wang Q, Jiao L, Du H, Wang Y, Yuan H. Fe₃O₄ nanoparticles grown on graphene as advanced electrode materials for supercapacitors. *Journal of Power Sources*. 2014;245:101-106.
- [31] Qi T, Jiang J, Chen H, Wan H, Miao L, Zhang L. Synergistic effect of Fe₃O₄/reduced graphene oxide nanocomposites for supercapacitors with good cycling life. *Electrochimica Acta*. 2013;114:674-680.
- [32] Ghasemi S, Ahmadi F. Effect of surfactant on the electrochemical performance of graphene/iron oxide electrode for supercapacitor. *Journal of Power Sources*. 2015;289:129-137.
- [33] Shi X, Zhang S, Chen X, Tang T, Mijowska E. Effect of iron oxide impregnated in hollow carbon sphere as symmetric supercapacitors. *Journal of Alloys and Compounds*. 2017;726:466-473.

- [34] Kumar A, Sarkar D, Mukherjee S, Patil S, Sarma D, Shukla A. Realizing an Asymmetric Supercapacitor Employing Carbon Nanotubes Anchored to Mn_3O_4 Cathode and Fe_3O_4 Anode. *ACS applied materials & interfaces*. 2018;10(49):42484-42493.
- [35] Nithya V, Arul NS. Progress and development of Fe_3O_4 electrodes for supercapacitors. *Journal of Materials Chemistry A*. 2016;4(28):10767-10778.
- [36] Kim Y-H, Park S-J. Roles of nanosized Fe_3O_4 on supercapacitive properties of carbon nanotubes. *Current Applied Physics*. 2011;11(3):462-466.
- [37] Guan D, Gao Z, Yang W, et al. Hydrothermal synthesis of carbon nanotube/cubic Fe_3O_4 nanocomposite for enhanced performance supercapacitor electrode material. *Materials Science and Engineering: B*. 2013;178(10):736-743.
- [38] Brousse T, Bélanger D. A Hybrid Fe_3O_4 - MnO_2 Capacitor in Mild Aqueous Electrolyte. *Electrochemical and solid-state letters*. 2003;6(11):A244-A248.
- [39] Cottineau T, Toupin M, Delahaye T, Brousse T, Bélanger D. Nanostructured transition metal oxides for aqueous hybrid electrochemical supercapacitors. *Applied Physics A*. 2006;82(4):599-606.
- [40] Silva RME, Poon R, Milne J, Syed A, Zhitomirsky I. New developments in liquid-liquid extraction, surface modification and agglomerate-free processing of inorganic particles. *Advances in Colloid and Interface Science*. 2018;261:15-27.
- [41] Chen R, Poon R, Sahu RP, Puri IK, Zhitomirsky I. MnO_2 -carbon nanotube electrodes for supercapacitors with high active mass loadings. *Journal of The Electrochemical Society*. 2017;164(7):A1673-A1678.
- [42] Su Y, Zhitomirsky I. Hybrid MnO_2 /carbon nanotube-VN/carbon nanotube supercapacitors. *Journal of Power Sources*. 2014;267:235-242.
- [43] Shi C, Zhitomirsky I. Electrodeposition and Capacitive Behavior of Films for Electrodes of Electrochemical Supercapacitors. *Nanoscale Research Letters*. 2010;5(3):518.

[44] Worsley KA, Kalinina I, Bekyarova E, Haddon RC. Functionalization and Dissolution of Nitric Acid Treated Single-Walled Carbon Nanotubes. *Journal of the American Chemical Society*. 2009;131(50):18153-18158.

4.8 Supporting informations

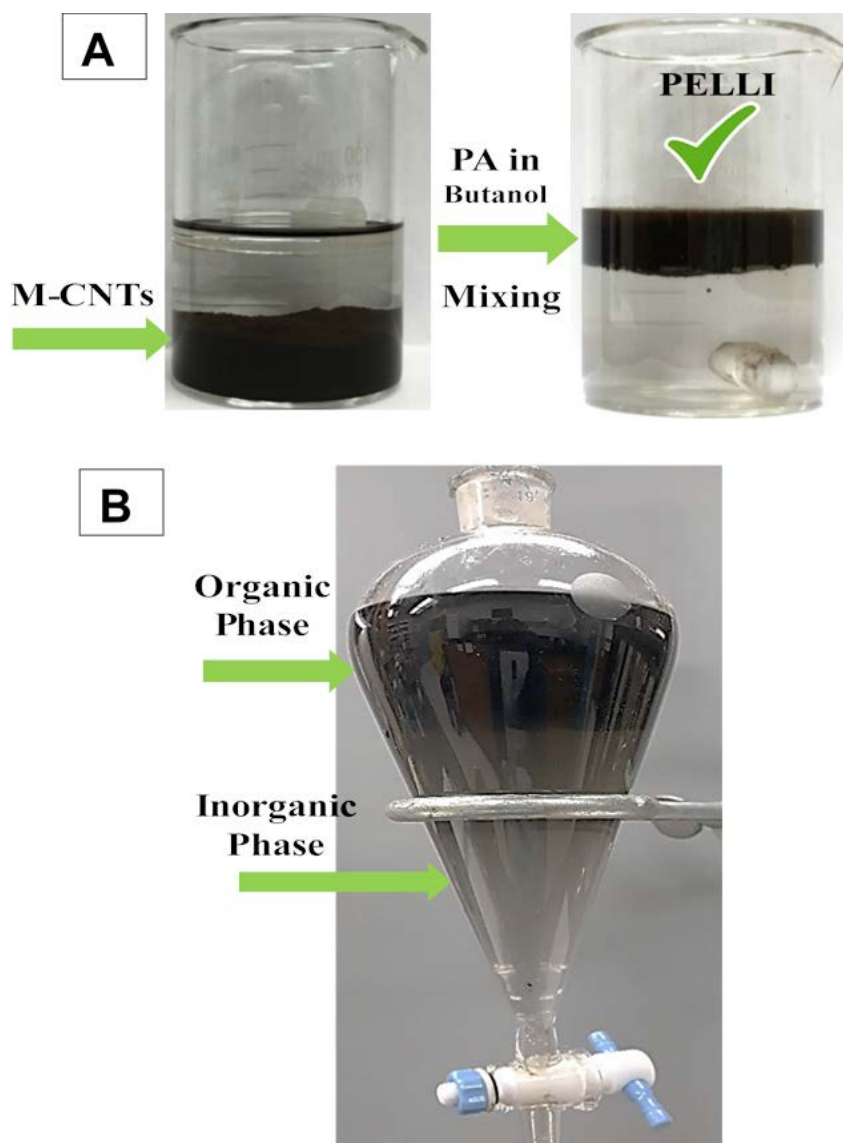


Figure 4.11 (A) PELL I for M-CNTs by PA (B) Separation of the inorganic phase with the impurities and sideproducts.

Chapter 5

Fe₃O₄ spinel-Mn₃O₄ spinel supercapacitor prepared using Celestine blue as a dispersant, capping agent and charge transfer mediator

Mohamed Nawwar^a, Ryan Poon^a, Rakesh P. Sahu^b, Ishwar K. Puri^{a,b} and Igor Zhitomirsky^{a,*},

^a Department of Materials Science and Engineering,

^b Department of Mechanical Engineering

McMaster University, Hamilton, Ontario, Canada L8S 4L7

* Corresponding Author: zhitom@mcmaster.ca.in. Tel.: +1 905 525-9140 ext. 23914

Submitted on 22 November 2019. Published on 22 April 2020.

Reprinted with Permission from Ceramic international Journal 0272-8842/ 2020

Copyright (2020), Reproduced with Permission from Ceramic international Journal

5.1 Abstract

An asymmetric spinel-spinel supercapacitor is fabricated with negative and positive electrodes consisting of Fe_3O_4 and Mn_3O_4 nanoparticles, respectively, where carbon nanotubes (CNT) serve as conductive additives. High performance of the individual electrodes and devices is achieved at a high active mass (AM) loading of 40 mg cm^{-2} for the individual electrodes. A conceptually new strategy is based on the use of multifunctional Celestine blue (CB) dye, which is strongly adsorbed on the spinel phases and CNT, facilitates dispersion, acts as a capping agent and allows for the fabrication of spinel decorated CNT. Moreover, it is discovered that CB is an efficient charge transfer mediator, which allows for significant improvement of capacitive behavior. The use of CB as a charge transfer mediator allows for good utilization of capacitive properties of spinels at high AM. Mechanisms of spinel-CB-CNT interactions and charge transfer mediation are discussed. The capacitive properties are analyzed by cyclic voltammetry, chronopotentiometry and impedance spectroscopy for the electrodes with different spinel/CNT mass ratios. The areal capacitances of 6.17 and 5.15 F cm^{-2} are obtained for Fe_3O_4 and Mn_3O_4 based electrodes, respectively in $0.5 \text{ M Na}_2\text{SO}_4$ electrolyte. The high capacitances are achieved with low electrode resistance. The electrodes are used for the fabrication of an asymmetric device which shows a capacitance of 2.41 F cm^{-2} in a voltage window of 1.6 V .

Key words: spinel, iron oxide, manganese oxide, carbon nanotube, supercapacitor, charge transfer, dispersant, composite

5.2 Introduction

Due to their multiple valence states, high capacitance, low cost, and chemical stability, transition metal oxides are used to fabricate electrodes for electrochemical supercapacitors. Interest has been focused on individual oxides, such as MnO_2 , Mn_3O_4 , Fe_2O_3 , Fe_3O_4 , Co_3O_4 , NiO [1-6] and complex oxides [7-9]. There are excellent reviews, which describe advanced materials, charging mechanisms, electrode design and performance of metal oxide based supercapacitors [3, 4, 7, 10].

A major problem in the development of metal oxide supercapacitor technology is poor electrode performance at commercially desirable high active mass (AM) loadings [11]. Many metal oxide materials showed outstanding capacitive properties, such as high gravimetric capacitance (F g^{-1}) and low impedance, only for AM lower than 1 mg cm^{-2} . However, the total capacitance of such electrodes is low. Moreover, the electrodes show very low ratio of active material mass to the mass of current collector (R_m). Thin films with active mass $< 1 \text{ mg cm}^{-2}$ on metal foil substrates have $R_m < 0.01$ [12]. The devices with low AM have low total capacitance and high total mass, which includes mass of active materials, electrolyte, current collectors and other passive components. The AM loading for practical applications must be above $10\text{--}20 \text{ mg cm}^{-2}$ [13-15]. However, it is challenging to achieve good electrochemical performance at high AM.

A significant decrease in specific capacitance with increasing capacitive material AM results from the poor electronic and ionic conductivities [11] of metal oxide based electrodes. Therefore, advanced technologies must be developed for the synthesis of

nanoparticles and their mixing with conductive additives on the nanometer scale. The modification of chemical composition is another important avenue for the development of advanced materials. It is important to note that tremendous progress in the development of advanced ceramic materials in different fields has been achieved by the synthesis of solid solutions, which exhibited superior properties. Advanced spinel solid solutions have been developed for magnetic applications [16, 17], batteries [18, 19], photoelectrochemical, and photocatalytic applications [20, 21].

Spinel-type oxide materials are of interest for supercapacitors [9, 22]. Such materials can be prepared by chemical precipitation at room temperature [22, 23]. Spinel solid solutions can be synthesized at room temperature or at relatively low temperatures under hydrothermal conditions [24]. The ability to form individual spinel compounds and solid solutions by chemical precipitation allows the fabrication of nanoparticles of controlled size. The synthesis of Mn_3O_4 spinel offers very promising processing advantages for the fabrication of positive electrodes of supercapacitors. For comparison, MnO_2 is another very promising cathode material, which is usually prepared by the reduction of Mn^{7+} in permanganate solutions. However, permanganates react with organic capping agents and conductive carbon additives. Such reactions result in decomposition of the capping agents and conductive additives. Therefore, organic capping agents cannot be used for the modification of particle size and morphology during synthesis. As a result, there has been limited progress in the fabricating MnO_2 nanoparticles of small size for design of advanced nanocomposite. The decomposition of carbon additives in chemical reactions with permanganates results in their oxidation and conversion to CO_2 gas. Therefore, conductive

additives cannot be added during synthesis. This limitation is detrimental for the formation of advanced nanocomposite with improved mixing of the individual components. In contrast, Mn_3O_4 can be produced from Mn^{2+} solutions in the presence of capping agents, which limit particle growth. Moreover, the use of Mn^{2+} precursors paves the way for the fabrication of advanced composites using new techniques for synthesis, co-dispersion and enhanced mixing of the individual components. Recent studies [23] Showed that capacitance of Mn_3O_4 -CNT cathodes, prepared using capping agents and advanced colloidal techniques, was higher than the capacitance of MnO_2 -CNT cathodes at AM loading of 33 mg cm^{-2} . Mn_3O_4 forms spinel solid solutions, which are promising for the modification of electrode properties.

Fe_3O_4 is another promising spinel material for negative electrodes. Asymmetric devices, containing Fe_3O_4 as a negative electrode and MnO_2 as a positive electrode have an enlarged voltage window of 1.8 V in aqueous K_2SO_4 electrolyte. A capacitance of 50 F g^{-1} has been reported at mass loading of 8.8 mg cm^{-2} for composite Fe_3O_4 -based electrodes [25]. However, the gravimetric capacitance of the negative electrodes was significantly lower than that of the positive electrodes. Matching the total capacitances of the individual electrodes generates a need in significantly larger AM of the negative electrode, compared to the AM of the positive electrode. Therefore, the specific capacitance of the negative electrodes must be increased. Moreover, good performance must be achieved at high AM.

The objective of this investigation was to fabricate spinel-spinel asymmetric supercapacitor devices using spinel Fe_3O_4 and Mn_3O_4 materials for anodes and cathodes, respectively. Our new approach is based on the application of Celestine blue (CB) as a

multifunctional capping dispersant for the synthesis of spinel phases in the presence of dispersed CNT, which were used as conductive additives. This approach resulted in the formation of spinel nanoparticle decorated CNT. Celestine blue (CB) was used as a charge transfer mediator, which allowed for significant capacitance enhancement. Good nanotube dispersion was achieved using CB as an efficient aromatic dispersant, offering the advantages of good adsorption on CNT, small size and ability to disperse CNT at low CB dispersant concentrations. The positive charge and chelating properties of CB promoted spinel phase formation on the surface of CNT due to chemical bonding and electrostatic heterocoagulation mechanisms.

Moreover, CB acted as a capping agent, which allowed for the particle size reduction. Good performance of the electrodes was achieved at AM of 40 mg cm^{-2} . We achieved exceptionally high capacitance of the negative electrodes, which facilitated the development of advanced asymmetric devices.

5.3 Experimental procedures

Iron (II) chloride tetrahydrate ($\text{FeCl}_2 \cdot 4\text{H}_2\text{O}$), iron (III) chloride hexahydrate ($\text{FeCl}_3 \cdot 6\text{H}_2\text{O}$), manganese nitrate tetrahydrate ($\text{Mn}(\text{NO}_3)_2 \cdot 4\text{H}_2\text{O}$), ammonium hydroxide (NH_4OH), sodium hydroxide (NaOH), sodium sulfate (Na_2SO_4), Celestine blue (CB) and polyvinyl butyral (PVB, average MW = 50–80 kDa) were purchased from Sigma Aldrich. Multiwalled carbon nanotubes (CNT, purity > 95%, OD 20–30 nm, and length 1–2 μm) were purchased from US Nanomaterial Inc, USA. Vale Ltd., Canada, supplied Ni foam (porosity of 95%).

Nanoparticles of Fe_3O_4 were prepared by chemical precipitation. The stoichiometric amounts of Fe^{2+} and Fe^{3+} salts were dissolved in DI water, and the pH of the solution was adjusted to $\text{pH} = 9$ by adding NH_4OH . The reaction was carried out at $70\text{ }^\circ\text{C}$ with a supply of N_2 gas. The mixed Fe_3O_4 and CNT sample was prepared by dispersing 1 g L^{-1} of CNT in DI water and ultrasonicated for 45 min. Subsequently, 0.25 g L^{-1} of CB was added to the CNT suspension, which was then ultrasonicated for 15 min, 1 g L^{-1} Fe_3O_4 in aqueous solution was then mixed with 1 g L^{-1} CNT suspension, containing CB, and ultrasonicated for 60 min. The dispersion was filtrated, washed, and dried overnight in an oven at $60\text{ }^\circ\text{C}$. A similar procedure was carried without CB to analyze the influence of CB on the electrode performance.

For the in-situ synthesis of Fe_3O_4 in the presence of CNT and CB, a 1 g L^{-1} CNT suspension, containing 0.25 g L^{-1} CB was initially prepared. Stoichiometric amounts of Fe^{2+} and Fe^{3+} salts were dissolved in DI water, and added to the CNT suspensions to obtain oxide/CNT mass ratio γ of 1, 1.25, 1.5, and 2.0. The synthesis procedure was similar to that for pure Fe_3O_4 , as it was described above. Table 5.1 (Supporting information) presents data on the composition of the tested samples and methods of their preparation. The synthesis of Mn_3O_4 nanoparticles has been previously described [26]. Similar to Fe_3O_4 -CNT composites, the Mn_3O_4 -CNT composites with different γ were also prepared by in-situ synthesis of Mn_3O_4 in the presence of CNT, that were dispersed using CB. To fabricate the electrodes, the dried Fe_3O_4 -CNT and Mn_3O_4 -CNT composites were dispersed in ethanol containing 3% PVB. The obtained slurry was used to impregnate Ni foam current collectors. The active mass loading of the electrodes was 40 mg cm^{-2} .

Transmission electron microscopy was performed using a JEOL 2010F field emission microscope. The elemental analysis was done using energy dispersive X-ray spectroscopy (EDX). X-ray diffraction (XRD) analysis was performed using the Bruker D8 DISCOVER instrument comprising DAVINCI diffractometer and Co-K α radiation. Raman spectroscopy analysis was carried out using Renishaw InVia Raman Spectrometer and a laser excitation wavelength of 514 nm (Spectra Physics Lasers, USA).

Cyclic voltammetry (CV) and alternating current (AC) electrochemical impedance spectroscopy (EIS) of the single electrodes and asymmetric devices were performed as described in prior investigations [12, 27]. Galvanostatic charge–discharge was performed using Biologic VMP 300 potentiostat at current densities of 3, 5, 7, and 10 mA cm⁻². The charge-discharge behavior of the asymmetric devices, containing Mn₃O₄-CNT positive electrodes and Fe₃O₄-CNT negative electrodes was evaluated using battery analyzers BST8-MA and BST8-3 (MTI Corporation, USA) at current densities of 3–50 mA cm⁻². Areal capacitance C_s (F cm⁻²) and mass normalized capacitance C_m (F g⁻¹) were calculated from the CV and galvanostatic charge-discharge data as described in prior investigations [12, 27]. Complex AC capacitance $C^* = C' - iC''$ was calculated from the impedance data [12, 27].

5.4 Results and discussion

Fe₃O₄ is a promising charge-storage material for supercapacitor anodes. However, it is challenging to achieve good performance of this material at high AM. The development of advanced anodes with high AM requires the fabrication of non-agglomerated Fe₃O₄ particles, which must be well mixed with dispersed CNT. Charge transfer between Fe₃O₄

and conductive additives is one of the challenges in the design of electrodes with high AM.

Metal oxide nanoparticles and CNT are prone to agglomeration due to their high surface area. In aqueous processing techniques, the surface condensation reactions of OH^- groups promote the formation of hard agglomerates of metal oxide nanoparticles. In the case of ferrimagnetic Fe_3O_4 , particle agglomeration is further enhanced through inter-particle magnetic attraction. These challenges were addressed by the development of Fe_3O_4 -decorated CNT using CB mediated in-situ synthesis. We report multiple findings that demonstrate the benefits of CB for fabricating advanced electrodes with enhanced performance at high AM.

Figure 5.1 (A) shows the chemical structure of CB. The polyaromatic structure of CB is beneficial for its adsorption on CNT. The CB adsorption mechanism is based on the formation of π -bonds. The small size of the CB molecule and its strong adsorption on CNT facilitated the CNT dispersion Figure 5.1 (B) by unzipping mechanism [28]. The interaction of CB with Fe_3O_4 particles can involve two possible mechanisms Figure 5.1(C). One mechanism is based on the chelating catechol-type CB bonding to the Fe atoms on the surface of Fe_3O_4 particles Figure 5.1 (C). Recent studies highlighted unique benefits of this bonding mechanism, which was used for the development of advanced chelating dispersants [29]. The interest in the catechol-type bonding resulted from the investigations of strong mussel's proteins adsorption on inorganic surfaces. Another mechanism involves the electrostatic interactions. The synthesis of Fe_3O_4 was performed at $\text{pH} = 9-10$ which is higher than the isoelectric point ($\text{pH} = 6.5$) [30] of this material. As a result, the synthesized particles were negatively charged and attracted cationic to CB.

In this investigation, we dispersed CNT using CB and then performed in-situ synthesis of Fe_3O_4 in the presence of dispersed CNT. The CB-CNT and CB- Fe_3O_4 interactions led to the formation of Fe_3O_4 -decorated CNT (FDCNT), as it is shown schematically in Figure 5.1 (D).

The formation of FDCNT allowed for improved contact of capacitive Fe_3O_4 and conductive CNT. Moreover, it will be shown below that catechol- type bonding of CB to Fe_3O_4 particles Figure 5.1 (C) and redox properties of CB, described by a reaction presented in Figure 5.1(E), facilitated charge transfer.

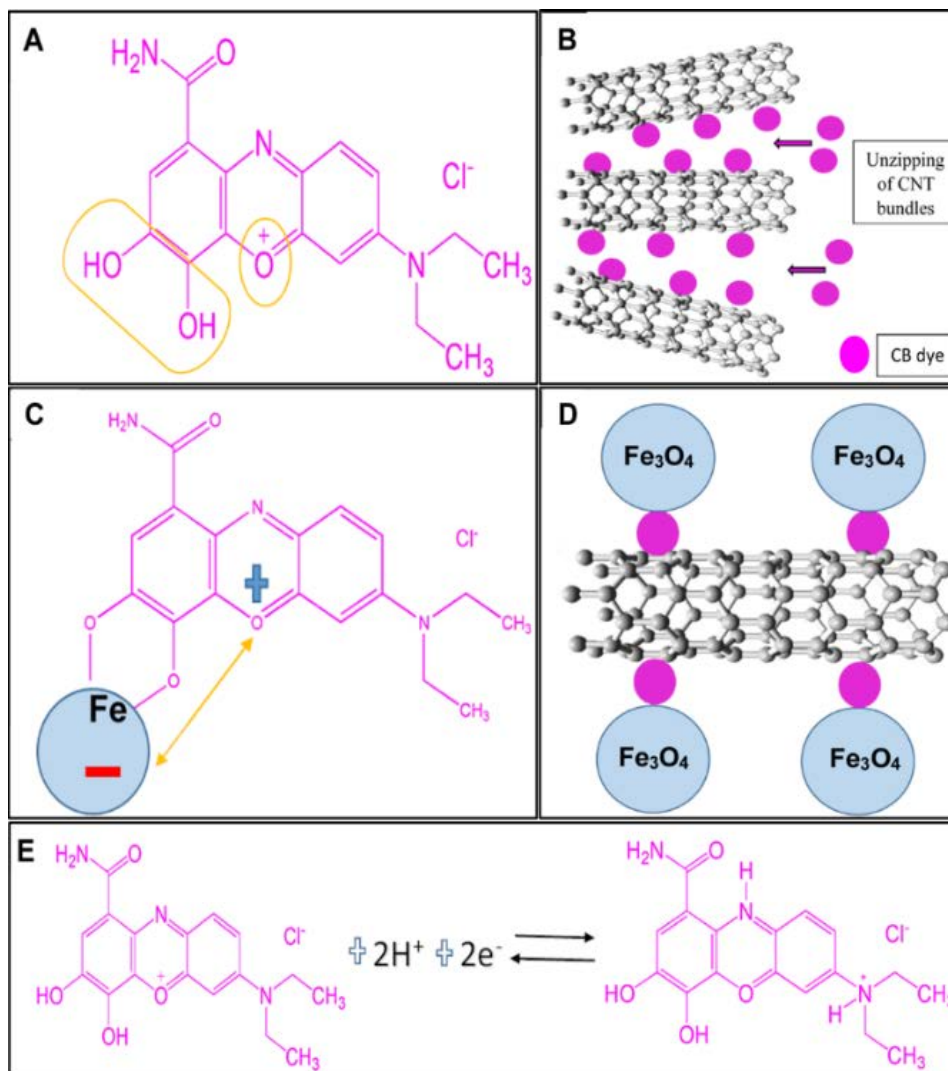


Figure 5.1 (A) chemical structure of cationic CB, containing a chelating catechol group, (B) unzipping mechanism of CNT dispersion using CB, (C) interaction of CB with Fe_3O_4 particles: chelating bonding and electrostatic attraction, (D) schematic of Fe_3O_4 decorated CNT and CB interaction with both materials, (E) redox reaction of CB.

Figure 5.2 compares the XRD pattern of a mixture of CNT and Fe_3O_4 , prepared by a chemical precipitation method, with a diffraction pattern of FDCNT. The diffraction patterns show peaks corresponding to Fe_3O_4 (JCPDS file 19-0629) and CNT (JCPDS file 22-1012) for both samples.

The broadening of the Fe_3O_4 diffraction peaks for FDCNT is attributed to low crystallite size. The observed broadening could be attributed to the effect of CB, which acted as a capping agent. The peak broadening resulted in reduced relative intensity of the Fe_3O_4 peaks. Changes in the relative intensity of the FDCNT peaks, compared to the mixture of CNT and Fe_3O_4 can also result from a texture of the FDCNT composite material. The decrease in the crystallite size could lead to improved electrochemical performance.

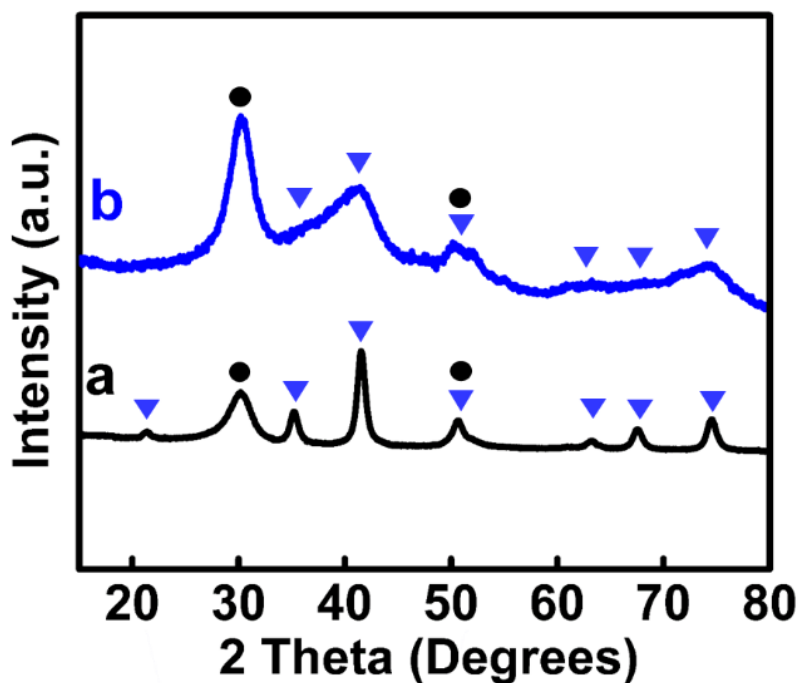


Figure 5.2 X-ray diffraction patterns of (a) mixture of Fe_3O_4 and CNT prepared without CB and (b) FDCNT (▼-JCPDS file No. 19-0629, ●-JCPDS No. 22-1012).

Raman spectroscopy studies were performed for as-received CNT, synthesized Fe_3O_4 , a mixture of Fe_3O_4 and CNT, as-received CB and the synthesized FDCNT (Figure 5.3). The Raman spectrum for CNT reveals the in-plane vibration of the C–C bond at 1592 cm^{-1} (G-band), the disordered D-band at 1354 cm^{-1} and G' band at 2702 cm^{-1} (overtone of D-

band) [31]. The Fe_3O_4 spectrum shows a peak at $\sim 698\text{ cm}^{-1}$ corresponding to A_{1g} mode [32]. The same bands were observed in the Raman spectrum of the Fe_3O_4 -CNT mixture and FDCNT. The Raman spectra of CB dye is analogous to the different organic dyes with a peak at low wavenumber and multiple peaks in the mid wavenumber range [33, 34]. These peaks were observed in the spectrum of FDCNT and confirmed the incorporation of CB into FDCNT.

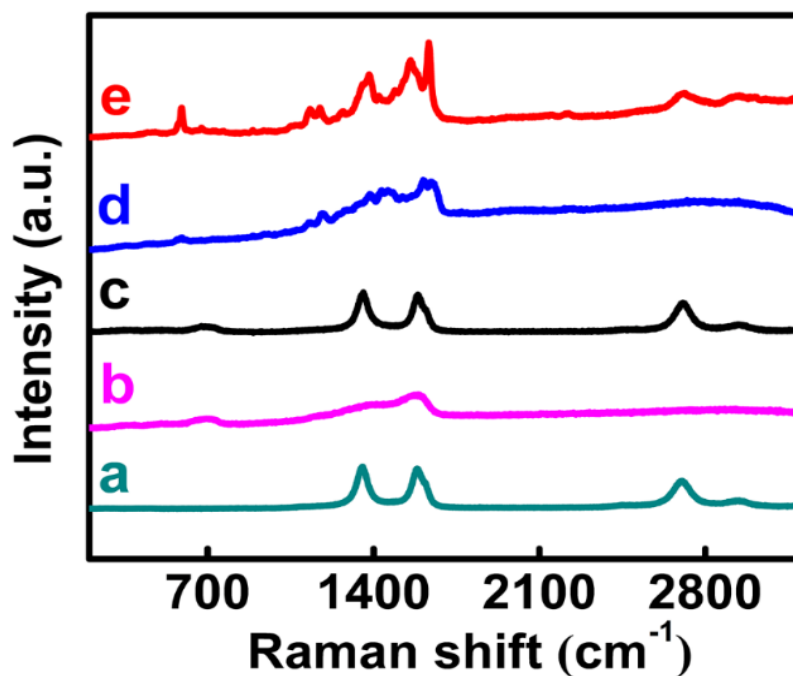


Figure 5.3 Raman spectroscopy data for (a) as-received CNT (b) precipitated Fe_3O_4 , (c) mixture of Fe_3O_4 and CNT, (d) CB dye, and (e) FDCNT for $\gamma = 1.50$.

Investigations of the effect of Fe_3O_4 /CNT mass ratio (γ) on the FDCNT morphology and electrochemical properties are important for the optimization of electrode performance. Fe_3O_4 offers benefits of high capacitance, whereas CNT provide electronic conductivity. The ability to avoid Fe_3O_4 and CNT agglomeration is critical for the design of composites

with enhanced charge storage properties. The STEM images at different magnifications Figure 5.4 (A, B) for FDCNT with $\gamma = 1.5$ show Fe_3O_4 nanoparticles present on the surface of CNT. The sizes of the nanoparticles are ~ 20 nm. As γ increases to 2.0, the nanoparticles form large agglomerates, as it is evident from Figure 5.4 (C). Energy dispersive X-ray analysis was used to perform line scans on the FDCNT surfaces Figure 5.4 (B). The EDX data Figure 5.4 (D) confirmed the deposition of Fe_3O_4 on CNT.

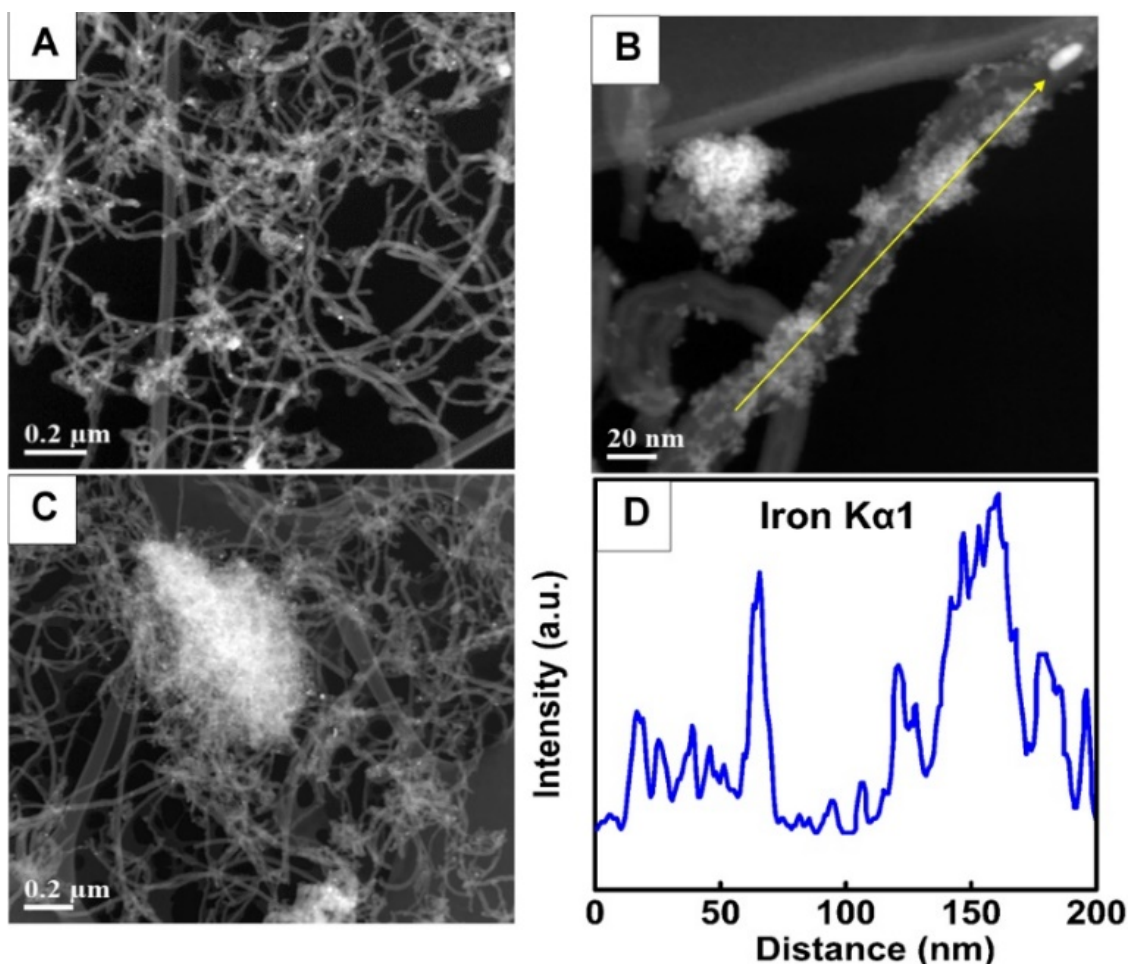


Figure 5.4 TEM of FDCNT for different (γ): (A, B) 1.50, and (C) 2.00. (D) EDX line scan for Fe, the line is shown in (B).

Electrodes prepared without CB showed relatively small CV areas Figure 5.5 A (a, b) indicating low capacitance Figure 5.5 B (a, b). The use of CB as a dispersant resulted in significant increase of the CV areas Figure 5.5 A (c, d) and higher capacitances Figure 5.5 B (c, d). The physical mixing of CNT with Fe_3O_4 particles, which were dried after chemical precipitation, resulted in relatively low capacitances. The in-situ precipitation of Fe_3O_4 in the presence of CNT allowed for improved mixing and higher capacitance. FDCNT electrodes, prepared using CB, showed the highest capacitance. Moreover, FDCNT electrodes exhibited lower resistance and higher real part of AC capacitance (C_s') Figure 5.5 (C, D). The AC relaxation frequency, corresponding to the maximum of the imaginary part of AC capacitance C_s'' , was above 10 mHz Figure 5.5 (E).

The supercapacitor electrodes prepared with CB showed significant capacitance increase in the range of 0 to -0.5 V. It is important to note that CB is a redox active material. However, the observed capacitance enhancement cannot be attributed to direct contribution of adsorbed CB to the charge storage due to the redox reaction shown in Figure 5.1 (E). The gravimetric capacitance of CB related to this reaction is very low due to the relatively large mass of CB. Therefore, we suggested that CB additive facilitates charge transfer between Fe_3O_4 and CNT and allows for better utilization of the charge storage properties of Fe_3O_4 .

It is known that CB is an efficient redox-type charge transfer mediator for electrocatalysis [35], where it is used to shuttle electrons between electrodes and analytes. CB has redox properties Figure 5.1 (E) in a negative potential range and offers benefits of high electron transfer rate constant, excellent reversibility and chemical stability [35].

The chelating bonding of CB to Fe_3O_4 and electrostatic interactions of CB and Fe_3O_4 are beneficial for stable redox performance in the negative potential range.

In addition to the redox-type mode of the charge transfer mediation, we also can suggest another mechanism, which can facilitate the charge transfer. This mechanism is related to the catechol-type CB bonding to Fe_3O_4 . Catechol-type molecules are widely used as charge transfer mediators in different fields. In the field of anodic electropolymerization of polypyrrole, catechol-type dopants facilitated charge transfer by creation of bonds to different substrates [36-38] and significantly reduced the anodic electropolymerization potential. As a result, adherent films were obtained on non-noble substrates [36 - 38]. In the field of biosensors and photovoltaic devices the charge transfer complexes [39 - 41] were formed by coordinating catechol with titanium atoms on the TiO_2 particle surface. Catechol-type materials are used as electron transfer mediators in advanced sensors [42]. Therefore, we suggested that catechol-type CB bonding could also facilitate charge transfer between Fe_3O_4 and CNT. The increase in capacitance of FDCNT can result from the ability of CB to facilitate electron transfer by either of two different mechanisms described above

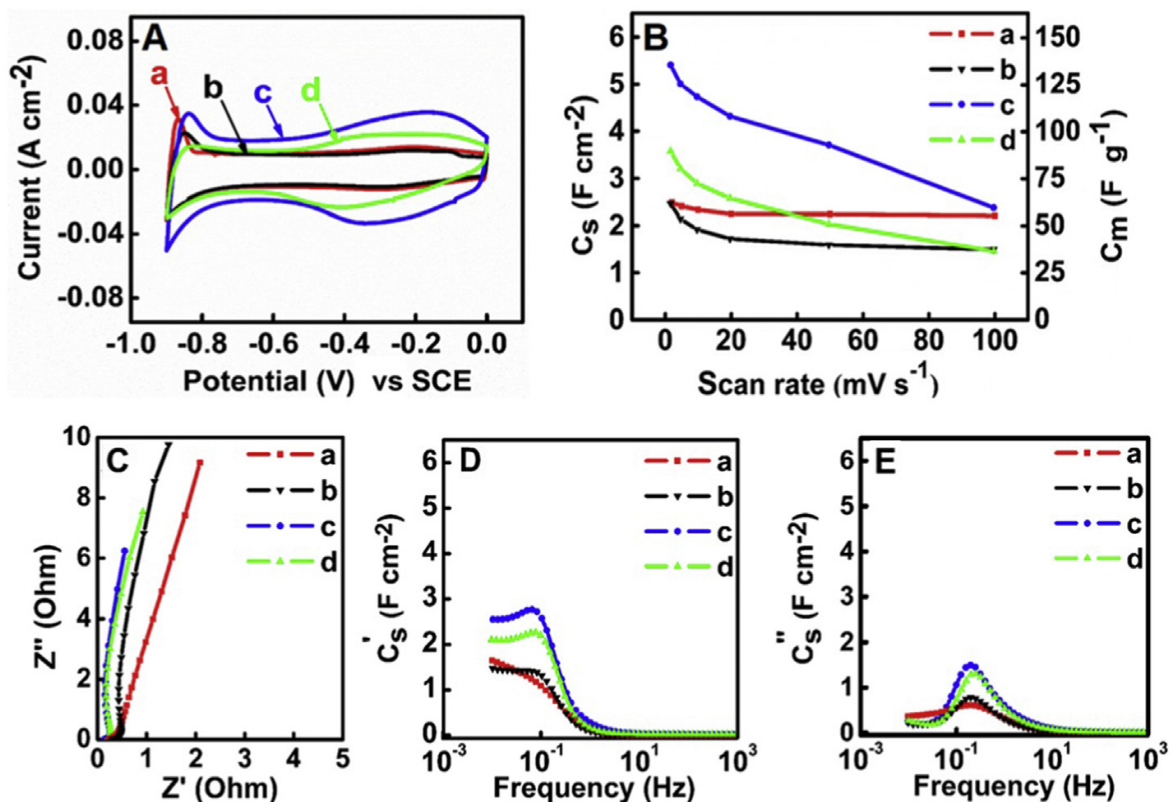


Figure 5.5. (A) CVs at scan rate of 5 mV s⁻¹, (B) C_s and C_m versus scan rate, (C) EIS Nyquist plot, (D) C_s' versus frequency and (E) C_s'' versus frequency for electrodes with $\gamma=1.00$, prepared (a, b) without CB and (c, d) with CB using different methods: (a, c) in-situ chemical precipitation and (b, d) mixing.

The investigation of FDCNT electrodes fabricated with different γ provided additional evidence of influence of CB mediated in-situ synthesis on the capacitive behavior. The CV profiles for the electrodes with different γ are presented in Figure 5.6 (A-C). The CV area of the electrode with $\gamma = 1.5$ is higher than those with $\gamma = 1.25$ and $\gamma = 2$. The electrode with $\gamma = 1.5$ shows Figure 5.6 (D) the highest capacitance of 6.17 F cm⁻² (154.3 F g⁻¹) at 2 mV s⁻¹. The retention of capacitance for $\gamma = 1.5$ was 37.9 %. The obtained areal capacitance was significantly higher than the literature data for Fe₃O₄ based electrodes, which were summarized in reviews [2, 43, 44].

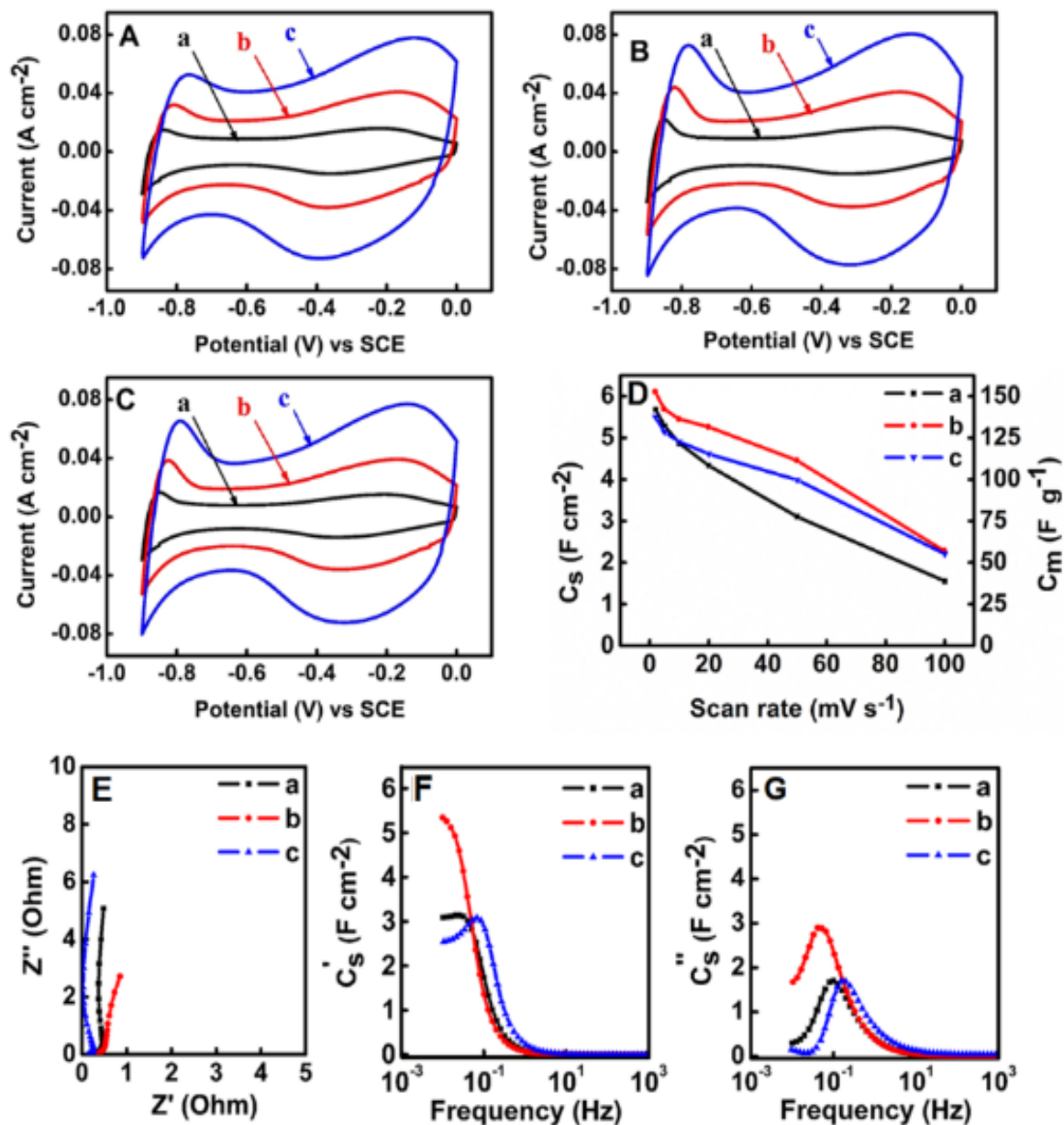


Figure 5.6 Testing data for FDCNT electrodes: (A-C) CVs at scan rates of (a) 2, (b) 5, and (c) 10 mV s⁻¹ with (A) $\gamma=1.25$, (B) $\gamma=1.50$, and (C) $\gamma= 2.00$; (D) C_s and C_m versus scan rate. (E) Nyquist plot of complex impedance and frequency dependences of (F) C_s' and (G) C_s'' for D(a), E(a), F(a), G(a) $\gamma=1.25$; D(b), E(b), F(b), G (b) $\gamma=1.50$, and D(c), E(c), F(c), G(c) $\gamma= 2.00$.

The FDCNT electrode with $\gamma = 1.5$ showed the highest capacitance and the highest capacitance retention at different scan rates compared to other electrodes. Galvanostatic charge-discharge was performed on this optimized electrode. The charge-discharge curves at various current densities in (Figure 5.7) (inset) showed nearly symmetrical triangular shapes. The capacitance calculated from the chronopotentiometry data is presented in (Figure 5.7). The highest capacitance of 4.97 F cm^{-2} was obtained at a discharge current of 3 mA cm^{-2} .

The fibrous microstructure of the electrode materials and magnetic interactions of Fe_3O_4 particles facilitated the fabrication of electrodes with relatively low binder content, which was 3% of the total mass of Fe_3O_4 and CNT. A polymer binder is an important component of the composite electrodes. However, insufficient attention has been paid in the literature to the minimization of binder content in supercapacitor composites. Polymer binders have significantly lower densities than the densities of functional metal oxides. Therefore, volume fractions of binders in composites are high even at relatively low mass concentration of the binders. Many water-insoluble polymers exhibit insulating and hydrophobic properties, which are detrimental for the electrode performance. Therefore, it is important to reduce the volume fraction of the binders in composite electrodes.

The testing results presented above indicate that CB mediated in-situ synthesis produces advanced Fe_3O_4 based anodes. A similar approach (see the supplementary information) has been utilized to fabricate Mn_3O_4 based cathodes that showed a capacitance of 5.15 F cm^{-2} at an AM of 40 mg cm^{-2} .

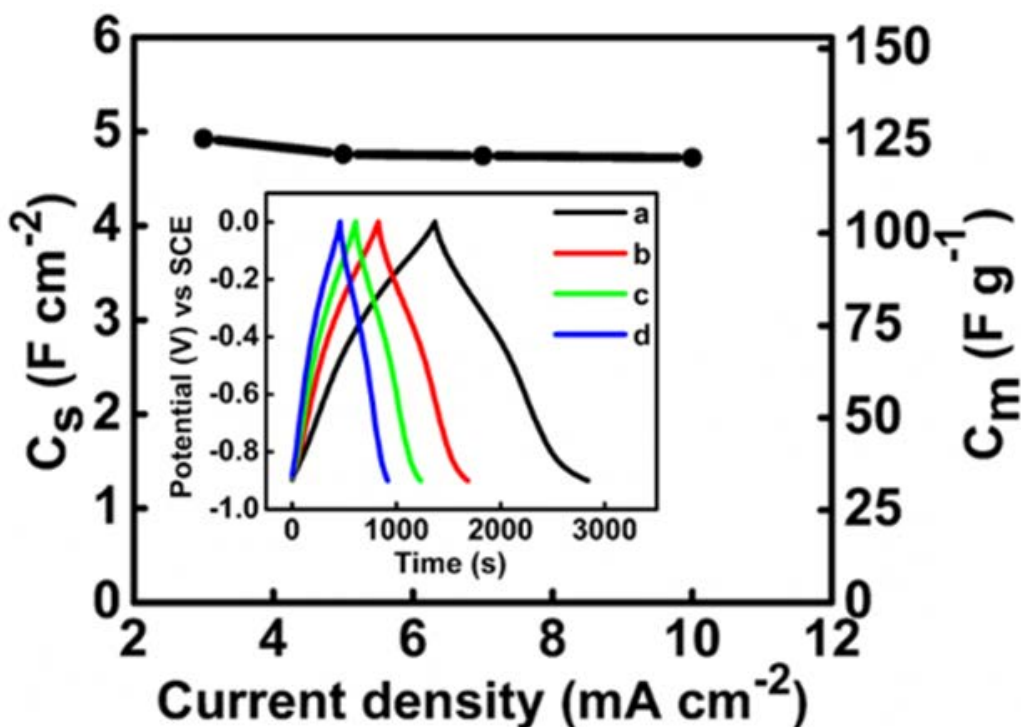


Figure 5.7 C_s and C_m versus scan rate for FDCNT electrodes with $\gamma=1.50$ obtained from charge-discharge curves (inset) at current densities of (a) 3, (b) 5, (c) 7, and (d) 10 mA cm⁻².

Spinel based cathodes and anodes, prepared by in-situ precipitation methods using CB were used to fabricate an asymmetric device for operation in a voltage window of 1.6 V. The device exhibited box-type capacitive CV profiles Figure 5.8 (A). The highest areal capacitance obtained for the device was 2.41 F cm⁻² at 2 mV s⁻¹. The capacitance decreased to 0.61 F cm⁻² at 100 mV s⁻¹ with a capacitance retention of 21.5%. The Nyquist plot showed a low impedance. The relaxation frequency of the asymmetric device was lower than that for the individual electrodes. The smaller relaxation frequency can result from higher total resistance of the device than the resistances of the individual electrodes.

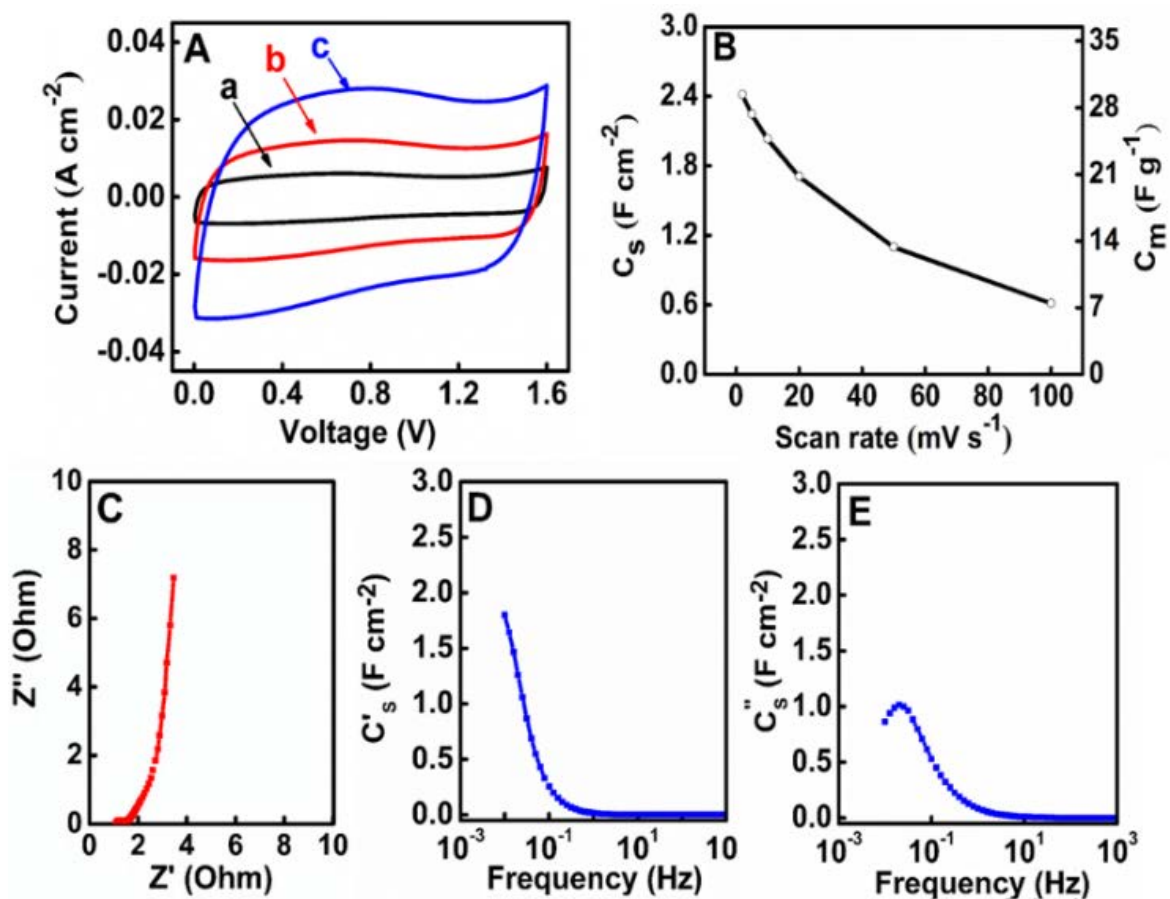


Figure 5.8 (A) CVs at scan rates of (a) 2, (b) 5 and (c) 10 mV s^{-1} , (B) C_s and C_m versus scan rate, (C) Nyquist plot of complex impedance and frequency dependences of (D) C_s' and (E) C_s'' for an asymmetric supercapacitor cell.

The asymmetric device Figure 5.9 (A) displayed ideal triangular shape chronopotentiometry graphs at all current densities in the 3–50 mA cm^{-2} range. The areal capacitance of 2.29 F cm^{-2} was obtained at a current density of 3 mA cm^{-2} . The capacitance decreased with current density, the retention at a current density of 50 mA cm^{-2} was 83.3%. The chronopotentiometry graphs were used to calculate the energy density and power density at varied current densities.

Figure 5.9 (B) shows the Ragone plot of the asymmetric device with the highest energy density of 0.91 mWh cm^{-2} obtained at a current density of 3 mA cm^{-2} and highest power density of 26.77 mW cm^{-2} achieved at current density of 50 mA cm^{-2} . The high power-energy density device characteristics were achieved at high AM.

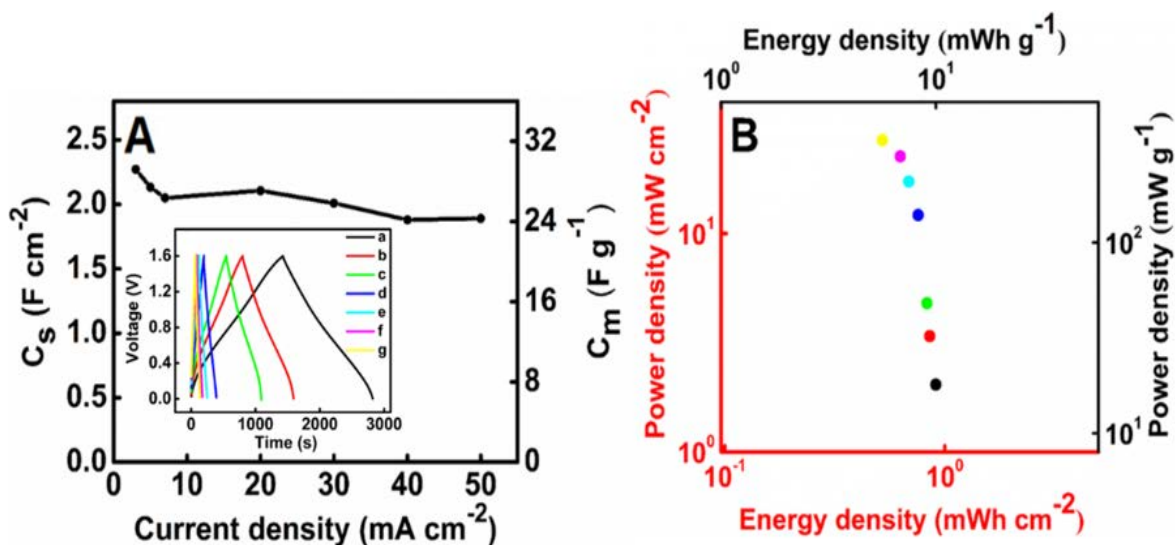


Figure 5.9 (A) C_s and C_m versus charge-discharge rate, obtained from charge-discharge curves (inset) at current densities of (a) 3, (b) 5, (c) 7, (d) 20, (e) 30, (f) 40, and (g) 50 mA cm^{-2} , (B) Ragone plot for an asymmetric supercapacitor cell.

5.5 Conclusions

An asymmetric spinel-spinel supercapacitor has been fabricated using Fe_3O_4 and Mn_3O_4 for charge storage in negative and positive electrodes, respectively, and CNT as a conductive additive. High performance of the individual electrodes and devices has been achieved at a high AM of 40 mg cm^{-2} for the individual electrodes. A conceptually new strategy has been developed, which was based on the use of multifunctional CB dye. CB strongly adsorbed on the spinel phases and CNT, facilitated CNT dispersion, acted as a

capping agent for the synthesis of spinel particles and allowed for the fabrication of spinel decorated CNT. Moreover, it was discovered that CB is an efficient charge transfer mediator, which allowed for significant improvement of capacitive behavior. The use of CB as a charge transfer mediator allowed for good utilization of capacitive properties of spinels at high AM. The mechanisms of spinel-CB-CNT interactions involved π - π interactions of CB and CNT and catechol-type chelating bonding of CB with metal atoms on the spinel particle surface. The charge transfer mediation mechanisms are based on redox properties of CB and catechol-type bonding. The capacitive properties were analyzed with cyclic voltammetry, chronopotentiometry and impedance spectroscopy for the electrodes with different spinel/CNT mass ratios. Areal capacitances of 6.17 and 5.15 F cm^{-2} were obtained for Fe_3O_4 and Mn_3O_4 based electrodes, respectively in 0.5 M Na_2SO_4 electrolyte. These high capacitances were achieved at low electrode resistances. The electrodes were used for the fabrication of an asymmetric device with a capacitance of 2.41 F cm^{-2} in a voltage window of 1.6 V.

5.6 Declaration of competing interest

The authors declare that they have no known competing financial interests or personal relationships that could have appeared to influence the work reported in this paper.

5.7 Acknowledgements

The authors gratefully acknowledge the Natural Sciences and Engineering Research Council of Canada and Canadian Centre for Electron Microscopy.

5.8 References

- [1] V.D. Nithya, N.S. Arul, Review on $\text{-Fe}_2\text{O}_3$ based negative electrode for high performance supercapacitors, *Journal of Power Sources* 327 (2016) 297-318.
- [2] C.D. Lokhande, D.P. Dubal, O. S. Joo, Metal oxide thin film based supercapacitors, *Current Applied Physics* 11(3) (2011) 255-270.
- [3] B. Xu, M. Zheng, H. Tang, Z. Chen, Y. Chi, L. Wang, L. Zhang, Y. Chen, H. Pang, Iron oxide-based nanomaterials for supercapacitors, *Nanotechnology* 30(20) (2019).
- [4] J.-G. Wang, F. Kang, B. Wei, Engineering of MnO_2 -based nanocomposites for high-performance supercapacitors, *Progress in Materials Science* 74 (2015) 51-124.
- [5] W. Xi, T. Wei, Z. Tianyou, Z. Chunyi, Y. Bando, D. Golberg, Cobalt(II,III) oxide hollow structures: Fabrication, properties and applications, *Journal of Materials Chemistry* 22(44) (2012) 23310-26.
- [6] Y. Su, I. Zhitomirsky, Hybrid MnO_2 /carbon nanotube-VN/carbon nanotube supercapacitors, *Journal of Power Sources* 267 (2014) 235-242.
- [7] D. Chen, Q. Wang, R. Wang, G. Shen, Ternary oxide nanostructured materials for supercapacitors: A review, *Journal of Materials Chemistry A* 3(19) (2015) 10158-10173.
- [8] Y. Liu, I. Zhitomirsky, Electrochemical supercapacitor based on multiferroic BiMn_2O_5 , *Journal of Power Sources* 284 (2015) 377-382.
- [9] W. Chenggang, E. Zhou, H. Weidong, D. Xiaolong, H. Jinzhao, D. Meng, W. Xianqi, L. Xiaojing, X. Xijin, NiCo_2O_4 -Based Supercapacitor Nanomaterials, *Nanomaterials* 7(2) (2017) 41 (23 pp.).
- [10] P. Simon, Y. Gogotsi, *Materials for electrochemical capacitors*, World Scientific Publishing Co.2010, pp. 138-147.
- [11] Y. Gogotsi, P. Simon, True performance metrics in electrochemical energy storage, *Science* 334(6058) (2011) 917-918.

- [12] Y. Zhu, K. Shi, I. Zhitomirsky, Polypyrrole coated carbon nanotubes for supercapacitor devices with enhanced electrochemical performance, *J. Power Sources* 268 (2014) 233-239.
- [13] A.-L. Brisse, P. Stevens, G. Toussaint, O. Crosnier, T. Brousse, (OH Ni, 2 and NiO based composites: battery type electrode materials for hybrid supercapacitor devices, *Materials* 11 (7) (2018) 1178.
- [14] W. Gu, G. Yushin, Review of nanostructured carbon materials for electrochemical capacitor applications: advantages and limitations of activated carbon, carbide - - derived carbon, zeolite - templated carbon, carbon aerogels, carbon nanotubes, onion - like carbon, and graphene, *Wiley Interdisciplinary Reviews: Energy Environ.* 3 (5) (2014) 424-473.
- [15] L. Wei, G. Yushin, Nanostructured activated carbons from natural precursors for electrical double layer capacitors, *Nano Energy* 1 (4) (2012) 552-565.
- [16] R.J. Harrison, A. Putnis, The magnetic properties and crystal chemistry of oxide spinel solid solutions, *Surveys in Geophysics* 19(6) (1999) 461-520.
- [17] O. Pena, X. Cailleaux, B. Piriou, M. del Canto, S. Abarca, E. Rios, J. Ortiz, J.L. Gautier, P.N. Lisboa-Filho, C. Moure, Magnetic properties of $\text{Cu}_{1+x}\text{Mn}_{2-x}\text{O}_4$ and $\text{Ni}_{1+x}\text{Mn}_{2-x}\text{O}_4$ solid solutions, *Journal of the European Ceramic Society* 27(13-15) (2007) 3911-3914.
- [18] R. Santhanam, B. Rambabu, Research progress in high voltage spinel $\text{LiNi}_{0.5}\text{Mn}_{1.5}\text{O}_4$ material, *Journal of Power Sources* 195(17) (2010) 5442-5451.
- [19] Y. Jaesang, K. Donghwi, U. Ji Hyun, J. Mihee, O. Woong, Y. Won-Sub, Effect of local structural changes on rate capability of $\text{LiNi}_{0.5}\text{Mn}_{1.5}\text{O}_4$ - cathode material for lithium ion batteries, *Journal of Alloys and Compounds* 686 (2016) 593-600.
- [20] L.G.J. de Haart, G. Blasse, Photoelectrochemical properties of ferrites with the spinel structure, *Solid State Ionics* 16 (1985) 137-139.

- [21] X. Xiaoxiang, X. Yinghao, N. Shuang, A.K. Azad, C. Tongcheng, Photocatalytic H₂ production from spinels ZnGa_{2-x}Cr_xO₄ (0<x<2) solid solutions, *Journal of Solid State Chemistry* 230 (2015) 95-101.
- [22] M. Nawwar, R. Poon, R. Chen, R.P. Sahu, I.K. Puri, I. Zhitomirsky, High areal capacitance of Fe₃O₄-decorated carbon nanotubes for supercapacitor electrodes, *Carbon Energy* (2019).
- [23] J. Milne, I. Zhitomirsky, Application of octanohydroxamic acid for liquid-liquid extraction of manganese oxides and fabrication of supercapacitor electrodes, *Journal of colloid and interface science* 515 (2018) 50-57.
- [24] C. Wang, E. Zhou, W. He, X. Deng, J. Huang, M. Ding, X. Wei, X. Liu, X. Xu, NiCo₂O₄-based supercapacitor nanomaterials, *Nanomaterials* 7(2) (2017) 41.
- [25] T. Brousse, D. Bélanger, A Hybrid Fe₃O₄ MnO₂ Capacitor in Mild Aqueous Electrolyte, *Electrochemical and Solid-State Letters* 6(11) (2003) A244-A248.
- [26] J. Milne, R.M. Silva, I. Zhitomirsky, Surface modification and dispersion of ceramic particles using liquid-liquid extraction method for application in supercapacitor electrodes, *Journal of the European Ceramic Society* 39 (2019) 3450-3455.
- [27] K. Shi, I. Zhitomirsky, Electrophoretic nanotechnology of graphene–carbon nanotube and graphene–polypyrrole nanofiber composites for electrochemical supercapacitors, *Journal of Colloid and Interface Science* 407 (2013) 474-481.
- [28] M.S. Ata, R. Poon, A.M. Syed, J. Milne, I. Zhitomirsky, New developments in non-covalent surface modification, dispersion and electrophoretic deposition of carbon nanotubes, *Carbon* 130 (2018) 584-598.
- [29] M. Ata, Y. Liu, I. Zhitomirsky, A review of new methods of surface chemical modification, dispersion and electrophoretic deposition of metal oxide particles, *Rsc Advances* 4(43) (2014) 22716-22732.

- [30] G.A. Parks, The isoelectric points of solid oxides, solid hydroxides, and aqueous hydroxo complex systems, *Chemical Reviews* 65(2) (1965) 177-198.
- [31] L. Bokobza, J. Zhang, Raman spectroscopic characterization of multiwall carbon nanotubes and of composites, *Express Polymer Letters* 6(7) (2012).
- [32] O.N. Shebanova, P. Lazor, Raman spectroscopic study of magnetite (FeFe_2O_4): a new assignment for the vibrational spectrum, *Journal of Solid State Chemistry* 174(2) (2003) 424-430.
- [33] H.E. Mayhew, D.M. Fabian, S.A. Svoboda, K.L. Wustholz, Surface-enhanced Raman spectroscopy studies of yellow organic dyestuffs and lake pigments in oil paint, *Analyst* 138(16) (2013) 4493-4499.
- [34] C.L. Brosseau, K.S. Rayner, F. Casadio, C.M. Grzywacz, R.P. Van Duyne, Surface-enhanced Raman spectroscopy: a direct method to identify colorants in various artist media, *Analytical chemistry* 81(17) (2009) 7443-7447.
- [35] A. Noorbakhsh, A. Salimi, E. Sharifi, Fabrication of Glucose Biosensor Based on Encapsulation of Glucose-Oxidase on Sol-Gel Composite at the Surface of Glassy Carbon Electrode Modified with Carbon Nanotubes and Celestine Blue, *Electroanalysis: An International Journal Devoted to Fundamental and Practical Aspects of Electroanalysis* 20(16) (2008) 1788-1797.
- [36] D. Tallman, C. Vang, G. Wallace, G. Bierwagen, Direct electrodeposition of polypyrrole on aluminum and aluminum alloy by electron transfer mediation, *Journal of the Electrochemical Society* 149(3) (2002) C173-C179.
- [37] S. Chen, I. Zhitomirsky, Influence of dopants and carbon nanotubes on polypyrrole electropolymerization and capacitive behavior, *Materials Letters* 98 (2013) 67-70.
- [38] C. Shi, I. Zhitomirsky, Electrodeposition of composite polypyrrole-carbon nanotube films, *Surface Engineering* 27(9) (2011) 655-661.

- [39] G.-L. Wang, J.-J. Xu, H.-Y. Chen, Dopamine sensitized nanoporous TiO₂ film on electrodes: photoelectrochemical sensing of NADH under visible irradiation, *Biosensors and Bioelectronics* 24(8) (2009) 2494-2498.
- [40] S. Verma, A. Ghosh, A. Das, H.N. Ghosh, Exciton-Coupled Charge-Transfer Dynamics in a Porphyrin J-Aggregate/TiO₂ Complex, *Chemistry–A European Journal* 17(12) (2011) 3458-3464.
- [41] S. Varaganti, G. Ramakrishna, Dynamics of interfacial charge transfer emission in small molecule sensitized TiO₂ nanoparticles: is it localized or delocalized , *The Journal of Physical Chemistry C* 114(32) (2010) 13917-13925.
- [42] N. Sangeetha, S. Sriman Narayanan, Hydrogen Peroxide Sensor Based on Carbon Nanotubes-Poly (celestine blue) Nanohybrid Modified Electrode, *Advanced Materials Research, Trans Tech Publ*, 2014, pp. 263-268.
- [43] X. Bingyan, Z. Mingbo, T. Hao, C. Zixia, C. Yao, W. Lei, Z. Lan, C. Yiyi, P. Huan, Iron oxide-based nanomaterials for supercapacitors, *Nanotechnology* 30(20) (2019) 204002 (31 pp.).
- [44] Q. Xia, M. Xu, H. Xia, J. Xie, Nanostructured Iron Oxide/Hydroxide-Based Electrode Materials for Supercapacitors, *ChemNanoMat* 2(7) (2016) 588-600.

5.9 Supporting informations

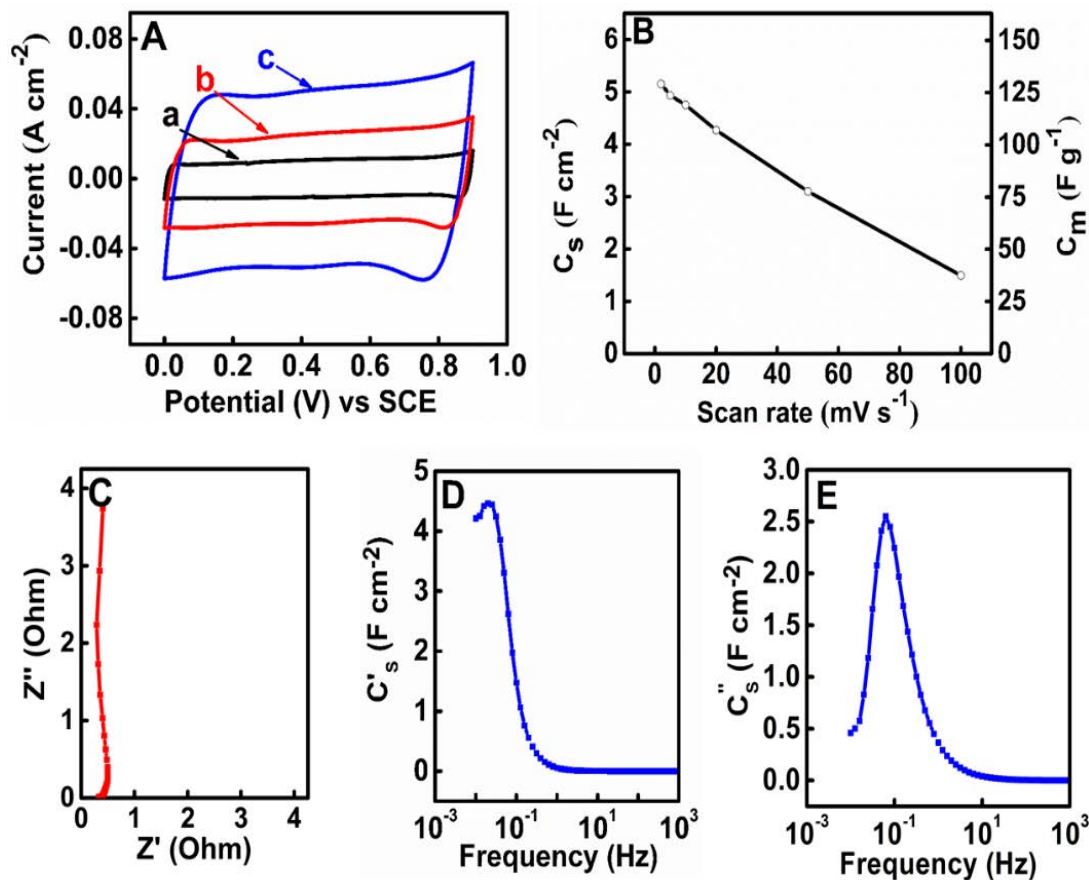


Figure 5.10 (A) CVs at scan rates of (a) 2, (b) 5 and (c) 10 mV s^{-1} , (B) C_s and C_m versus scan rate, (C) Nyquist plot of complex impedance and frequency dependences of (D) C_s' and (E) C_s'' . For a positive $\text{Mn}_3\text{O}_4\text{-CNT}$ electrode, prepared by precipitation using CB.

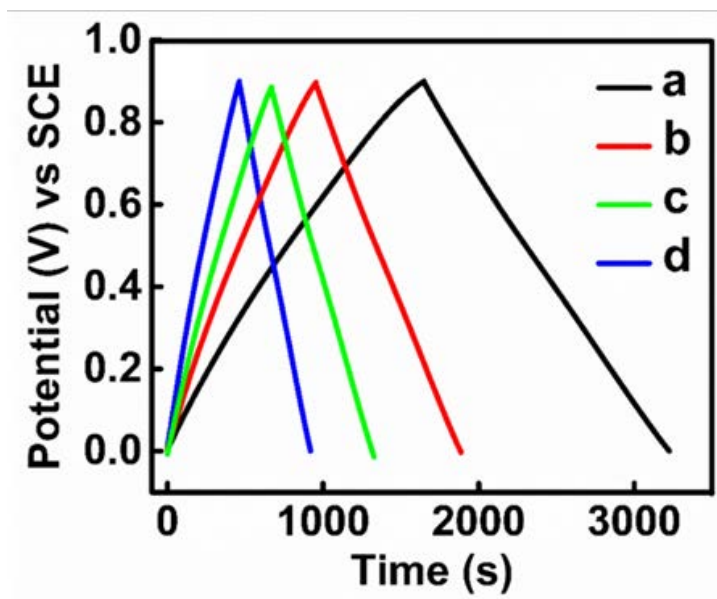


Figure 5.11 Charge-discharge curves at current densities of (a) 3, (b) 5, (c) 7, and (d) 10 mA cm^{-2} , for a positive Mn_3O_4 -CNT electrode, prepared by precipitation using CB.

Table 5.1 Fe_3O_4 -CNT samples used in this investigation.

| No. | Mass ratio (γ) Fe_3O_4 -CNT | CB | Synthesis method |
|-----|--|---------|-------------------|
| 1 | 1 | without | Physical mixing |
| 2 | 1 | without | In-situ synthesis |
| 3 | 1 | with | Physical mixing |
| 4 | 1 | with | In-situ synthesis |
| 5 | 1.25 | with | In-situ synthesis |
| 6 | 1.5 | with | In-situ synthesis |
| 7 | 2 | with | In-situ synthesis |

Chapter 6

Functionally decorated carbon nanotube networks for energy storage in supercapacitors

Mohamed Nawwar^a, , Rakesh P. Sahu^b, Ishwar K. Puri^{a,b} and Igor Zhitomirsky^{a,*},

^a Department of Materials Science and Engineering,

^b Department of Mechanical Engineering

McMaster University, Hamilton, Ontario, Canada L8S 4L7

* Corresponding Author: zhitom@mcmaster.ca. Tel.: +1 905 525-9140 ext. 23914

Submitted on 19 February 2020. Published on 24 March 2020.

Reprinted with Permission from Electrochemical Energy Conversion and Storage, a section of the journal Frontiers in Energy Research

Copyright 2020, Reproduced with Permission from Frontiers in Energy Research Journal

6.1 Abstract

A novel approach has been developed for the fabrication of Fe_3O_4 decorated multiwalled carbon nanotubes (MWCNT) for energy storage in negative electrodes of electrochemical supercapacitors. Synthesis of Fe_3O_4 was performed in the presence of MWCNT, dispersed using various cationic and anionic polyaromatic dispersants. The comparison of experimental results obtained using different dispersants provided an insight into the influence of the chemical structure of the dispersant molecules on the microstructure of the Fe_3O_4 -MWCNT materials. It was found that positively charged groups and chelating catechol ligands of the dispersants facilitated the formation of Fe_3O_4 decorated MWCNT with low agglomeration. The Fe_3O_4 -MWCNT materials, prepared using different dispersants were used for the fabrication of electrodes with mass loading of 40 mg cm^{-2} . The highest capacitance was obtained in $0.5 \text{ M Na}_2\text{SO}_4$ electrolyte for Fe_3O_4 decorated MWCNT prepared using cationic celestine blue dye as a dispersant. Improved cyclic voltammetry profile was obtained using FeOOH as an additive. Asymmetric devices were fabricated and tested based on the Fe_3O_4 decorated MWCNT negative electrodes and MnO_2 -MWCNT positive electrodes.

Keywords: carbon nanotube, iron oxide, energy, supercapacitor, dispersant

6.2 Introduction

Electrochemical supercapacitors are currently under intensive investigation for energy storage and capacitive water purification applications (Shi et al., 2014; Zhao and Zheng, 2015; Ding et al., 2020). Research is focused on the development of new materials and electrolytes (Brousse & Bélanger, 2003; Shi & Zhitomirsky, 2010; Li et al., 2019), fabrication of nanoparticles of active materials (Luo et al., 2016; Silva et al., 2018), design and modeling of composite electrodes and devices (Pavaskar et al., 2018; Xing et al., 2019). New strategies have been designed for the fabrication of carbon based electrodes with enhanced capacitive performance (Salinas Torres et al., 2019). Significant interest has been generated in application of carbon nanotubes (CNT) for the fabrication of composite electrode materials (Lu et al., 2019). The interest in CNT applications for supercapacitors is related to high electronic conductivity and high surface area of CNT.

It was recognized that CNT can be decorated with other functional materials (Pan et al., 2015; Hao et al., 2016). With a desire to fabricate new and advanced devices, there is growing interest in the development of new techniques for the fabrication of functionally decorated CNT, such as laser ablation (Imbrogno et al., 2017), atomic layer deposition (Ding et al., 2018), polymerization (Zhu et al., 2014), magnetron sputtering (Wei et al., 2014), electrodeposition (Chitturi et al., 2016), and chemical precipitation (Hong et al., 2013). Decorated CNT are of particular interest for energy storage and generation devices, such as supercapacitors, batteries and fuel cells.

The use of functionally decorated CNT allowed for the fabrication of advanced batteries with enhanced capacity (Hong et al., 2013; Wei et al., 2014), good cyclic stability (Chitturi et al., 2016) and improved conductivity (Wang et al., 2010). It has been reported that CNT can be decorated with catalysts for advanced application in fuel cells (Sonkar et al., 2017). Significant advances have been achieved in applications of functionally decorated CNT for photovoltaic devices (Mathew et al., 2011; Tai et al., 2014). It has previously been shown that carbon nanotubes can be decorated with oxides (Ojha et al., 2019), polypyrrole (Su & Zhitomirsky, 2015) and activated carbon (Shi et al., 2014) for energy storage applications in supercapacitors.

Previous studies highlighted the need in the development of efficient manufacturing techniques for the fabrication of functionally decorated CNT. Such techniques need to be based on the careful selection of dispersing agents, which must be well adsorbed on the CNT surface. Good dispersion of CNT is critical for their decoration with functional materials. The use of networks of decorated CNT is promising for the fabrication of advanced supercapacitor electrodes with high active mass.

The objective of this investigation was the fabrication of Fe_3O_4 decorated CNT for application in negative electrodes of asymmetric supercapacitors. Following this objective, we investigated anionic and cationic aromatic dispersants for the dispersion of CNT. The results presented below indicated that chemical precipitation of Fe_3O_4 in the presence of CNT allowed for the fabrication of Fe_3O_4 decorated CNT. Testing results provided an insight into the influence of electric charge and chelating groups of the dispersants on the Fe_3O_4 formation on the CNT surface. The fibrous networks of decorated CNT were used

for the fabrication of negative electrodes with high active mass of 40 mg cm^{-2} . The capacitive behavior was linked to dispersant structure. Finally, we fabricated and tested an asymmetric supercapacitor device.

6.3 Experimental procedures

Iron (II) chloride tetrahydrate ($\text{FeCl}_2 \cdot 4\text{H}_2\text{O}$), iron (III) chloride hexahydrate ($\text{FeCl}_3 \cdot 6\text{H}_2\text{O}$), ammonium hydroxide (NH_4OH), sodium hydroxide (NaOH), sodium sulfate (Na_2SO_4), Palmetic acid (PA), celestine blue (CB), pyrocatechol violet (PV), azure A chloride (AA), m-cresol purple (CP), poly(vinyl butyral-co-vinyl-alcohol-co-vinyl-acetate) (PVB, average MW = 50,000-80,000), multiwalled carbon nanotubes (MWCNT, purity > 95 %, OD 20-30 nm, and length 1–2 μm , US Nanomaterial Inc, USA), and Ni foam (porosity of 95%, Vale Ltd., Canada) were used.

For decoration of the MWCNT by Fe_3O_4 nanoparticles, the synthesis of the nanoparticles was performed in the presence of dispersed MWCNT. In this procedure, 1 g L^{-1} of MWCNT were dispersed in DI water by ultrasonication for 15 min and then 0.25 g L^{-1} dispersant was added and suspension was ultrasonicated again for 15 min. A stoichiometric mixture of Fe^{2+} and Fe^{3+} salts dissolved in DI water was added to the suspension of MWCNT in order to obtain the mass ratio of Fe_3O_4 to MWCNT equal to 1.5. The pH was adjusted to 9 by the addition of 1 M NH_4OH . The obtained suspension was ultrasonicated for 40 min and then filtrated. The materials were washed with DI water and dried overnight. The magnetite decorated MWCNT, prepared using CB, PV, AA and CP were denoted as M-CB-MWCNT, M-PV-MWCNT, M-AA-MWCNT and M-CP-MWCNT, respectively. Non-agglomerated FeOOH nanoparticles were

prepared by a chemical precipitation and liquid-liquid extraction method (Chen et al., 2019). However, in contrast to the previous investigation (Chen et al., 2019) PA was used as a new and efficient extractor. M-FH-CB-MWCNT material was prepared by mixing of M-CB-MWCNT (80%) and FeOOH (20%).

M-CB-MWCNT, M-PV-MWCNT, M-AA-MWCNT, M-CP-MWCNT and M-FH-CB-MWCNT were dispersed in ethanol, containing dissolved PVB binder and obtained slurries were used for the impregnation of Ni foam current collectors and fabrication of negative electrodes of supercapacitors. The PVB binder content in the electrodes was 3%. The total mass of the impregnated material was 40 mg cm^{-2} . MnO₂-MWCNT material for positive electrodes was prepared by the precipitation and liquid-liquid extraction method (Chen, et al., 2017). The asymmetric device was fabricated containing M-FH-CB-MWCNT negative electrodes with mass loading of 40 mg cm^{-2} and MnO₂-MWCNT positive electrodes with mass loading of 35 mg cm^{-2} . At such mass loadings the capacitance of negative electrodes matched the capacitance of the positive electrodes.

Transmission electron microscopy was performed (dark field STEM) using a JEOL 2010F field emission microscope. X-ray diffraction (XRD) analysis was performed using the Bruker D8 Discover instrument comprising Davinci diffractometer and Co-K α radiation. Particle size distribution was done using dynamic light scattering (DLS) model (DelsaMax Pro- Beckman Coulter). The analysis was carried out based on testing of 4 sets of each material with a concentration of 0.4 mg L^{-1} in DI, where every set consisted of 10 acquisition.

Cyclic voltammetry and electrochemical impedance spectroscopy studies of single electrodes and asymmetric device were performed in 0.5 M Na₂SO₄ electrolyte as described in prior investigations (Shi & Zhitomirsky, 2013; Zhu et al., 2014; Chen et al., 2017). EIS measurements were carried out in the frequency range of 10 mHz–100 kHz with a sinusoidal signal of 10mV. The components of complex capacitance (C_s' and C_s'') were calculated from the EIS data as $C_s' = Z'' / \omega |Z|^2 A$ and $C_s'' = Z' / \omega |Z|^2 A$, where $\omega = 2\pi f$ and f is frequency. Galvanostatic charge–discharge of individual electrodes at different current densities and discussion performed using Biologic VMP300 potentiostat. The charge-discharge behavior of the asymmetric device was analyzed using battery analyzers BST8-MA and BST8-3 (MTI Corporation, USA).

6.4 Results and discussion

Figure 6.1 (A) shows chemical structures of aromatic dispersants used for dispersion of MWCNT. The polyaromatic structure of the dispersants was beneficial (Ata et al., 2018) for their adsorption on MWCNT. The adsorption mechanism involved π - π interactions. The adsorbed dispersants imparted a positive charge (CB, AA) or a negative charge (PV, CP) to MWCNT. The small size, electric charge and good adsorption of the dispersants on MWCNT facilitated MWCNT dispersion by unzipping mechanism (Ata et al., 2018; Figure 6.1 (E)) and allowed for the fabrication of stable suspensions. Figure 6.1 (F, G) illustrates different types of interactions of the dispersants with Fe₃O₄ particles. The precipitation of Fe₃O₄ was achieved at pH=9, which is above the isoelectric point (pH=6.5) (Parks, 1965) of this material.

Therefore, the Fe_3O_4 particles were negatively charged. The negative charge of Fe_3O_4 resulted in electrostatic repulsion of Fe_3O_4 and anionic PV or CP, adsorbed on MWCNT Figure 6.1 (F). In contrast, electrostatic attraction existed between Fe_3O_4 and cationic CB or AA molecules, adsorbed on MWCNT Figure 6.1 (G). Previous investigations (Ata et al., 2014) showed that molecules, containing a catechol group, strongly adsorbed on inorganic particles and facilitated their efficient dispersion. Therefore, CB and PV can be adsorbed on Fe_3O_4 particles by catecholate type bonding. Figure 6.1 (F) shows bonding of PV to the Fe atom on the particle surface. A similar mechanism can be suggested for CB bonding. It is important to note that phenolic molecules containing single OH groups, such as CP, show poor adsorption on inorganic molecules (Ata et al., 2014). In contrast, molecules from the catechol family, such as PV, containing two adjacent OH groups, show very strong bonding to the inorganic particles (Ata et al., 2014).

X-ray diffraction studies confirmed the formation of pure Fe_3O_4 by precipitation from mixed Fe^{2+} and Fe^{3+} salt solutions (supplementary information, Figure 6.10). The materials prepared by precipitation from the same solutions, containing dispersed MWCNT, showed X-ray diffraction peaks of Fe_3O_4 and MWCNT (Figure 6.2). Peak broadening resulted from the small particle size of Fe_3O_4 .

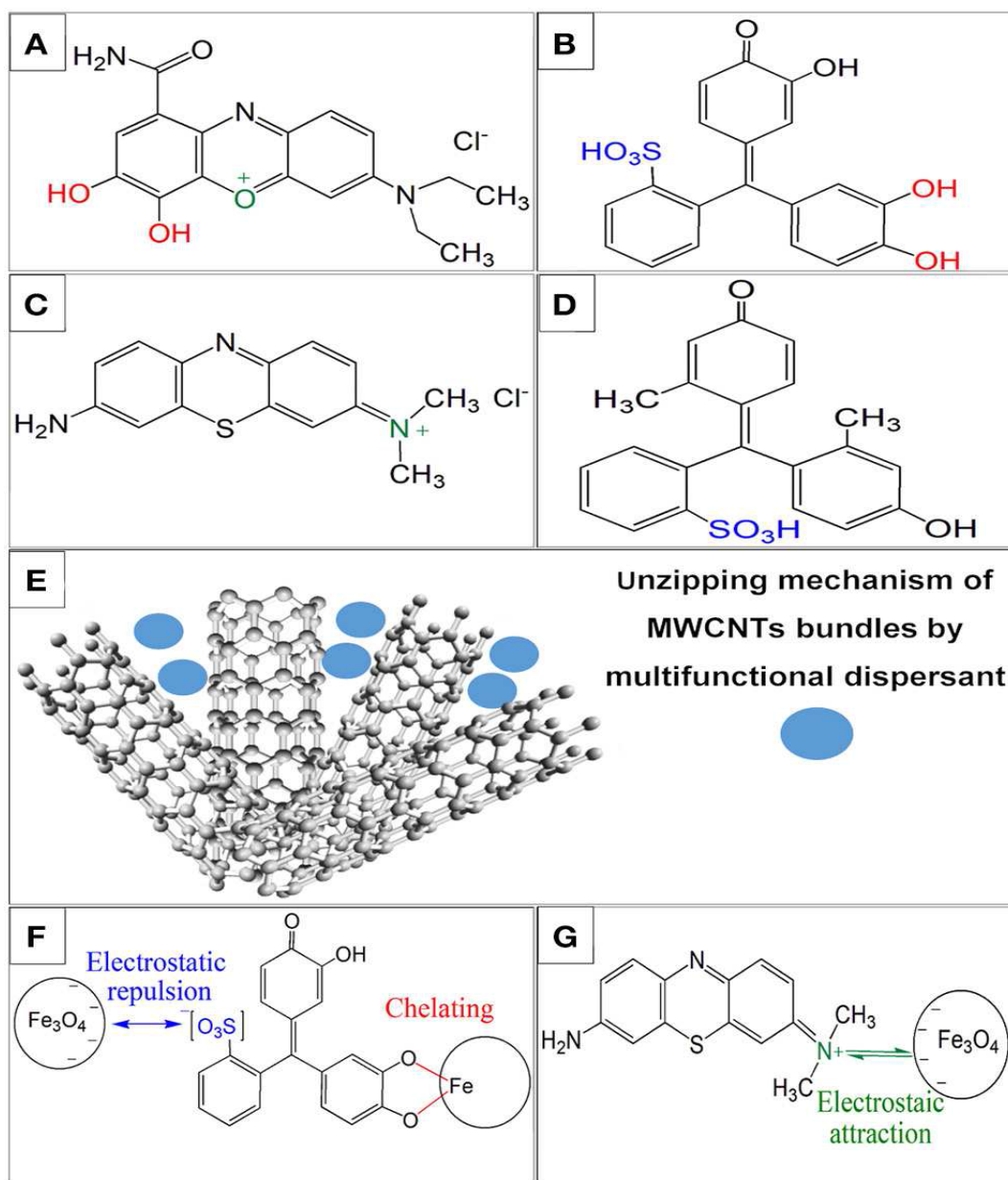


Figure 6.1 Chemical structures of (A) CB, (B) PV, (C) AA, (D) CP and schematics, showing (E) unzipping of MWCNT bundles by dispersants, (F) electrostatic repulsion of PV and Fe_3O_4 particles and chelating bonding of PV to Fe atoms on the Fe_3O_4 particle surface, involving a catechol group of PV, (G) electrostatic attraction of AA and Fe_3O_4 .

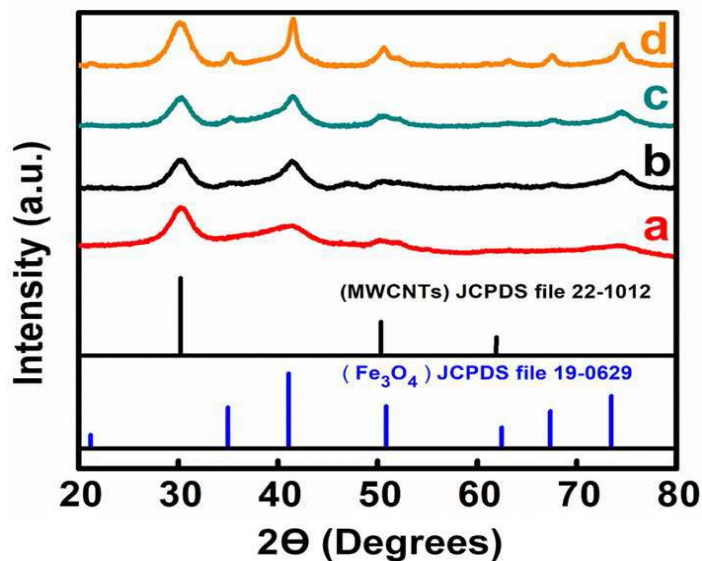


Figure 6.2 X-ray diffraction patterns of (a) M-CB-MWCNT, (b) M-PV-MWCNT, (c) M-AA-MWCNT, and (d) M-CP-MWCNT.

Figure 6.3 shows TEM images of the materials at different magnifications. The TEM images of M-CBMWCNT showed the formation of Fe₃O₄ decorated MWCNT. The size of the Fe₃O₄ particles adsorbed on the MWCNT was about 10 nm. It is suggested that electrostatic attraction of positively charged CB dispersant and negatively charged Fe₃O₄ as well as chelating bonding of the catechol group facilitated the formation of the decorated MWCNT. It is important to note that electrostatic repulsion of the PV dispersant, adsorbed on the MWCNT surface, and Fe₃O₄ nanoparticles was detrimental for the formation of the decorated MWCNT. On the other hand, the chelating bonding of the catechol groups of PV promoted Fe₃O₄ formation on the MWCNT surface. The chelating bonding was a dominating mechanism, which allowed for the formation of decorated MWCNT. However, the TEM studies of M-PV-MWCNT also revealed the formation of small agglomerates of the Fe₃O₄ particles as it is shown in Figure 6.3 (F).

The analysis of the TEM images for M-AA-MWCNT and M-CP-MWCNT showed enhanced agglomeration of the Fe_3O_4 particles. The agglomeration is especially evident for M-CP-MWCNT samples. In this case, the poor coverage of MWCNT resulted from electrostatic repulsion of CP and Fe_3O_4 .

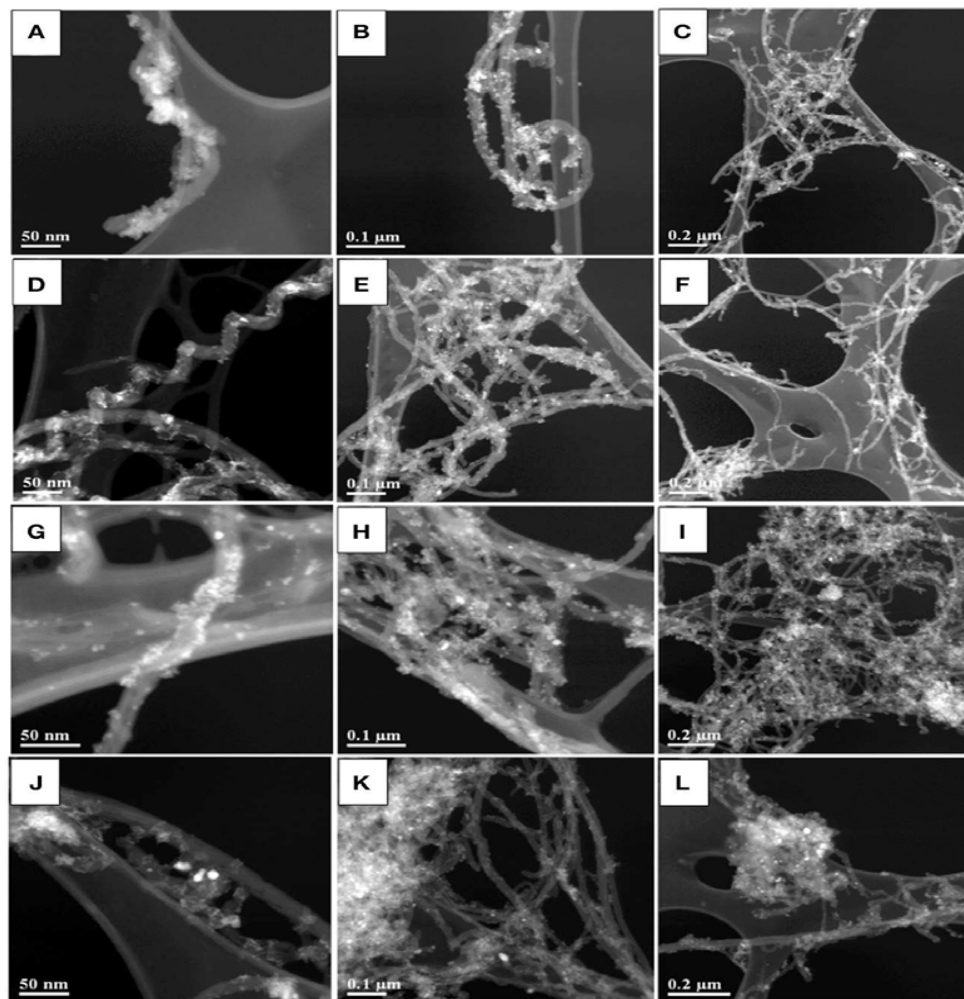


Figure 6.3 TEM images at different magnifications for (A–C) M-CB-MWCNT, (D–F) M-PV-MWCNT, (G–I) M-AA-MWCNT, and (J–L) M-CP-MWCNT.

The effect of different dispersing agents has also been studied using DLS analysis (Figure 6.4). The size distribution of the aggregates in all samples is bimodal with different degree of polydispersity. The effect of different dispersing agents has also been

studied using DLS analysis (Figure 6.4). The size distribution of the aggregates in all samples is bimodal with different degree of polydispersity. The first peak at ~ 100 nm is present in all four dispersions with different intensities. The second peak was observed in the range of 10^3 - 10^4 nm. The intensity and polydispersity of the second peak are smallest for M-CB-MWCNT. The polydispersity of M-PV-MWCNT is broader than that of M-CB-MWCNT. The analysis of the DLS data for M-AA-MWCNT and M-CP-MWCNT revealed significant increase in the relative intensity of the second peak, compared to the intensity of the first peak. The second peak for M-AA-MWCNT and M-CP-MWCNT shifted to larger radius numbers, compared to the second peak for M-CB-MWCNT. The increase in relative intensity of the second peak for M-AA-MWCNT and M-CP-MWCNT and peak shifts indicated an increasing number of agglomerates and increase in the agglomerate size of the particles.

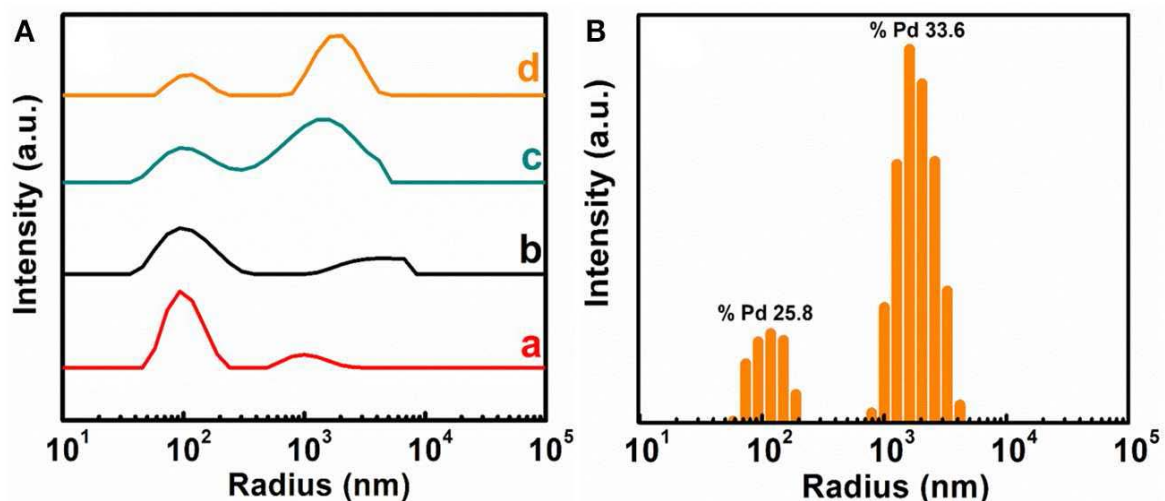


Figure 6.4 (A) Average data (40 samples of each composition) for DLS analysis of (a) M-CB-MWCNT, (b) M-PV-MWCNT, (c) M-AA-MWCNT and (d) M-CP-MWCNT, (B) Typical spectrum for M-CP-MWCNT. The width of the peaks indicates the polydispersity of the aggregate (Pd).

This is in agreement with the TEM data and indicates the beneficial effect of the catechol groups of CB and PV for the formation of decorated CNT and reduction of Fe₃O₄ agglomeration. It is important to note that the decoration of MWCNT resulted from the dispersant mediated adsorption. In this approach the changes in MWCNT structure, resulting from chemical reactions and high temperature treatment (Xing et al. 2015, 2017, 2019) can be avoided.

M-CB-MWCNT, M-PV-MWCNT, M-AA-MWCNT, M-CP-MWCNT were used for the fabrication of supercapacitor electrodes with mass loading of 40 mg cm⁻². Figure 6.5 shows cyclic voltammetry data for the electrodes in the potential range of -0.9 - 0.0 V vs. SCE. M-CB-MWCNT electrodes showed a larger CV area, compared to other electrodes and higher integral capacitance in the selected potential window. The M-CP-MWCNT electrodes showed lower capacitance, compared to other materials. The higher capacitance of M-CB-MWCNT can result from reduced agglomeration of the Fe₃O₄ particles and improved contact of Fe₃O₄ and MWCNT. However, the CV for M-CB-MWCNT showed redox peaks and deviated significantly from the box shape. Significant reduction of the charge and discharge currents was observed in the potential range of -0.4 to -0.7V. The observed redox peak can result from the redox-active properties of CB (Noorbakhsh et al., 2008). Such CV shape is detrimental for the fabrication of asymmetric cells. In order to improve the CV profile, M-CB-MWCNT was combined with FeOOH, which shows good charge storage properties in the range of -0.4 to -0.7 V (Chen et al., 2018). Therefore, M-FH-CB-MWCNT was prepared and tested. This material showed improved CV shape, compared to M-CB-MWCNT. The capacitance of 5.76 F cm⁻² (144 F g⁻¹) was obtained at a scan rate of 2 mV s⁻¹.

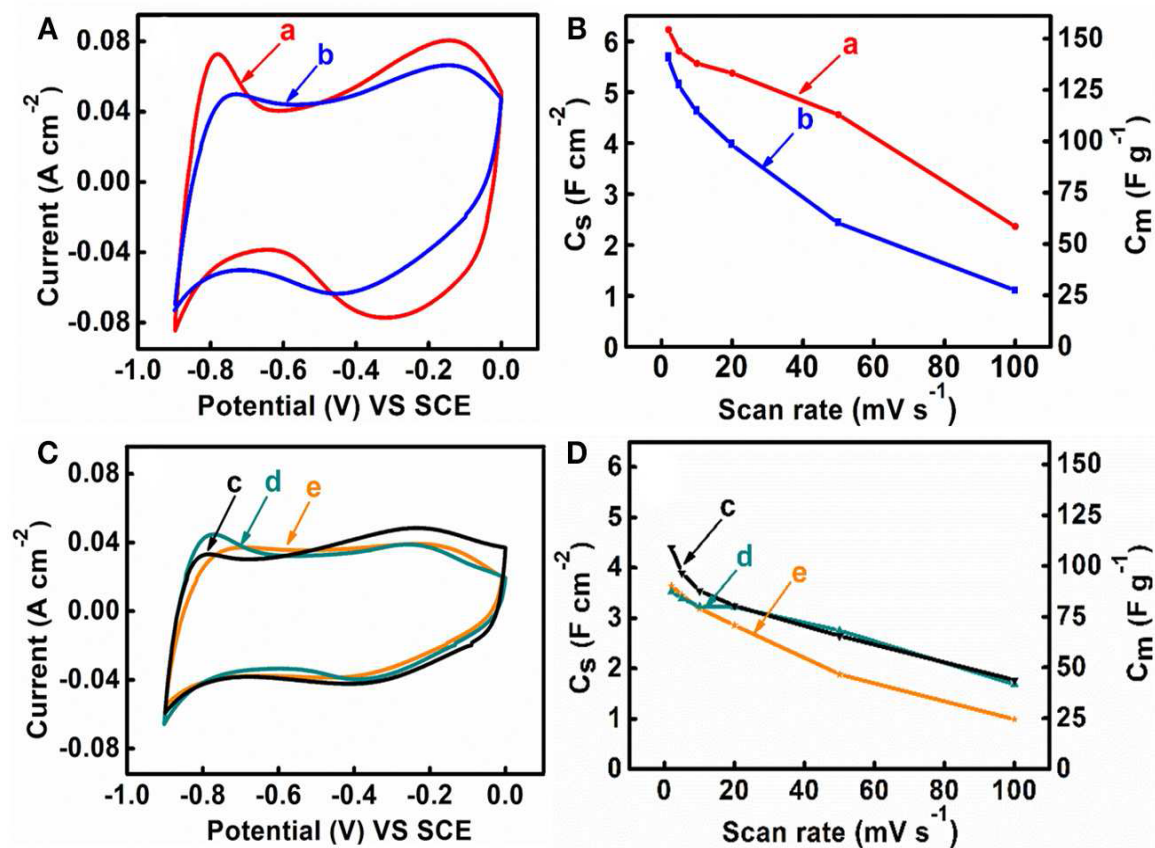


Figure 6.5 (A,C) CVs and (B,D) capacitance vs. scan rate for (a) M-CB-MWCNT, (b) M-FH-CB-MWCNT, (c) M-PV-MWCNT, (d) M-AA-MWCNT and (e) M-CP-MWCNT electrodes.

Figure 6.6 shows frequency dependences of the components of differential AC capacitance, calculated from the impedance data. M-CB-MWCNT showed the highest real part of capacitance C_s' at low frequencies, compared to other materials. However, the M-FH-CB-MWCNT electrodes showed lower C_s'' , which indicated lower energy losses. The slightly higher relaxation frequency, corresponding to maximum of C_s'' , indicated better performance. The M-CP-MWCNT electrodes, showed lower C_s' and lower relaxation frequency, compared to other materials. The capacitive behavior of the electrodes has also been analyzed by chronopotentiometry.

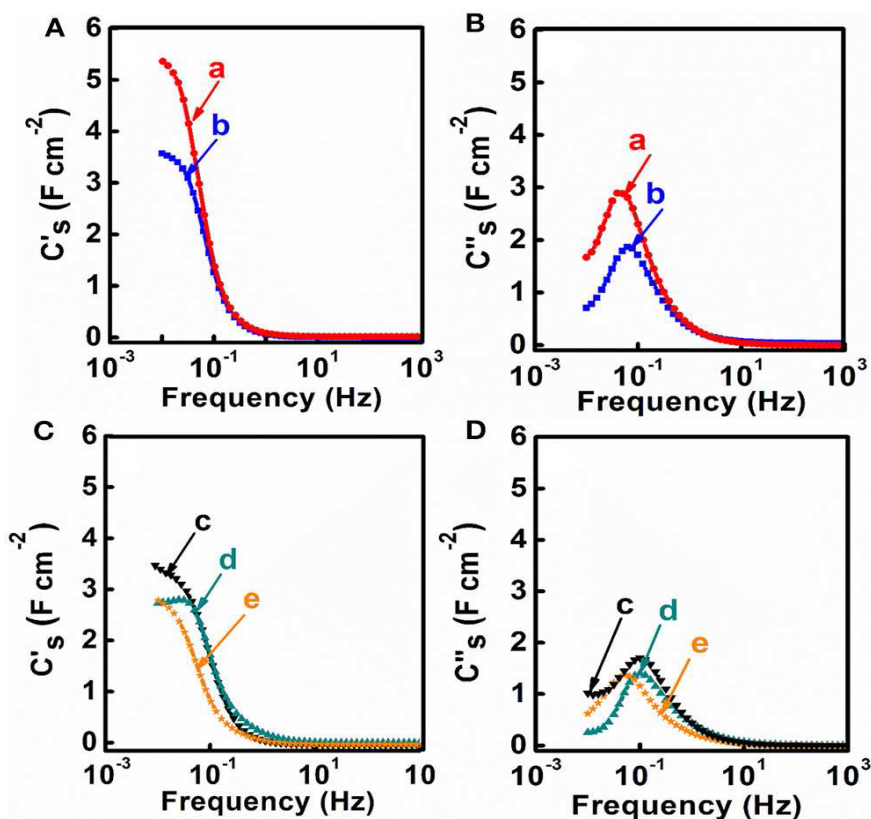


Figure 6.6 (A–D) Frequency dependences of components of complex AC capacitance, calculated from impedance data for (a) M-CB-MWCNT, (b) M-FH-CB-MWCNT, (c) M-PV-MWCNT, (d) M-AA-MWCNT and (e) M-CP-MWCNT electrodes.

Figure 6.7 compares galvanostatic charge-discharge curves for different electrodes and capacitances, calculated from the discharge data at different current densities. The charge-discharge curves were of nearly triangular shape. The highest capacitance at 3 mA cm^{-2} was achieved using M-CP-MWCNT. However, M-FH-CB-MWCNT showed benefits of nearly constant capacitance in the range of $3\text{-}10 \text{ mA cm}^{-2}$. The M-CP-MWCNT and M-FH-CB-MWCNT electrodes showed practically the same capacitances at 5 and 10 mA cm^{-2} . The M-CP-MWCNT electrodes showed significantly lower capacitance, compared to other electrodes in agreement with CV and impedance spectroscopy data.

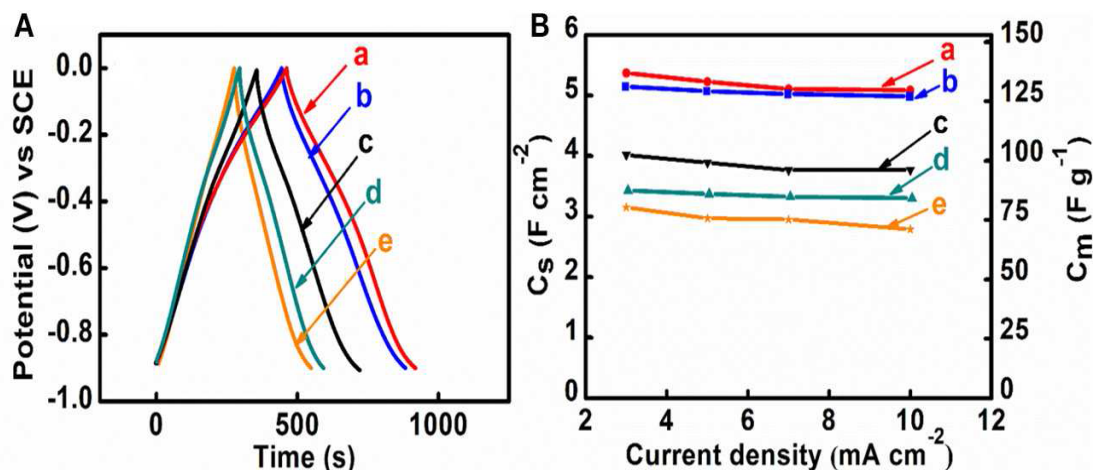


Figure 6.7 (A) Charge-discharge curves at current density of 5 mA cm^{-2} , (B) capacitance, calculated from charge-discharge data, vs. current density for (a) M-CB-MWCNT, (b) M-FH-CB-MWCNT, (c) M-PV-MWCNT, (d) M-AA-MWCNT and (e) M-CP-MWCNT.

M-FH-CB-MWCNT electrodes were used for the fabrication of the asymmetric supercapacitor cells. One of the problems related to the fabrication of asymmetric devices with Na_2SO_4 electrolyte is related to lower capacitance of negative electrodes, compared to the capacitance of advanced positive electrodes, such as MnO_2 -MWCNT (Ri Chen et al., 2017). However, M-FH-CB-MWCNT electrodes showed relatively high capacitance and the asymmetric device was fabricated using 40 mg cm^{-2} M-FH-CB-MWCNT negative electrode and 35 mg cm^{-2} MnO_2 -MWCNT positive electrode. Figure 6.8 (A) shows CVs for the device in a voltage window of 1.6 V. The current increased with increasing scan rate. As expected, the capacitance C_s of the device was about 50% of the capacitance of the individual electrodes Figure 6.8 (B). The device showed relatively low impedance and relatively high relaxation frequency Figure 6.8 (C-E).

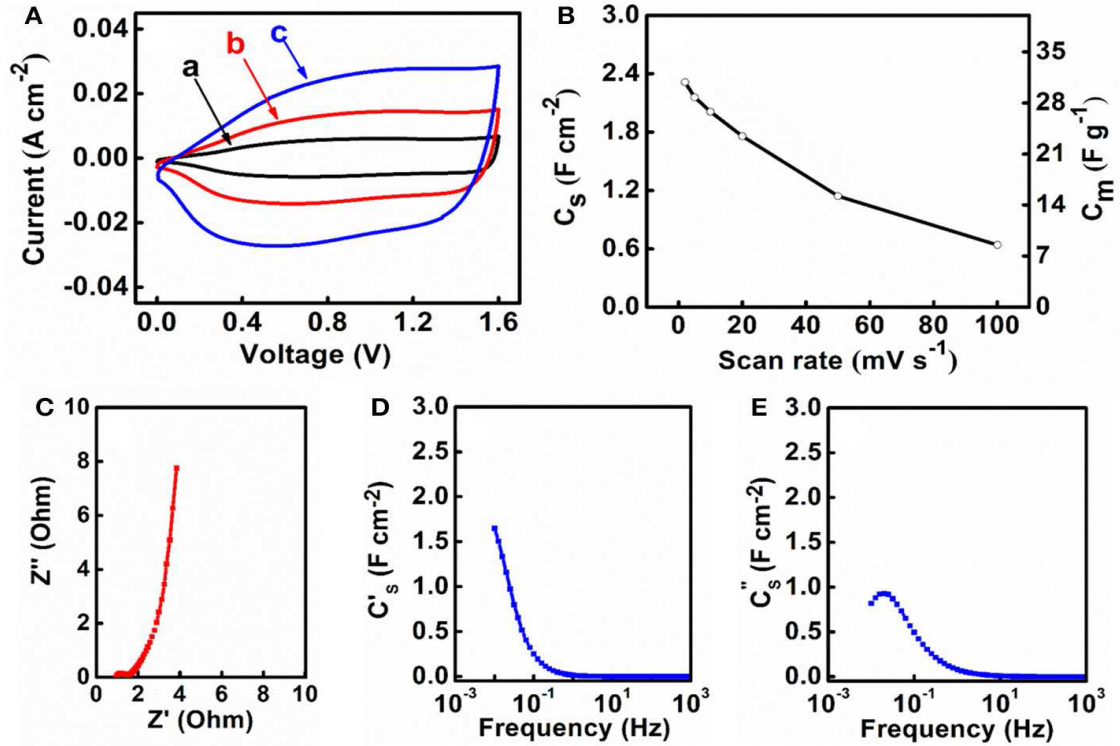


Figure 6.8 (A) CVs at scan rates of (a) 2, (b) 5 and (c) 10 mV s⁻¹, (B) C_s and C_m calculated from the CV data versus scan rate, (C) Nyquist plot of complex impedance and frequency dependences of (D) C_s' and (E) C_s'' for an asymmetric supercapacitor cell, containing M-FH-CB-MWCNT as a negative electrode and MnO₂-MWCNT as a positive electrode.

The asymmetric devices showed ideal triangular shape charge-discharge curves Figure 6.9 (A, inset). The capacitance slightly decreased Figure 6.9 (A) with current density in the range of 3-50 mA cm⁻². The capacitance retention after 1000 cycles was 75% Figure 6.9 (B). The Coulombic efficiency remained about 100% during cycling. The device had an energy density of about 1 mWh cm⁻² which showed relatively small variations with increasing current density in the range of 3-50 mA cm⁻² Figure 6.9 (C). Two cells, connected in series, allowed for the powering of eleven 20 mA LEDs, as it is shown in Figure 6.9 (D).

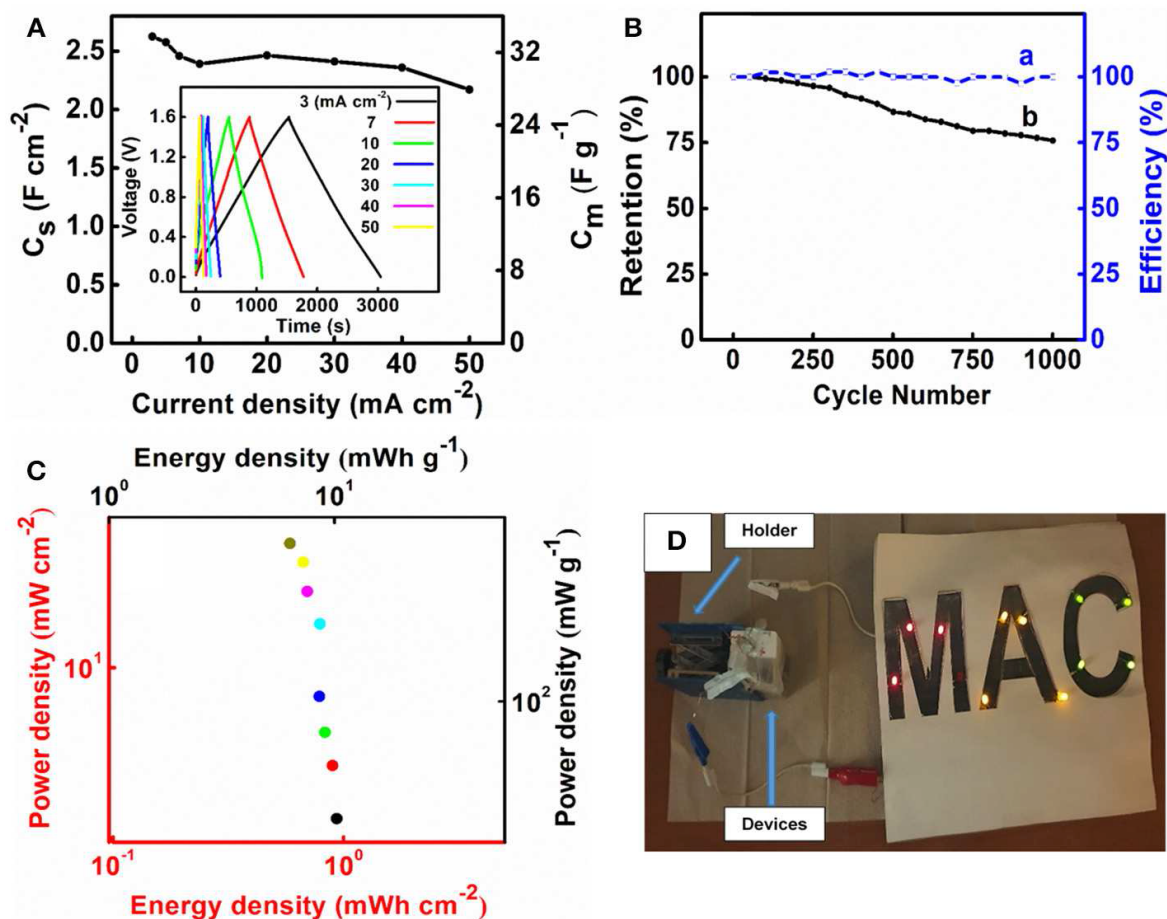


Figure 6.9 (A) C_s and C_m vs. current density calculated from discharge data, inset shows charge-discharge curves, and different current densities, (B) (a) Coulombic efficiency and (b) capacitance retention and vs. cycle number, (C) Ragone plot for an asymmetric supercapacitor cell, containing M-FH-CB-MWCNT as a negative electrode and MnO_2 -MWCNT as a positive electrode, (D) LEDs powered by two asymmetric cells.

6.5 Conclusions

Polyaromatic CB, PV, AA and CP molecules allowed for efficient dispersion of MWCNT. The chelating catechol groups of CB and PV as well as electrostatic attraction of cationic CB and AA with negatively charged Fe_3O_4 particles were beneficial for the formation of Fe_3O_4 decorated MWCNT. M-CB-MWCNT showed a network of Fe_3O_4 decorated

MWCNT and low agglomeration of Fe₃O₄ nanoparticles. M-CB-MWCNT exhibited higher capacitance, compared to M-PV-MWCNT, M-AA-MWCNT and M-CP-MWCNT. Compared to M-CB-MWCNT, the M-FH-CB-MWCNT electrodes showed improved CV profile, reduced AC energy losses and low variation of capacitance with increasing charge-discharge current. M-FH-CB-MWCNT showed good capacitive behavior at mass loading of 40 mg cm⁻². Asymmetric devices were fabricated, containing M-FH-CB-MWCNT negative electrodes and MnO₂-MWCNT positive electrodes, which showed promising capacitance and power-energy characteristics.

6.6 Author contributions

MN conducted synthesis of materials, performed materials characterization and electrochemical testing and contributed to the writing of the manuscript. RS contributed to DLS and electron microscopy testing, data analysis and writing of the manuscript. IZ contributed to the development of new dispersants, cell design, and IP and IZ contributed to the data analysis and writing of the manuscript.

6.7 Funding

This work was supported by the Natural Sciences and Engineering Research Council of Canada

6.8 Acknowledgment

The authors would like to thank the Natural Sciences and Engineering Research Council of Canada for the financial support. Dr. Carmen Andrei of Canadian Centre for Electron Microscopy (CCEM), M.A.Sc. Victoria Jarvis of McMaster Analytical X-Ray Diffraction

Facility for XRD for assistance with measurements, and Dr. R. Poon for fruitful discussions and technical support.

6.9 Data availability statement

The datasets generated for this study are available on request to the corresponding author

6.10 Conflict of interest

The authors declare that the research was conducted in the absence of any commercial or financial relationships that could be construed as a potential conflict of interest.

6.11 Supplementary material

The supplementary material for this article can be found online at <https://www.frontiersin.org/articles/10.3389/fenrg.2020.0004/full/supplementarymaterial>

6.12 References

- [1] Ata, M., Liu, Y., & Zhitomirsky, I. (2014). A review of new methods of surface chemical modification, dispersion and electrophoretic deposition of metal oxide particles. *RSC Advances*, 4(43), 22716-22732.
- [2] Ata, M. S., Poon, R., Syed, A. M., Milne, J., & Zhitomirsky, I. (2018). New developments in non-covalent surface modification, dispersion and electrophoretic deposition of carbon nanotubes. *Carbon*, 130, 584-598.
- [3] Brousse, T., & Bélanger, D. (2003). A hybrid $\text{Fe}_3\text{O}_4\text{-MnO}_2$ capacitor in mild aqueous electrolyte. *Electrochemical and solid-state letters*, 6(11), A244-A248.
- [4] Chen, R., Poon, R., Sahu, R. P., Puri, I. K., & Zhitomirsky, I. (2017). MnO_2 -carbon nanotube electrodes for supercapacitors with high active mass loadings. *Journal of the Electrochemical Society*, 164(7), A1673-A1678.
- [5] Chen, R., Puri, I., & Zhitomirsky, I. (2019). Polypyrrole-carbon nanotube- FeOOH composites for negative electrodes of asymmetric supercapacitors. *Journal of the Electrochemical Society*, 166(6), A935-A940.
- [6] Chen, R., Puri, I. K., & Zhitomirsky, I. (2018). High areal capacitance of FeOOH -carbon nanotube negative electrodes for asymmetric supercapacitors. *Ceramics International*, 44(15), 18007-18015.
- [7] Chitturi, V. R., Ara, M., Fawaz, W., Ng, K. Y. S., & Arava, L. M. R. (2016). Enhanced lithium-oxygen battery performances with Pt subnanocluster decorated n-doped single-walled carbon nanotube cathodes. *ACS Catalysis*, 6(10), 7088-7097.
- [8] Ding, H., Zhang, Q., Liu, Z., Wang, J., Ma, R., Fan, L., Lu, B. (2018). TiO_2 quantum dots decorated multi-walled carbon nanotubes as the multifunctional separator for highly stable lithium sulfur batteries. *Electrochimica Acta*, 284, 314-320.
- [9] Ding, Y., Wang, T., Dong, D., & Zhang, Y. (2020). Using biochar and coal as the electrode material for supercapacitor applications. *Frontiers in Energy Research*, 7, 159.

- [10] Hao, M., Tang, M., Wang, W., Tian, M., Zhang, L., & Lu, Y. (2016). Silver-nanoparticle-decorated multiwalled carbon nanotubes prepared by poly (dopamine) functionalization and ultraviolet irradiation. *Composites Part B: Engineering*, 95, 395-403.
- [11] Hong, H. P., Kim, M. S., Lee, Y. H., Yu, J. S., Lee, C. J., & Min, N. K. (2013). Spray deposition of LiMn_2O_4 nanoparticle-decorated multiwalled carbon nanotube films as cathode material for lithium-ion batteries. *Thin Solid Films*, 547, 68-71.
- [12] Imbrogno, A., Pandiyan, R., Barberio, M., Macario, A., Bonanno, A., & El khakani, M. A. (2017). Pulsed-laser-ablation based nanodecoration of multi-wall-carbon nanotubes by co-ni nanoparticles for dye-sensitized solar cell counter electrode applications. *Materials For Renewable and Sustainable Energy*, 6(2), 11 (10 pp.).
- [13] Li, X., Huang, Z., & Zhi, C. (2019). Environmental stability of mxenes as energy storage materials. *Front. Mater.*, 6, 312.
- [14] Lu, Z., Raad, R., Safaei, F., Xi, J., Liu, Z., & Foroughi, J. (2019). Carbon nanotube based fiber supercapacitor as wearable energy storage. *Frontiers in Materials*, 6, 138.
- [15] Luo, D., Wallar, C. J., Shi, K., and Zhitomirsky, I. (2016). Enhanced capacitive performance of mno_2 -multiwalled carbon nanotube electrodes, prepared using lauryl Gallate dispersant. *Colloids Surfaces A* 509, 504–511. doi: 10.1016/j.colsurfa.2016.09.065
- [16] Mathew, A., Rao, G. M., & Munichandraiah, N. (2011). Dye sensitized solar cell based on platinum decorated multiwall carbon nanotubes as catalytic layer on the counter electrode. *Materials Research Bulletin*, 46(11), 2045-2049.
- [17] Noorbakhsh, A., Salimi, A., & Sharifi, E. (2008). Fabrication of glucose biosensor based on encapsulation of glucose - oxidase on sol - gel composite at the surface of glassy carbon electrode modified with carbon nanotubes and celestine blue. *Electroanalysis: An International Journal Devoted to Fundamental and Practical Aspects of Electroanalysis*, 20(16), 1788-1797.

- [18] Ojha, M., Le Houx, J., Mukkabila, R., Kramer, D., Andrew Wills, R. G., & Deepa, M. (2019). Lithium titanate/pyrenecarboxylic acid decorated carbon nanotubes hybrid - alginate gel supercapacitor. *Electrochimica Acta*, 309, 253-263.
- [19] Pan, Y., Hu, W., Liu, D., Liu, Y., & Liu, C. (2015). Carbon nanotubes decorated with nickel phosphide nanoparticles as efficient nanohybrid electrocatalysts for the hydrogen evolution reaction. *Journal of Materials Chemistry A*, 3(24), 13087-13094.
- [20] Parks, G. A. (1965). The isoelectric points of solid oxides, solid hydroxides, and aqueous hydroxo complex systems. *Chemical Reviews*, 65(2), 177-198.
- [21] Pavaskar, G., Ramakrishnasubramanian, K., Kandagal, V. S., & Kumar, P. (2018). Modeling electric double-layer capacitors using charge variation methodology in gibbs ensemble. *Frontiers in Energy Research*, 5, 36.
- [22] Salinas Torres, D., Ruiz-Rosas, R., Morallon, E., & Cazorla-Amorós, D. (2019). Strategies to enhance the performance of electrochemical capacitors based on carbon materials. *Frontiers in Materials*, 6, 115.
- [23] Shi, C., & Zhitomirsky, I. (2010). Electrodeposition and capacitive behavior of films for electrodes of electrochemical supercapacitors. *Nanoscale Research Letters*, 5(3), 518.
- [24] Shi, K., Ren, M., & Zhitomirsky, I. (2014). Activated carbon-coated carbon nanotubes for energy storage in supercapacitors and capacitive water purification. *ACS Sustainable Chemistry & Engineering*, 2(5), 1289-1298.
- [25] Shi, K., & Zhitomirsky, I. (2013). Electrophoretic nanotechnology of graphene-carbon nanotube and graphene-polypyrrole nanofiber composites for electrochemical supercapacitors. *Journal of Colloid and Interface Science*, 407, 474-481.
- [26] Silva, R. M. E., Poon, R., Milne, J., Syed, A., & Zhitomirsky, I. (2018). New developments in liquid-liquid extraction, surface modification and agglomerate-free processing of inorganic particles. *Advances in Colloid and Interface Science*, 261, 15-27.

- [27] Sonkar, P. K., Prakash, K., Yadav, M., Ganesan, V., Sankar, M., Gupta, R., & Yadav, D. K. (2017). Co(ii)-porphyrin-decorated carbon nanotubes as catalysts for oxygen reduction reactions: An approach for fuel cell improvement. *Journal of Materials Chemistry A*, 5(13), 6263-6276.
- [28] Su, Y., & Zhitomirsky, I. (2015). Asymmetric electrochemical supercapacitor, based on polypyrrole coated carbon nanotube electrodes. *Applied Energy*, 153, 48-55.
- [29] Tai, S.-Y., Lu, M.-N., Ho, H.-P., Xiao, Y., & Lin, J.-Y. (2014). Investigation of carbon nanotubes decorated with cobalt sulfides of different phases as nanocomposite catalysts in dye-sensitized solar cells. *Electrochimica Acta*, 143, 216-221.
- [30] Wang, T., Kaempgen, M., Nopphawan, P., Wee, G., Mhaisalkar, S., & Srinivasan, M. (2010). Silver nanoparticle-decorated carbon nanotubes as bifunctional gas-diffusion electrodes for zinc-air batteries. *Journal of Power Sources*, 195(13), 4350-4355.
- [31] Wei, W., Ruiz, I., Ahmed, K., Bay, H. H., George, A. S., Wang, J., Ozkan, C. S. (2014). Silicon decorated cone shaped carbon nanotube clusters for lithium ion battery anodes. *Small*, 10(16), 3389-3396.
- [32] Xing, Z., Deng, Y.-P., Sy, S., Tan, G., Li, A., Li, J., et al. (2019). Carbon-pore-sheathed cobalt nanoseeds: an exceptional and durable bifunctional catalyst for zinc-air batteries. *Nano Energy* 65, 104051. doi: 10.1016/j.nanoen.2019. 104051
- [33] Xing, Z., Qi, Y., Tian, Z., Xu, J., Yuan, Y., Bommier, C., et al. (2017). Identify the removable substructure in carbon activation. *Chem. Mater.* 29, 7288–7295. doi: 10.1021/acs.chemmater.7b01937
- [34] Xing, Z., Wang, B., Halsted, J. K., Subashchandrabose, R., Stickle, W. F., and Ji, X. (2015). Direct fabrication of nanoporous graphene from graphene oxide by adding a gasification agent to a magnesiothermic reaction. *Chem. Commun.* 51, 1969–1971. doi: 10.1039/C4CC08977D.

[35] Zhao, C., & Zheng, W. (2015). A review for aqueous electrochemical supercapacitors. *Frontiers in Energy Research*, 3, 23.

[36] Zhu, Y., Shi, K., & Zhitomirsky, I. (2014). Polypyrrole coated carbon nanotubes for supercapacitor devices with enhanced electrochemical performance. *Journal of Power Sources*, 268, 233-239. doi.org/10.1016/j.jpowsour.2014.06.046.

6.13 Supporting informations

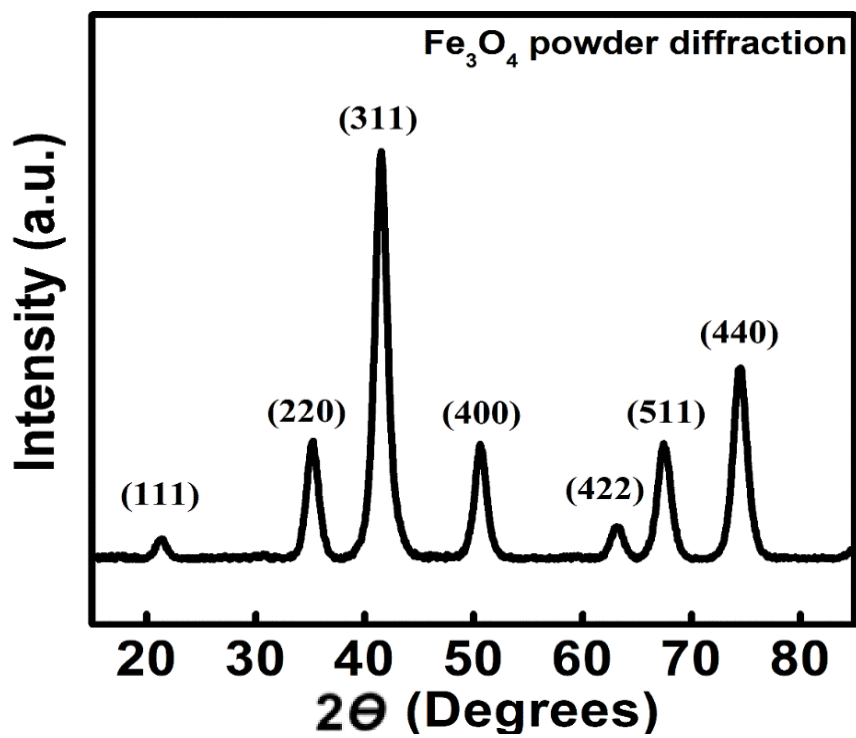


Figure 6.10 X-ray diffraction patterns of Fe₃O₄ powder (JCPDS file 19-0629).

Table 6.1 Detailed results for CVs, the average C_s , C_m versus scan rates capacitance vs. scan rate for (a) M-CB-MWCNT, (b) M-FH-CB-MWCNT, (c) M-PV-MWCNT, (d) M-AA-MWCNT and (e) M-CP-MWCNT electrodes.

| Gamma | Composite | Scan rate mV/s | C_s F/cm² | C_m F/g |
|--------------|----------------------|---------------------------|--|---------------------------------|
| 1.5 | M-CB-MWCNT | 2 | 6.17 | 154.98 |
| | | 5 | 5.75 | 143.57 |
| | | 10 | 5.59 | 137.58 |
| | | 20 | 5.42 | 132.81 |
| | | 50 | 4.51 | 112.38 |
| | | 100 | 2.35 | 58.14 |
| | M-FH-CB-MWCNT | 2 | 5.75 | 144.21 |
| | | 5 | 5.18 | 127.53 |
| | | 10 | 4.65 | 113.56 |
| | | 20 | 3.99 | 99.59 |
| | | 50 | 2.49 | 63.00 |
| | | 100 | 1.12 | 27.51 |
| | M-PV-MWCNT | 2 | 4.39 | 109.91 |
| | | 5 | 3.98 | 96.97 |
| | | 10 | 3.48 | 87.54 |
| | | 20 | 3.24 | 82.13 |
| | | 50 | 2.65 | 65.75 |
| | | 100 | 1.75 | 45.30 |
| | M-AA-MWCNT | 2 | 3.51 | 87.52 |
| | | 5 | 3.48 | 84.42 |
| | | 10 | 3.25 | 81.00 |
| | | 20 | 3.23 | 81.23 |
| | | 50 | 2.75 | 68.53 |
| | | 100 | 1.65 | 43.48 |
| | M-CP-MWCNT | 2 | 3.61 | 95.11 |
| | | 5 | 3.45 | 85.49 |
| | | 10 | 3.24 | 80.14 |
| | | 20 | 2.81 | 70.79 |
| | | 50 | 1.95 | 46.21 |
| | | 100 | 1.01 | 25.00 |

Table 6.2 Detailed results for GCD, the average C_s , C_m versus scan rates capacitance vs. scan rate for (a) M-CB-MWCNT, (b) M-FH-CB-MWCNT, (c) M-PV-MWCNT,(d) M-AA-MWCNT and (e) M-CP-MWCNT electrodes.

| Gamma | Composite | Scan rate mV/s | C_s F/cm² | C_m F/g |
|--------------|----------------------|---------------------------|--|---------------------------------|
| 1.5 | M-CB-MWCNT | 3 | 5.45 | 137.50 |
| | | 5 | 5.21 | 134.60 |
| | | 7 | 5.13 | 132.50 |
| | | 10 | 5.11 | 130.40 |
| | M-FH-CB-MWCNT | 3 | 4.84 | 132.40 |
| | | 5 | 4.70 | 132.30 |
| | | 7 | 4.61 | 129.30 |
| | | 10 | 4.60 | 128.80 |
| | M-PV-MWCNT | 3 | 4.10 | 103.50 |
| | | 5 | 3.93 | 100.20 |
| | | 7 | 3.71 | 90.21 |
| | | 10 | 3.72 | 89.84 |
| | M-AA-MWCNT | 3 | 3.45 | 88.10 |
| | | 5 | 3.39 | 87.50 |
| | | 10 | 3.38 | 84.10 |
| | | 20 | 3.38 | 82.50 |
| | M-CP-MWCNT | 3 | 3.15 | 81.5 |
| | | 5 | 3.05 | 75.10 |
| | | 7 | 3.02 | 75.00 |
| | | 10 | 2.75 | 69.5 |

Chapter 7

Pseudocapacitive behavior of ferrimagnetic NiFe_2O_4 - carbon nanotube electrodes prepared with a multifunctional dispersing agent.

Mohamed Nawwar^a, Rakesh P. Sahu^b, Ishwar K. Puri^{a,b} and Igor Zhitomirsky^{a,*},

^a Department of Materials Science and Engineering,

^b Department of Mechanical Engineering

McMaster University, Hamilton, Ontario, Canada L8S 4L7

* Corresponding Author: zhitom@mcmaster.ca.

Submitted on 12 April 2021, Published on 24 May 2021.

Reprinted with Permission from Elsevier Ltd on behalf of European Ceramic Society

2666-5395/© 2021, CC BY-NC-ND license.

Copyright 2021, Reproduced with Permission from Open Ceramics peer-reviewed Journal

- Open Access journal of the European Ceramic Society

7.1 Abstract

We investigate the pseudocapacitive properties of ferrimagnetic NiFe_2O_4 ceramics in a 0.5 M Na_2SO_4 aqueous electrolyte. These ceramics have a high capacitance of 2.33 F cm^{-2} since a more efficient colloidal technique is applied, which enhances the current response of the electrode in the negative potential range. NiFe_2O_4 is co-dispersed with multiwalled carbon nanotubes (MWCNTs) using Celestine Blue (CB) dye as a multifunctional co-dispersant. The capacitance measurements are performed by cyclic voltammetry, impedance spectroscopy and galvanostatic charge-discharge. The experiments reveal the synergistic effects of NiFe_2O_4 and conductive MWCNTs additives and the benefit they provide through co-dispersion with CB, which acts as an electron transfer mediator, enhancing pseudocapacitance. The mass ratio of NiFe_2O_4 and MWCNTs in the composite electrodes is varied to optimize the capacitance enhancement, lower electrical resistance at a high active mass loading of 40 mg cm^{-2} , and achieve favorable capacitance retention at high charge-discharge rates. The results reveal a path for the development of pseudocapacitive ferrimagnetic ceramic composites that have advanced functionality.

Keywords: pseudocapacitance, ferrimagnetic, spinel, dispersant, charge transfer, dye

7.2 Introduction

The combination of the magnetic and electrical capacitive properties of ceramic materials offers the potential to develop many novel applications in multifunctional devices. The discovery [1-3] of magnetically ordered ferroelectrics or multiferroics has generated interest in materials that combine the magnetic ordering with a high capacitance that result from spontaneous ferroelectric polarization due to the influence of the magnetic field on material electrical properties and vice versa [4]. However, the relatively high conductivity of some magnetically ordered ferroelectrics limits the occurrence of magnetocapacitive effects at room temperature, but here investigations of the pseudocapacitive properties of magnetic materials [5-7] and multiferroics [8] have revealed a new research avenue. Pseudocapacitive materials exhibit superior electrical capacitance [9-11] compared to that of ferroelectric materials. The capacitance of pseudocapacitors is typically by 6-8 orders of magnitude higher [12] than of ferroelectric capacitors of the same mass. Ideal pseudocapacitive and ferroelectric materials exhibit rectangular current-voltage dependences at low voltages [12, 13]. However, the origin of this pseudocapacitance is different from that of ferroelectric dipole capacitance. Pseudocapacitive properties of materials result from fast reversible redox reactions [14]. Therefore, in contrast to ferroelectric materials, a high material conductivity is an important beneficial factor for efficient pseudocapacitive charge-discharge [12]. Pseudocapacitors can operate at low voltages. In contrast, higher voltages can be applied to ferroelectric materials. However, the dielectric constant and capacitance of ferroelectric materials decreases drastically with increasing voltage. Moreover, the current-voltage characteristics of ferroelectric

capacitors at high voltages can deviate significantly from ideal capacitive rectangular shapes due to various polarization switching phenomena. The dielectric constant of ferroelectric materials decreases with decreasing crystal size to the nanometer scale. In contrast, the pseudocapacitance increases with decreasing particle size and increasing surface area. The use of nanoparticles with the high surface area is crucial to utilize high theoretical pseudocapacitance of suitable materials for practical applications.

The materials science of magnetically ordered pseudocapacitors (MOPC) is an emerging field of technological and scientific interest [6, 15, 16]. Of particular importance are ferrimagnetic MOPC ceramic materials, such as spinels [17-19] and hexagonal ferrites [20], which exhibit high magnetization at room temperature. MOPC materials can have enhanced charge storage properties induced by magnetic fields [21, 22]. However, the mechanism of this pseudocapacitance increase under the influence of a magnetic field is not well understood. Investigations of paramagnetic Mn_3O_4 at room temperature have shown that the pseudocapacitance is reduced under the influence of a magnetic field [22]. The fabrication of pseudocapacitive electrodes that are influenced by magnetic fields offers a unique opportunity to manipulate microstructure design to improve their pseudocapacitive behavior [23-25]. Significant progress has been made in the magnetic field-assisted preparation of advanced pseudocapacitors based on paramagnetic oxides [23-25]. However, strong magnetic interactions between particles of ferrimagnetic MOPC can enhance nanoparticle agglomeration and diminish mixing with conductive additives, which is detrimental for pseudocapacitive performance. There is significant interest in NiFe_2O_4 spinel, which has ferrimagnetic ordering and high dielectric constant [26-29]. Previous

investigations have focused on the fabrication of NiFe_2O_4 -based multiferroic composites with high capacitance [30-33] and magnetocapacitive thin film devices [34-36]. Other investigations showed that NiFe_2O_4 is a promising MOPC material, where its pseudocapacitive behavior in KOH electrolytes has a relatively high capacitance in both positive and negative potential windows [37, 38]. Enhanced capacitive behavior in KOH electrolytes has been reported for various NiFe_2O_4 based composites, containing graphene [39, 40], reduced graphene oxide [41], SiO_2 [42], NiO [43], activated carbon [44, 45], and layered double hydroxides [46]. The literature describes the pseudocapacitive properties of NiFe_2O_4 based composites in H_2SO_4 [47, 48], KNO_3 [49], NaCl [50], and gel electrolytes [51-53]. The capacitive behavior in an Na_2SO_4 electrolyte is of particular interest for fabricating asymmetric capacitors with an enlarged voltage window. While the promising behavior of this arrangement is known [54], investigations have been limited to electrodes with the relatively low active mass [55, 56] of 5 mg cm^{-2} . Superior electrode performance must be achieved at high active mass for electrodes with high areal capacitance (C_s) and low resistance. The goal of this investigation was to fabricate advanced NiFe_2O_4 based composites containing carbon nanotubes as conductive additives for operation in an Na_2SO_4 electrolyte. We used a multifunctional co-dispersing agent to disperse the NiFe_2O_4 and carbon nanotubes, which reduced the agglomeration of NiFe_2O_4 and carbon nanotubes. The better co-dispersion facilitated greater mixing of these components and thus allowed the fabrication of high active mass electrodes with higher areal capacitance and lower resistance. The redox-active dispersant acted as a charge transfer agent, which enhanced the MOPC NiFe_2O_4 electrical response.

7.3 Experimental procedures

Celestine blue dye (CB), NiFe_2O_4 (particle size <100 nm), Na_2SO_4 , ethanol, poly(vinyl butyral-co-vinyl-alcohol-co-vinyl-acetate) (PVB, average MW = 50,000-80,000), multiwalled carbon nanotubes (MWCNTs, purity $> 95\%$, OD 20-30 nm, and length 1–2 μm , US Nanomaterial Inc, USA), and Ni foam (porosity of 95%, Vale Ltd., Canada) were used.

Mixtures of NiFe_2O_4 and MWCNTs with different mass ratios γ ($\text{NiFe}_2\text{O}_4/\text{MWCNTs}$) = 1, 1.5, 2.5, and 4 in DI water were prepared and CB was added as a dispersant. Due to the low density and high aspect ratio of MWCNTs, we were not able to impregnate more than 20 mg cm^{-2} MWCNTs into the commercial Ni foam current collectors. Therefore, in order to compare electrode performance at the same total mass loadings (40 mg cm^{-2}), the $\text{NiFe}_2\text{O}_4/\text{MWCNTs}$ mass ratio was changed in a limited range of 1-4. The mass of the added CB was 15 % of the total mass of NiFe_2O_4 and MWCNTs. The CB content was optimized at the level of 15% in order to achieve good colloidal stability at a minimum dispersant content in the colloidal suspension. The resulting mixture was ultrasonicated, filtrated, washed with DI water to remove non-adsorbed CB, and redispersed in ethanol by ultrasonic agitation. NiFe_2O_4 and MWCNTs with different γ were also dispersed by ultrasonic treatment in ethanol without the use of a dispersant. PVB binder was added to the suspensions, the amount of PVB was 3% of the total mass of NiFe_2O_4 and MWCNTs. The suspensions of NiFe_2O_4 and MWCNTs in ethanol containing dissolved PVB were used for the impregnation of commercial Ni foam current collectors.

Transmission Electron Microscopy (TEM) was performed using a JEOL 2010F field emission microscope. Elemental analysis was performed using EDX by line and mapping analysis. X-ray diffraction (XRD) analysis was performed using a Bruker D8 DISCOVER instrument comprising DAVINCI diffractometer and Co-K α radiation. FTIR measurements were carried out on a Bruker Vertex 70 spectrometer in the wavenumber range of 400 - 2000 cm⁻¹.

Cyclic voltammetry (CV) and electrochemical impedance spectroscopy (EIS) studies of single electrodes were performed as described in prior investigations [14]. Galvanostatic charge-discharge (GCD) was performed using Biologic VMP 300 at current densities of 3 - 40 mA cm⁻². Areal capacitances (C_s) and gravimetric capacitances (C_m) were calculated from the CV, GCD, and EIS data, as described elsewhere [12].

7.4 Results and discussion

We have developed a facile approach to fabricate NiFe₂O₄-MWCNTs composite electrodes that have enhanced pseudocapacitive performance by addressing issues related to composite design by using CB as a multifunctional dispersing agent. The major difficulty in utilizing NiFe₂O₄ nanoparticles for supercapacitors is related to particle agglomeration, which results not only from the Van der Waals attraction forces but also from strong magnetic interactions. Therefore, ferrimagnetic NiFe₂O₄ nanoparticles must be well-dispersed using a superior dispersant. Another obstacle for NiFe₂O₄ application in supercapacitors is related to the low conductivity of this material. Therefore, conductive additives, such as MWCNTs, must be added to NiFe₂O₄ to format nanocomposites with enhanced electronic conductivity. MWCNTs are prone to strong agglomeration due to their

hydrophobic interactions. Therefore, the use of dispersant that co-disperses NiFe_2O_4 and MWCNTs is critical for their good mixing. High charge transfer resistance is another factor, limiting charge transfer between redox-active materials, conductive additives, and current collectors. These problems were addressed by using CB as a multifunctional catecholate molecule. The selection of CB as a dispersant was motivated by various considerations, as described below. Catecholate molecules are gaining attention as efficient dispersants for inorganic nanoparticles. The basis for using catecholates [57] in the colloidal processing of inorganic nanomaterials comes from the investigation of super-strong mussel adsorption on inorganic materials, which involves the bonding of chelating catechol monomers of their proteins to surface metal atoms. Catecholate molecules are of particular interest for the surface modification of magnetic nanoparticles. Catecholate adsorption on magnetic nanoparticles restores the structure and magnetic properties of the surface magnetically dead layer, resulting in enhanced particle magnetization and an increase in the superparamagnetic blocking temperature [58, 59]. The NiFe_2O_4 and MWCNTs suspensions prepared using CB as a dispersant had enhanced colloidal stability compared to suspensions prepared without CB. Sedimentation tests showed that the NiFe_2O_4 and MWCNTs suspensions in ethanol were stable for more than 4 days.

Figure 7.1 shows a chemical structure of CB, which is a cationic polyaromatic molecule, containing a catechol group. The greater colloidal stability of the suspensions results from CB adsorption on NiFe_2O_4 and MWCNTs. The CB adsorption on NiFe_2O_4 occurs due to chelating bonding of the catechol group Figure 7.1 (B), whereas π - π

interactions promote CB adsorption on MWCNTs. Similar to other small aromatic dispersants, CB facilitates MWCNTs dispersion via the unzipping mechanism [60]. The adsorbed CB imparts a positive charge to NiFe_2O_4 and MWCNT for the electrostatic dispersion, which improves their mixing in the composite electrode Figure 7.1 (C).

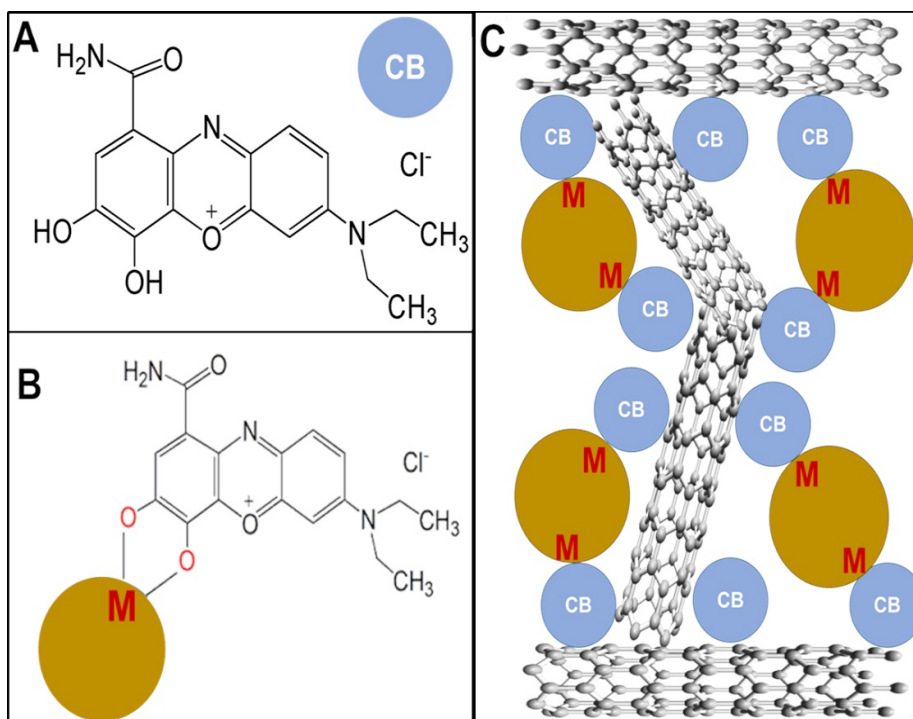


Figure 7.1 (A) Chemical structure of cationic CB, containing a chelating catechol group (B) interaction of CB with NiFe_2O_4 particles: chelating bonding with M (Ni, Fe), and (C) unzipping mechanism of MWCNTs dispersion using CB, decoration of MWCNTs and NiFe_2O_4 by CB interaction with both materials.

Figure 7.2 shows X-ray diffraction patterns of a mechanical mixture of NiFe_2O_4 with MWCNTs and a NiFe_2O_4 -MWCNTs ($\gamma=1$) composite prepared using CB as a co-dispersant. The diffraction peaks correspond to JCPDS files of spinel NiFe_2O_4 phase (file 74-1913) and MWCNTs (file 22-1012).

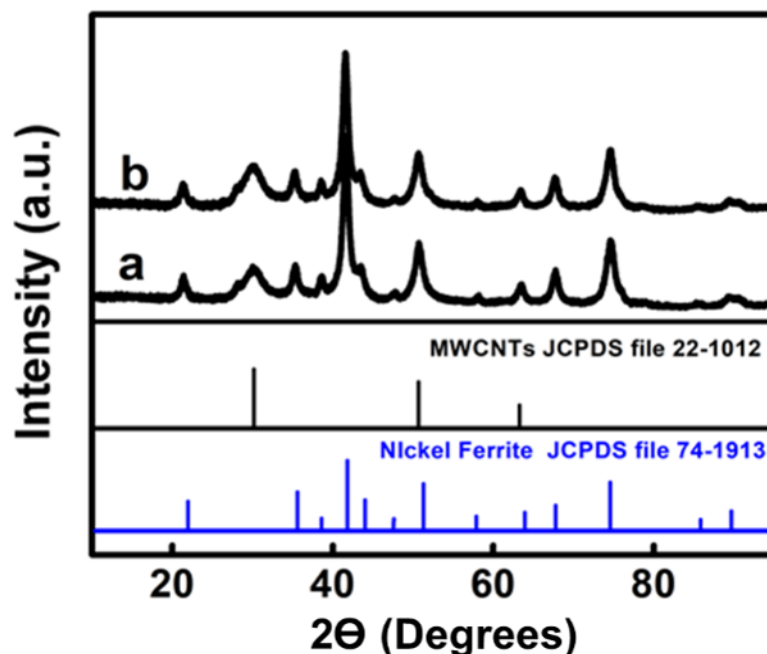


Figure 7.2 X-ray diffraction patterns of (a) mixture of NiFe_2O_4 with MWCNTs and (b) NiFe_2O_4 -MWCNTs composite, prepared using CB for $\gamma = 1$ in comparison with JCPDS file 22-1012 and 74-1913.

The FTIR spectrum of the NiFe_2O_4 -MWCNTs ($\gamma=1$) composite shows absorptions, which is not observed in the spectrum of the mechanical mixture (Figure 7.3). These absorptions are attributed to the adsorbed CB. The absorptions at 1550 , 1450 , and 1390 cm^{-1} result from the stretching of aromatic rings $\nu(\text{C}-\text{C})$ and $\nu(\text{C}=\text{C})$ [61]. Small peaks at 1345 and 1325 cm^{-1} are attributed to $\nu(\text{C}-\text{N})$ and $\nu\text{ C}=\text{N})$ stretching vibrations [61]. The absorptions at 1255 and 1215 cm^{-1} represent $\text{C}-\text{O}$ and $\text{C}=\text{O}$ vibrations, respectively [62]. The absorption at 1175 cm^{-1} results from aryl oxygen stretching [63]. The bands at 1110 and 1072 cm^{-1} represented $\text{C}-\text{H}$ bending vibrations [64]. FTIR spectrum of the NiFe_2O_4 -MWCNTs ($\gamma=1$) composite showed absorptions, which were not observed in a spectrum of the mechanical mixture. Such absorptions were attributed to adsorbed CB. The

absorptions at 1550, 1450 and 1390 cm^{-1} resulted from aromatic rings stretching $\nu(\text{C}-\text{C})$ and $\nu(\text{C}=\text{C})$ [61]. Small peaks at 1345 and 1325 cm^{-1} can be attributed to $\nu(\text{C}-\text{N})$ and $\nu(\text{C}=\text{N})$ stretching vibrations [61]. The absorptions at 1255 and 1215 cm^{-1} represented the $\text{C}-\text{O}$ and $\text{C}=\text{O}$ vibrations, respectively [62]. The absorption at 1175 cm^{-1} resulted from aryl oxygen stretching [63]. The bands at 1110 and 1072 cm^{-1} represented C-H bending vibrations [64].

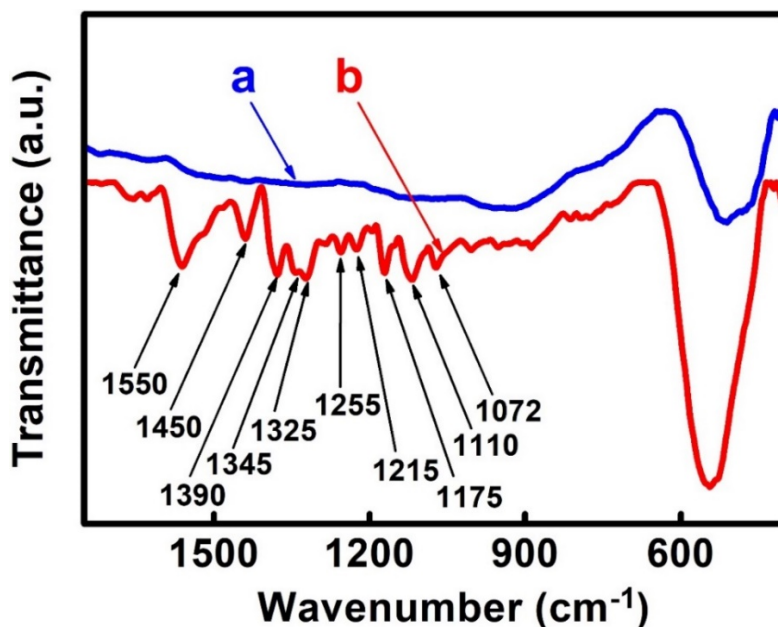


Figure 7.3 FTIR spectrum data for (a) mixture of NiFe_2O_4 with MWCNTs and (b) NiFe_2O_4 -MWCNTs composite, prepared using CB, for $\gamma = 1$.

The microstructure of the composite prepared using the CB dispersant is shown in Figure 7.4. The TEM data coupled with the related EDX line scan and mapping data show NiFe_2O_4 nanoparticles attached to MWCNTs. The TEM images indicate good mixing of the NiFe_2O_4 nanoparticles and MWCNTs, which is important for the electrochemical performance of the composite.

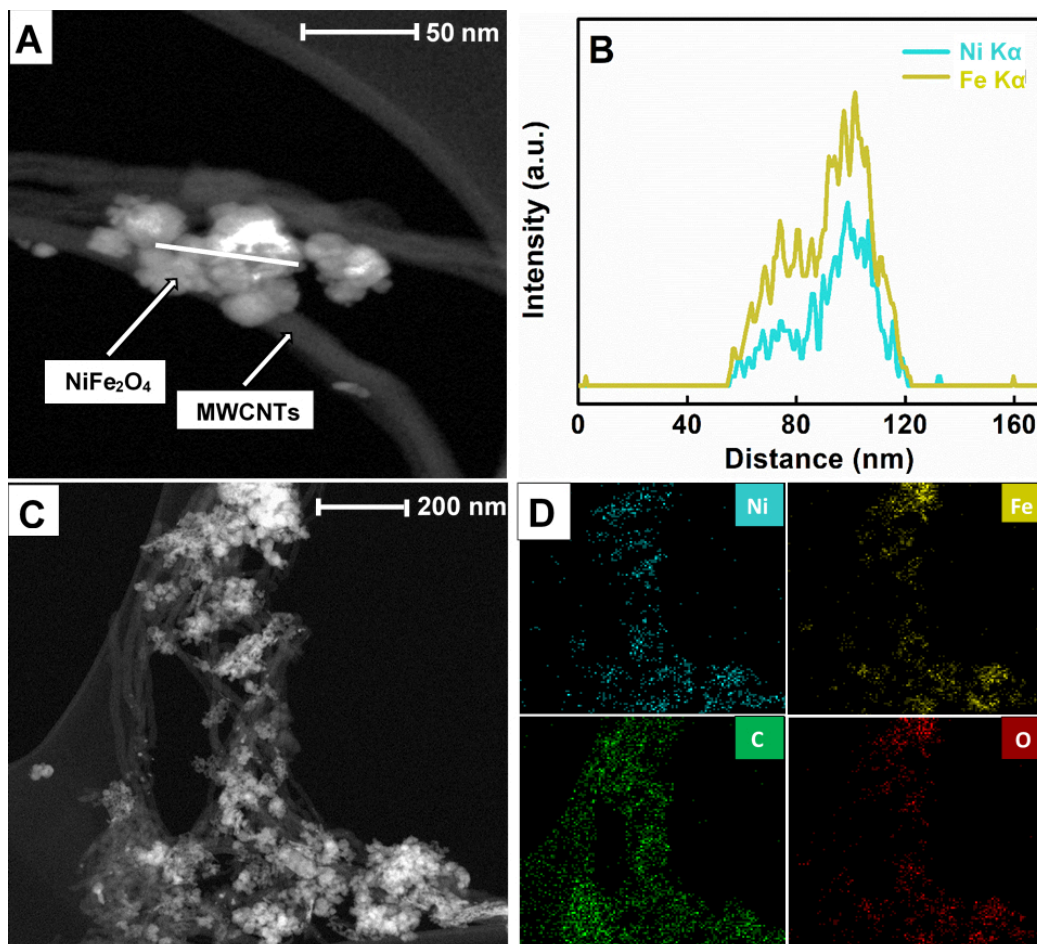


Figure 7.4 (A-D) TEM images of NiFe₂O₄-MWCNT ($\gamma=1$) prepared using CB and related EDX data: (A,C) TEM images at different magnifications, (B) EDX line scan for Fe and Ni for the line shown in (A); (D) EDX mapping for elements (Ni, Fe, C, O) for the image shown in (C).

Electrochemical testing is performed on the electrodes, containing individual materials, their mixture and composites prepared using CB as a dispersant. Previous investigations show that the performance of supercapacitor electrodes decreases significantly with increasing mass loading and highlights the need to develop efficient electrodes with high active mass above 10-20 mg cm⁻², which is necessary for practical

applications. Therefore, in this investigation, special attention is focused on the fabrication of electrodes with high active mass, a synergistic effect of NiFe_2O_4 nanoparticles and MWCNTs, and beneficial effect of CB.

Figure 7.5 compares electrochemical testing results for 20 mg cm^{-2} NiFe_2O_4 electrodes, 20 mg cm^{-2} MWCNTs electrodes and 40 mg cm^{-2} electrodes that contain a mechanical mixture of 20 mg cm^{-2} NiFe_2O_4 and 20 mg cm^{-2} MWCNTs. The CVs for the 20 mg cm^{-2} NiFe_2O_4 electrodes and 20 mg cm^{-2} MWCNTs electrodes show relatively low currents Figure 7.5 (A) and capacitances Figure 7.5 (B). The highest capacitance of the NiFe_2O_4 electrodes is 0.058 F cm^{-2} at a scan rate of 2 mV cm^{-2} . The capacitance decreases to 0.005 F cm^{-2} at a scan rate of 100 mV s^{-1} due to the poor electronic conductivity of NiFe_2O_4 . The capacitance of MWCNTs electrodes is about 0.23 F cm^{-2} at 2 mV cm^{-2} and it shows very small variations as the scan rate increases, attributed to a double layer capacitance. Electrodes containing the NiFe_2O_4 and MWCNTs mixture show a significantly higher CV area Figure 7.5 (A) and likewise a higher capacitance Figure 7.5 (B), compared to those for the individual materials. The capacitance of the electrode containing NiFe_2O_4 and MWCNTs mixture is 0.89 F cm^{-2} , which is significantly higher than the sum of the capacitances of the electrodes containing the individual components. Therefore, the result indicates that the two materials have synergistic effects. This enhanced capacitance results from better utilization of the capacitive properties of NiFe_2O_4 in the presence of conductive MWCNTs additives. The results of EIS presented in the Nyquist plot Figure 7.5 (C) show a relatively large real part of the complex impedance, which indicates high resistance. This resistance decreases significantly after the addition of MWCNTs. Therefore, efficient

electron transfer is a critically important factor influencing the capacitive properties of NiFe_2O_4 . The capacitive properties of the electrodes were also analyzed by calculating the real (C_s') and imaginary (C_s'') parts of the capacitance derived from the impedance data Figure 7.5 (D,E). The frequency dependence of C_s' and C_s'' , shows that C_s' for the mixture is significantly higher than the sum of the contributions of the individual components, which is in agreement with CV data. The electrodes, containing the NiFe_2O_4 and MWCNTs mixture have a relatively high relaxation frequency corresponding to the C_s'' maximum, indicating improved capacitive properties over a relatively wide frequency range as compared to pure NiFe_2O_4 electrodes.

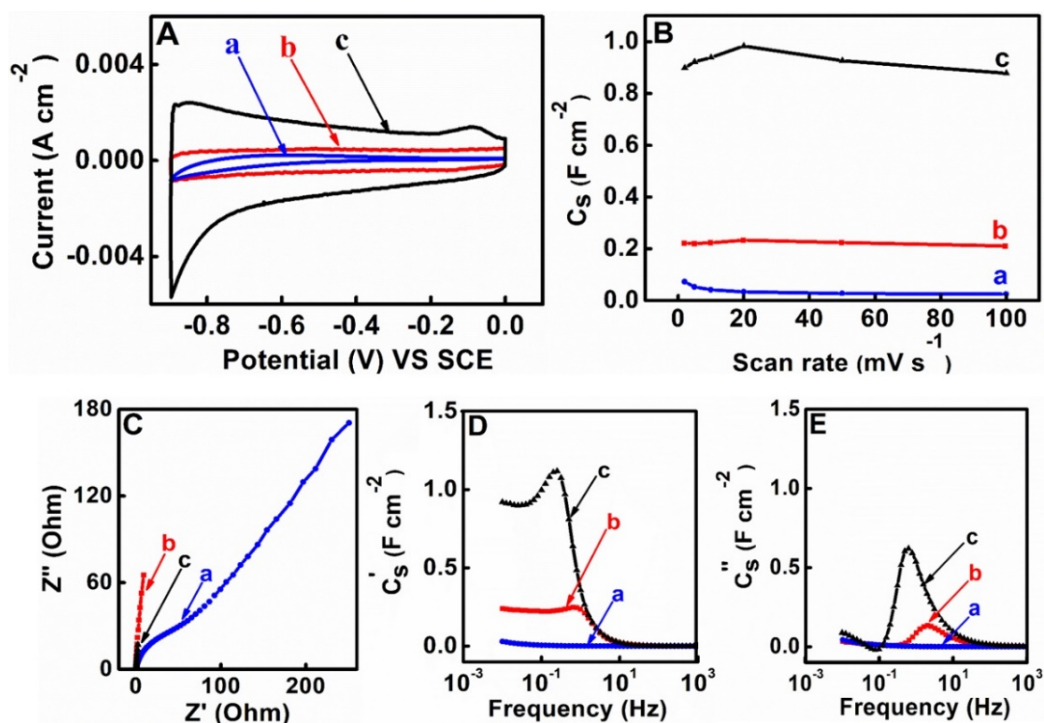


Figure 7.5 (A) CVs at a scan rate of 2 mV s⁻¹, (B) C_s versus scan rate, (C) EIS Nyquist plot, (D) C_s' versus frequency and (E) C_s'' versus frequency for electrodes, containing (a) 20 mg cm⁻² NiFe_2O_4 (b) 20 mg cm⁻² MWCNTs, and (c) a mixture of 20 mg cm⁻² NiFe_2O_4 and 20 mg cm⁻² MWCNTs.

The capacitive properties of NiFe_2O_4 -MWCNT composites prepared using CB as a dispersant are presented and compared with capacitive data (Figure 7.6) for the mechanical mixtures with $\gamma=1-4$, where the total active mass of the electrodes is 40 mg cm^{-2} . Figure 7.6 compares electrochemical testing results for the electrodes with $\gamma=1.5$. The electrodes prepared with CB as a dispersant show a significantly larger CV area, especially in the potential range of $-0.4 - 0.0 \text{ V}$. The capacitances for electrodes prepared with and without CB dispersant are 2.17 and 0.84 F cm^{-2} , respectively, at a scan rate of 2 mV s^{-1} . EIS measurements show relatively low Z' , however electrodes prepared with CB show higher Z' despite the higher currents observed in the CV data. The real part of the capacitance C' at low frequencies for the electrode prepared without CB is comparable with the corresponding C_s values at low scan rates. Electrodes prepared using CB have higher capacitances at low frequencies, but C' derived from the EIS data was lower than the C_s obtained from the CV data.

The difference in the EIS and CV capacitances has also been observed in other investigations [65] and attributed to the existence of redox sites with a wide range of redox potentials. Hence, EIS data is obtained at a low voltage of 5mV when some redox sites do not contribute to the capacitance. Both electrodes showed relatively high relaxation frequencies corresponding to the C_s'' maxima.

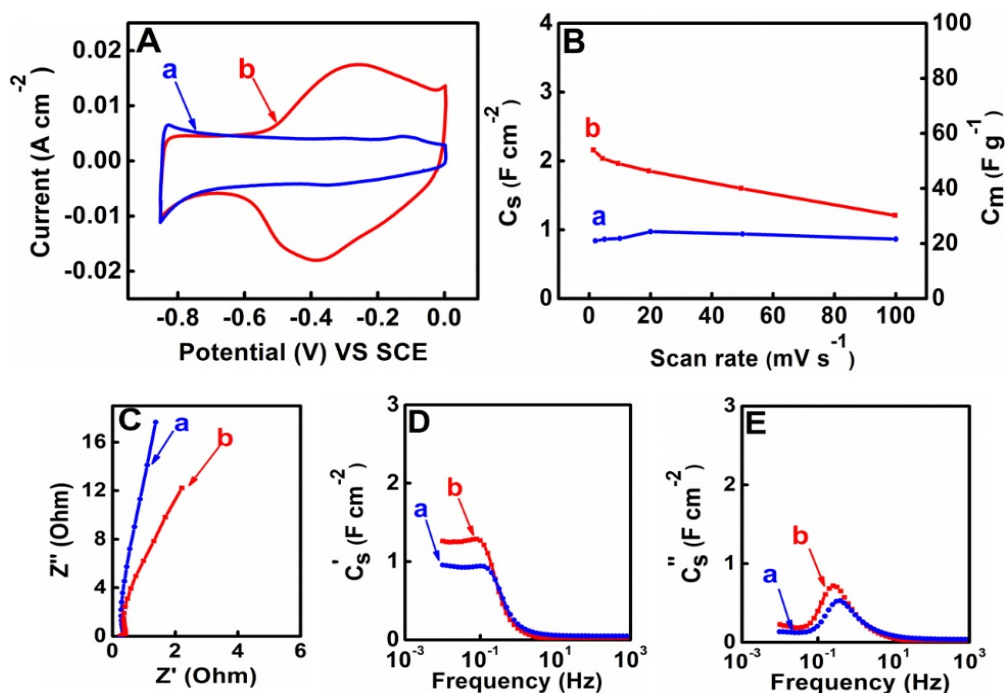


Figure 7.6 (A) CVs at scan rate of 5 mV s⁻¹, (B) capacitance versus scan rate, (C) EIS Nyquist plot, (D) Cs' versus frequency and (E) Cs'' versus frequency for NiFe₂O₄-MWCNTs electrodes with $\gamma = 1.5$, prepared (a) without CB (b) using CB as a dispersant.

Figure 7.7 compares electrochemical measurements for electrodes prepared using CB at different γ . The CVs have enlarged areas Figure 7.7 (A) in the -0.4 – 0 V potential range. The capacitances, obtained at a sweep rate of 2 mV s⁻¹, were 2.33, 2.15 and 1.91 F cm⁻² for $\gamma = 1$, $\gamma = 2.5$ and $\gamma = 4$, respectively Figure 7.7 (B). Comparing the data shown in Figure 7.5 and Figure 7.7 indicates that electrodes with $\gamma = 1$ prepared using CB have significantly higher capacitances as compared to electrodes prepared without CB. Electrodes prepared using CB and $\gamma = 1$ have improved capacitance retention at higher sweep rates and significantly higher capacitances at 100 mV s⁻¹ compared to other electrodes. The lowest electrode resistance occurs at $\gamma = 1$ Figure 7.7 (C).

The results of impedance spectroscopy agree with the results of CV measurements and reveal that the highest C_s' occurs at $\gamma = 1$. Electrodes prepared using CB show relatively high relaxation frequencies, indicating good capacitive response at high frequencies.

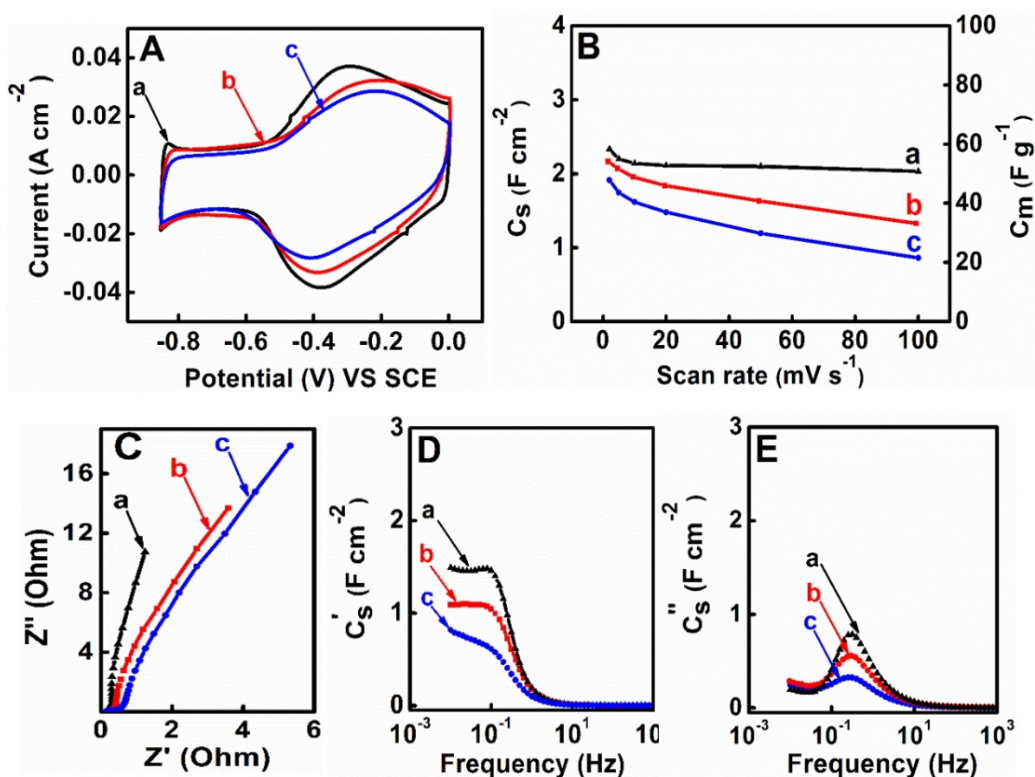


Figure 7.7 (A) CVs at scan rate of 10 mV s⁻¹, (B) capacitance versus scan rate, (C) EIS Nyquist plot, (D) C_s' versus frequency and (E) C_s'' versus frequency for NiFe₂O₄ - MWCNTs electrodes prepared using CB for (a) $\gamma = 1$, (b) $\gamma = 2.5$ and (c) $\gamma = 4$.

The charge-discharge behavior of the electrodes is also investigated at different constant current densities in the 3-40 mA cm⁻² range. Electrodes with $\gamma = 1$ show the largest charge-discharge times, particularly at high current densities Figure 7.8 (A,B). This is attributed to their higher capacitance, which is determined from the discharge data and presented in Figure 7.8 © versus current density. The capacitance for electrodes with $\gamma = 1$ exhibits small

variations with increasing current density, which, in agreement with the CV data, indicates good capacitance retention at high charge-discharge rates Figure 7.7(B). The Coulombic efficiency remains close to 100% after 1000 cycles, however the capacitance retention reduces to 85% Figure 7.8 (D). Therefore, further investigation must focus on the improvement of the cyclic stability of the electrodes.

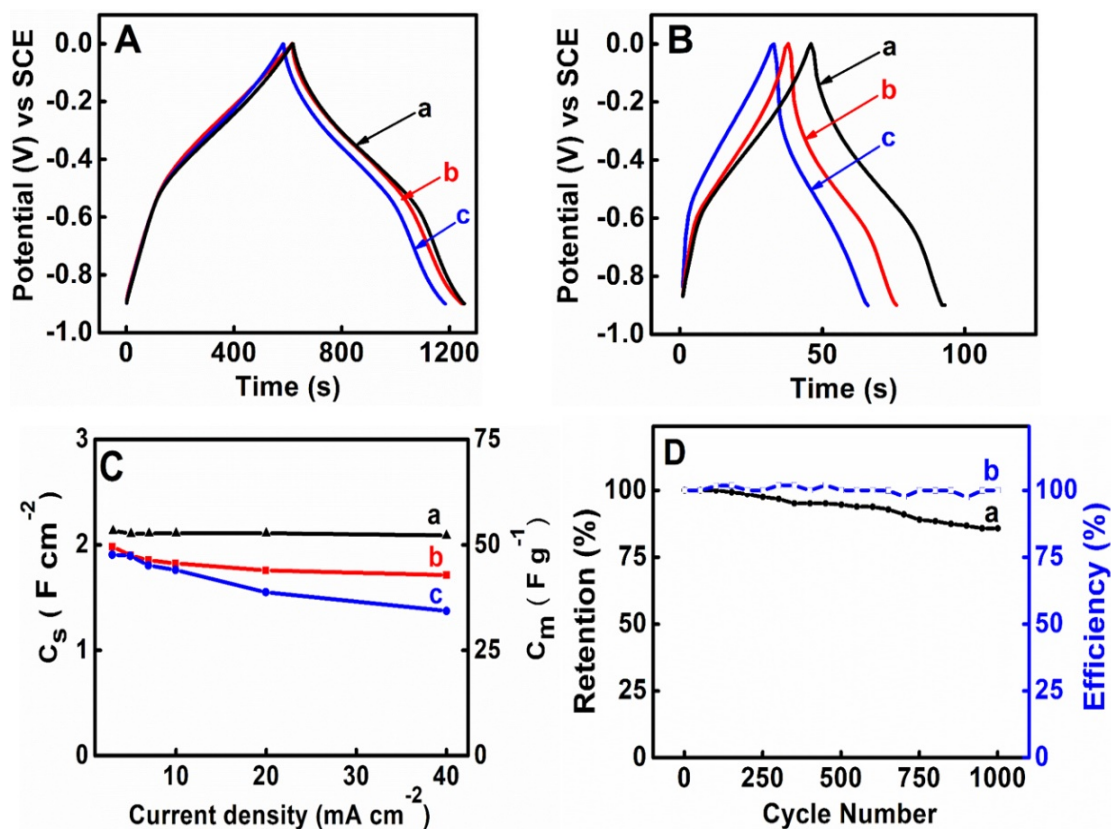


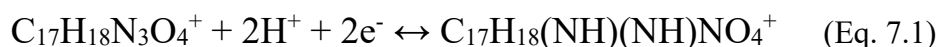
Figure 7.8 (A) Charge-discharge curves at current densities of 3 mA cm⁻² and (B) 40 mA cm⁻², (C) capacitance versus current density for NiFe₂O₄-MWCNTs composites with (a) $\gamma = 1$ (b) $\gamma = 2.5$, and (c) $\gamma = 4$. (D) (a) Capacitance retention and (b) Coulombic efficiency versus cycle number for $\gamma = 1$.

The experimental measurements indicate that the capacitance of the NiFe₂O₄ electrodes is enhanced by adding conductive MWCNTs and using CB as a multifunctional dispersant.

However, the mechanism of capacitance enhancement in composites that are prepared with CB as a dispersant is not well understood. Analysis of the experimental results and available literature allow us to suggest a mechanism. The enhanced dispersion of NiFe_2O_4 and MWCNTs in the presence of CB indicates that CB is partially adsorbed on the electrode materials. The non-adsorbed CB is washed away during the material preparation. As mentioned above, CB adsorption on NiFe_2O_4 nanoparticles involves catecholate type bonding Figure 7.1(B), whereas π - π interactions promote CB adsorption on MWCNTs. The isoelectric point of NiFe_2O_4 is located at $\text{pH} \sim 6.7$ [66]. Application of a negative potential to the electrode usually results in a local pH increase due to electrode reactions in aqueous electrolytes [67, 68]. Therefore, NiFe_2O_4 particles can be expected to acquire a negative charge and promote electrostatic attraction and adsorption of positively charged CB.

Different mechanisms can enhance the capacitance of electrodes containing adsorbed catecholate molecules. Catechol exhibits redox reactions related to the oxidation of its phenolic OH groups [69]. Catechol-modified carbon cloth electrodes have enhanced capacitance due to the contribution of electrochemical oxidation of the OH groups of catechol [69]. Redox properties of catechol, related to oxidation of their phenolic OH groups, are used for electron transfer mediation in capacitive-type electrochemical biosensors[70]. Several electron transfer mediators are used to develop electrochemical biosensors and enhance their current response significantly. However, the two mechanisms described above and based on catechol oxidation at positive potentials cannot explain the higher capacitance of the CB modified NiFe_2O_4 -MWCNTs electrodes in the negative potential range. In both mechanisms, the OH groups of catechol were not involved in the

adsorption on the electrode material. In contrast, adsorption of catecholates, such as Tiron and Alizarin Red on inorganic surfaces, involves chelating or bridge bonding of their phenolic OH group to metal atoms on inorganic surfaces [71-74]. This bonding facilitates electron transfer from inorganic materials to organic materials [71-74]. A similar adsorption mechanism is involved in CB adsorption on NiO nanoparticles [75]. In contrast to other catecholate molecules, CB also exhibits redox properties in a negative potential range through the following reduction reaction [75]



The adsorbed redox-active CB facilitated electron transfer occurs during an electrocatalytic process in the negative potential range [75] above $\sim -0.5\text{V}$. This improvement in the electrochemical response of the electrode results from a charge transfer mediation mechanism [75]. Therefore, it is suggested that catecholate bonding of CB to the Ni or Fe atoms on the NiFe_2O_4 surface and redox reaction (Eq. 7.1) facilitates electron transfer to electrochemically active NiFe_2O_4 and enhances the capacitance of the electrode.

The pseudocapacitive properties of NiFe_2O_4 in the negative potential range are attributed to the reduction of Fe^{3+} to Fe^{2+} , which has a lower magnetic moment. However, the magnetic ordering in ferrimagnetic oxides is influenced by the magnetic moments of the paramagnetic ions involved in super-exchange interactions. Therefore, the change in the valence state of the paramagnetic ions and their magnetic moments in the pseudocapacitive redox reactions can potentially result in interesting magneto-pseudocapacitive effects in MOPC. The results of this investigation indicated that enhanced electron transfer is an important factor for the observation of the pseudocapacitive behavior of such materials.

7.5 Conclusions

This study demonstrates how the pseudocapacitive properties of electrodes are advanced with ferrimagnetic NiFe_2O_4 ceramic nanoparticles. A high 2.33 F cm^{-2} capacitance is achieved at low resistance for an active mass of 40 mg cm^{-2} and $\gamma=1$. The electrodes show good capacitance retention with increasing CV scan rate, GCD current density, and EIS frequency. The capacitance decreases with increasing γ in the 1-4 range. The high capacitance results from the synergistic effect of NiFe_2O_4 and the conductive MWCNT additive, and the application of CB as a co-dispersant and electron transfer mediator. The multifunctional properties of CB result from the polyaromatic chemical structure of this molecule that contains a catechol group, its electric charge and redox-active properties. The results open an avenue for fabricating advanced ceramic MOPC materials by combining pseudocapacitive and ferrimagnetic properties.

7.6 Declaration of competing interest

The authors do not have any conflict of interest to report.

7.7 Acknowledgments

The Natural Sciences and Engineering Research Council of Canada funded this research, grant number RGPIN-2018-04014. TEM investigations were performed at the Canadian Centre for Electron Microscopy. M. Nawwar would like to thank the government of Egypt for their sponsorship, in addition to Dr. Aithal Srivatsa for his help in FTIR characterization.

7.8 References

- [1] Y.E. Roginskaya, Y.N. Venevtsev, G. Zhdanov, New magnetic ferroelectrics, Soviet Physics JETP 21 (1965) 817-822.
- [2] L. Shvorneva, Y. Venevtsev, Perovskites with ferroelectric-magnetic properties, Sov Phys JETP 22 (1966) 722-724.
- [3] Y.E. Roginskaya, Y.Y. Tomashpol'Skiĭ, Y.N. Venevtsev, V. Petrov, G. Zhdanov, The nature of the dielectric and magnetic properties of BiFeO₃, Soviet Journal of Experimental and Theoretical Physics 23 (1966) 47.
- [4] Y.N. Venevtsev, V.V. Gagulin, I.D. Zhitomirsky, Material science aspects of seignette-magnetism problem, Ferroelectrics 73(1) (1987) 221-248.
- [5] M. Aghazadeh, I. Karimzadeh, M.R. Ganjali, Preparation of Nano-sized Bismuth-Doped Fe₃O₄ as an Excellent Magnetic Material for Supercapacitor Electrodes, Journal of Electronic Materials 47(5) (2018) 3026-3036.
- [6] H. Kennaz, A. Harat, O. Guellati, D.Y. Momodu, F. Barzegar, J.K. Dangbegnon, N. Manyala, M. Guerioune, Synthesis and electrochemical investigation of spinel cobalt ferrite magnetic nanoparticles for supercapacitor application, Journal of Solid State Electrochemistry 22(3) (2018) 835-847.
- [7] N. Sinan, E. Unur, Fe₃O₄/carbon nanocomposite: Investigation of capacitive & magnetic properties for supercapacitor applications, Materials Chemistry and Physics 183 (2016) 571-579.
- [8] Y. Liu, I. Zhitomirsky, Electrochemical supercapacitor based on multiferroic BiMn₂O₅, Journal of Power Sources 284 (2015) 377-382.
- [9] J.A. Argüello, A. Cerpa, R. Moreno, Reinforcing effect of graphene nanoplatelets in the electrochemical behaviour of manganese oxide-based supercapacitors produced by EPD, Ceramics International 45(11) (2019) 14316-14321.

- [10] M. Dinesh, Y. Haldorai, R.T. Rajendra Kumar, Mn–Ni binary metal oxide for high-performance supercapacitor and electro-catalyst for oxygen evolution reaction, *Ceramics International* 46(18, Part A) (2020) 28006-28012.
- [11] V. Sannasi, K. Subbian, High-pseudocapacitance of MnCo_2O_4 nanostructures prepared by phenolphthalein assisted hydrothermal and microwave methods, *Ceramics International* 46(10, Part A) (2020) 15510-15520.
- [12] R. Chen, M. Yu, R.P. Sahu, I.K. Puri, I. Zhitomirsky, The Development of Pseudocapacitor Electrodes and Devices with High Active Mass Loading, *Advanced Energy Materials* 10(20) (2020) 1903848.
- [13] M. Cheong, I. Zhitomirsky, Electrophoretic deposition of manganese oxide films, *Surface Engineering* 25(5) (2009) 346-352.
- [14] Y. Zhu, K. Shi, I. Zhitomirsky, Polypyrrole coated carbon nanotubes for supercapacitor devices with enhanced electrochemical performance, *Journal of Power Sources* 268 (2014) 233-239.
- [15] M. Aghazadeh, Zn-doped magnetite nanoparticles: development of novel preparation method and evaluation of magnetic and electrochemical capacitance performances, *Journal of Materials Science: Materials in Electronics* 28(24) (2017) 18755-18764.
- [16] K. Bhattacharya, P. Deb, Hybrid nanostructured C-dot decorated Fe_3O_4 electrode materials for superior electrochemical energy storage performance, *Dalton Transactions* 44(19) (2015) 9221-9229.
- [17] S. Meena, K.S. Anantharaju, S. Malini, A. Dey, L. Renuka, S.C. Prashantha, Y.S. Vidya, Impact of temperature-induced oxygen vacancies in polyhedron MnFe_2O_4 nanoparticles: As excellent electrochemical sensor, supercapacitor and active photocatalyst, *Ceramics International* <https://doi.org/10.1016/j.ceramint.2020.12.217>.

- [18] V.V. Deshmukh, H.P. Nagaswarupa, N. Raghavendra, Development of Co-doped MnFe_2O_4 nanoparticles for electrochemical supercapacitors, *Ceramics International* 47(7, Part B) (2021) 10268-10273.
- [19] S.M. Alshehri, J. Ahmed, A.N. Alhabarah, T. Ahamad, T. Ahmad, Nitrogen-Doped Cobalt Ferrite/Carbon Nanocomposites for Supercapacitor Applications, *ChemElectroChem* 4(11) (2017) 2952-8.
- [20] E. Rezaie, A. Rezanezhad, L.S. Ghadimi, A. Hajalilou, N. Arsalani, Effect of calcination on structural and supercapacitance properties of hydrothermally synthesized plate-like $\text{SrFe}_{12}\text{O}_{19}$ hexaferrite nanoparticles, *Ceramics International* 44(16) (2018) 20285-20290.
- [21] A. Viswanathan, A.N. Shetty, Real time magnetic supercapacitor with antiferromagnetic nickel hydroxide based nanocomposite, *Electrochimica Acta* 309 (2019) 187-196.
- [22] S. Pal, S. Majumder, S. Dutta, S. Banerjee, B. Satpati, S. De, Magnetic field induced electrochemical performance enhancement in reduced graphene oxide anchored Fe_3O_4 nanoparticle hybrid based supercapacitor, *Journal of Physics D: Applied Physics* 51(37) (2018) 375501.
- [23] T. Zhu, Y. Xie, G. Zhang, Z. He, Y. Lu, H. Guo, C. Lin, Y. Chen, Magnetic-field-assisted synthesis of Co_3O_4 nanoneedles with superior electrochemical capacitance, *Journal of Nanoparticle Research* 17(12) (2015) 484.
- [24] T. Liu, Y. Li, G. Quan, P. Dai, X. Yu, M. Wu, Z. Sun, G. Li, Magnetic-field-assisted preparation of one-dimensional (1-D) wire-like $\text{NiO}/\text{Co}_3\text{O}_4$ composite for improved specific capacitance and cycle ability, *Materials Letters* 139 (2015) 208-211.
- [25] K. Hoshino, Y. Asano, A. Magori, Electrochemical capacitor performance of cobalt compound nanowires electrosynthesized in magnetic fields, *Materials Chemistry and Physics* 204 (2018) 132-140.

- [26] L. Chauhan, S. Kumar, K. Sreenivas, A. Shukla, Variable range hopping and modulus relaxation in NiFe_2O_4 ceramics, *Materials Chemistry and Physics* 259 (2021) 124135.
- [27] S. Choudhury, M. Sinha, M. Mandal, S. Pradhan, A. Meikap, Electrical transport properties of nanocrystalline nonstoichiometric nickel ferrite at and above room temperature, *Physica B: Condensed Matter* 457 (2015) 225-231.
- [28] F. Hezam, A. Rajeh, O. Nur, M. Mustafa, Synthesis and physical properties of spinel ferrites/MWCNTs hybrids nanocomposites for energy storage and photocatalytic applications, *Physica B: Condensed Matter* 596 (2020) 412389.
- [29] S. Mandal, S. Singh, P. Dey, J. Roy, P. Mandal, T. Nath, Frequency and temperature dependence of dielectric and electrical properties of TFe_2O_4 (T= Ni, Zn, $\text{Zn}_{0.5}\text{Ni}_{0.5}$) ferrite nanocrystals, *Journal of Alloys and Compounds* 656 (2016) 887-896.
- [30] C. Behera, R. Choudhary, P.R. Das, Development of Ni-ferrite-based PVDF nanomultiferroics, *Journal of Electronic Materials* 46(10) (2017) 6009-6022.
- [31] L. Zhu, Y. Dong, X. Zhang, Y. Yao, W. Weng, G. Han, N. Ma, P. Du, Microstructure and properties of sol-gel derived $\text{PbTiO}_3/\text{NiFe}_2\text{O}_4$ multiferroic composite thin film with the two nano-crystalline phases dispersed homogeneously, *Journal of Alloys and Compounds* 503(2) (2010) 426-430.
- [32] K.C. Verma, R. Kotnala, Nanostructural and lattice contributions to multiferroism in $\text{NiFe}_2\text{O}_4/\text{BaTiO}_3$, *Materials Chemistry and Physics* 174 (2016) 120-128.
- [33] Z. Zheng, P. Zhou, Y. Liu, K. Liang, R. Tanguturi, H. Chen, G. Srinivasan, Y. Qi, T. Zhang, Strain effect on magnetoelectric coupling of epitaxial NFO/PZT heterostructure, *Journal of Alloys and Compounds* 818 (2020) 152871.
- [34] N.A. Ahir, A.V. Takaloo, K.A. Nirmal, S.S. Kundale, M.Y. Chougale, J. Bae, D.-k. Kim, T.D. Dongale, Capacitive coupled non-zero I-V and type-II memristive properties of the $\text{NiFe}_2\text{O}_4\text{-TiO}_2$ nanocomposite, *Materials Science in Semiconductor Processing* 125 (2021) 105646.

- [35] G. Boni, L. Hrib, S. Porter, G. Atcheson, I. Pintilie, K. Rode, L. Pintilie, Electrical properties of NiFe_2O_4 epitaxial ultra-thin films, *Journal of Materials Science* 52(2) (2017) 793-803.
- [36] C. Jin, E. Jiang, H. Bai, Resistive hysteresis and capacitance effect in $\text{NiFe}_2\text{O}_4/\text{SrTiO}_3$: Nb (1 wt%) junctions, *Applied surface science* 257(21) (2011) 8998-9001.
- [37] T. Huang, W. Cui, Z. Qiu, Z. Hu, Z. Zhang, 2D porous layered NiFe_2O_4 by a facile hydrothermal method for asymmetric supercapacitor, *Ionics* 27(3) (2021) 1347-1355.
- [38] X. Gao, W. Wang, J. Bi, Y. Chen, X. Hao, X. Sun, J. Zhang, Morphology-controllable preparation of NiFe_2O_4 as high performance electrode material for supercapacitor, *Electrochimica Acta* 296 (2019) 181-189.
- [39] A.-R. Shaymaa, R. Rajagopalan, C. Subramaniam, Z. Tai, J. Xian, X. Wang, S.X. Dou, Z. Cheng, NiFe_2O_4 nanoparticles coated on 3D graphene capsule as electrode for advanced energy storage applications, *Dalton Transactions* 47(39) (2018) 14052-14059.
- [40] M. Sethi, U.S. Shenoy, D.K. Bhat, A porous graphene– NiFe_2O_4 nanocomposite with high electrochemical performance and high cycling stability for energy storage applications, *Nanoscale Advances* 2(9) (2020) 4229-4241.
- [41] M.B. Askari, P. Salarizadeh, Binary nickel ferrite oxide (NiFe_2O_4) nanoparticles coated on reduced graphene oxide as stable and high-performance asymmetric supercapacitor electrode material, *International Journal of Hydrogen Energy* 45(51) (2020) 27482-27491.
- [42] M.M. Baig, E. Pervaiz, M. Azad, Z. Jahan, M.B.K. Niazi, S.M. Baig, $\text{NiFe}_2\text{O}_4/\text{SiO}_2$ nanostructures as a potential electrode material for high rated supercapacitors, *Ceramics International* (2021).
- [43] Y. Zhang, W. Zhang, C. Yu, Z. Liu, X. Yu, F. Meng, Synthesis, structure and supercapacitive behavior of spinel NiFe_2O_4 and $\text{NiO}@ \text{NiFe}_2\text{O}_4$ nanoparticles, *Ceramics International* 47(7) (2021) 10063-10071.

- [44] L. Liu, S. Hu, K. Gao, Natural nanofiber-based stacked porous nitrogen-doped carbon/NiFe₂O₄ nanohybrid nanosheets, *Cellulose* 27(2) (2020) 1021-1031.
- [45] T. Uzzaman, S. Zawar, M.T. Ansar, S.M. Ramay, A. Mahmood, S. Atiq, Electrochemical Performance of NiFe₂O₄ Nanostructures Incorporating Activated Carbon as an Efficient Electrode Material, *Ceramics International* (2020).
- [46] S. Li, J. Pan, F. Li, L. Zhang, D. Chai, Z. Zhang, J. Xin, Bimetallic FeNi-MIL-88-derived NiFe₂O₄@ Ni-Mn LDH composite electrode material for a high performance asymmetric supercapacitor, *Dalton Transactions* 49(29) (2020) 10203-10211.
- [47] J. Ge, G. Fan, Y. Si, J. He, H.-Y. Kim, B. Ding, S.S. Al-Deyab, M. El-Newehy, J. Yu, Elastic and hierarchical porous carbon nanofibrous membranes incorporated with NiFe₂O₄ nanocrystals for highly efficient capacitive energy storage, *Nanoscale* 8(4) (2016) 2195-2204.
- [48] S.S. Scindia, R.B. Kamble, J.A. Kher, Nickel ferrite/polypyrrole core-shell composite as an efficient electrode material for high-performance supercapacitor, *AIP Advances* 9(5) (2019) 055218.
- [49] X. Zhang, M. Zhu, T. Ouyang, Y. Chen, J. Yan, K. Zhu, K. Ye, G. Wang, K. Cheng, D. Cao, NiFe₂O₄ nanocubes anchored on reduced graphene oxide cryogel to achieve a 1.8 V flexible solid-state symmetric supercapacitor, *Chemical Engineering Journal* 360 (2019) 171-179.
- [50] S. Anwar, K.S. Muthu, V. Ganesh, N. Lakshminarasimhan, A comparative study of electrochemical capacitive behavior of NiFe₂O₄ synthesized by different routes, *Journal of The Electrochemical Society* 158(8) (2011) A976.
- [51] S.B. Bandgar, M.M. Vadiyar, Y.-C. Ling, J.-Y. Chang, S.-H. Han, A.V. Ghule, S.S. Kolekar, Metal precursor dependent synthesis of NiFe₂O₄ thin films for high-performance flexible symmetric supercapacitor, *ACS Applied Energy Materials* 1(2) (2018) 638-648.

- [52] M.S. Javed, C. Zhang, L. Chen, Y. Xi, C. Hu, Hierarchical mesoporous NiFe_2O_4 nanocone forest directly growing on carbon textile for high performance flexible supercapacitors, *Journal of Materials Chemistry A* 4(22) (2016) 8851-8859.
- [53] Z.-Y. Yu, L.-F. Chen, S.-H. Yu, Growth of NiFe_2O_4 nanoparticles on carbon cloth for high performance flexible supercapacitors, *Journal of Materials Chemistry A* 2(28) (2014) 10889-10894.
- [54] Z. Wang, X. Zhang, Y. Li, Z. Liu, Z. Hao, Synthesis of graphene- NiFe_2O_4 nanocomposites and their electrochemical capacitive behavior, *Journal of Materials Chemistry A* 1(21) (2013) 6393-6399.
- [55] Y.-Z. Cai, W.-Q. Cao, P. He, Y.-L. Zhang, M.-S. Cao, NiFe_2O_4 nanoparticles on reduced graphene oxide for supercapacitor electrodes with improved capacitance, *Materials Research Express* 6(10) (2019) 105535.
- [56] Y.-Z. Cai, W.-Q. Cao, Y.-L. Zhang, P. He, J.-C. Shu, M.-S. Cao, Tailoring rGO- NiFe_2O_4 hybrids to tune transport of electrons and ions for supercapacitor electrodes, *Journal of Alloys and Compounds* 811 (2019) 152011.
- [57] M. Ata, Y. Liu, I. Zhitomirsky, A review of new methods of surface chemical modification, dispersion and electrophoretic deposition of metal oxide particles, *Rsc Advances* 4(43) (2014) 22716-22732.
- [58] D.K. Nagesha, B.D. Plouffe, M. Phan, L.H. Lewis, S. Sridhar, S.K. Murthy, Functionalization-induced improvement in magnetic properties of Fe_3O_4 nanoparticles for biomedical applications, *Journal of Applied Physics* 105(7) (2009) 07B317.
- [59] K.V. Korpany, F. Habib, M. Murugesu, A.S. Blum, Stable water-soluble iron oxide nanoparticles using Tiron, *Materials Chemistry and Physics* 138(1) (2013) 29-37.
- [60] M.S. Ata, R. Poon, A.M. Syed, J. Milne, I. Zhitomirsky, New developments in non-covalent surface modification, dispersion and electrophoretic deposition of carbon nanotubes, *Carbon* 130 (2018) 584-598.

- [61] Y. Liu, M. Ata, K. Shi, G.-z. Zhu, G. Botton, I. Zhitomirsky, Surface modification and cathodic electrophoretic deposition of ceramic materials and composites using celestine blue dye, *RSC advances* 4(56) (2014) 29652-29659.
- [62] Y. Sun, M. Ata, I. Zhitomirsky, Electrophoretic deposition of TiO₂ nanoparticles using organic dyes, *Journal of colloid and interface science* 369(1) (2012) 395-401.
- [63] Y. Sun, I. Zhitomirsky, Electrophoretic deposition of titanium dioxide using organic acids as charging additives, *Materials Letters* 73 (2012) 190-193.
- [64] Y. Wang, I. Zhitomirsky, Bio-inspired catechol chemistry for electrophoretic nanotechnology of oxide films, *Journal of colloid and interface science* 380(1) (2012) 8-15.
- [65] Y. Zhu, K. Shi, I. Zhitomirsky, Anionic dopant-dispersants for synthesis of polypyrrole coated carbon nanotubes and fabrication of supercapacitor electrodes with high active mass loading, *Journal of Materials Chemistry A* 2(35) (2014) 14666-14673.
- [66] R. Plaza, J. De Vicente, S. Gomez-Lopera, A. Delgado, Stability of dispersions of colloidal nickel ferrite spheres, *Journal of colloid and interface science* 242(2) (2001) 306-313.
- [67] X. Pang, I. Zhitomirsky, M. Niewczas, Cathodic electrolytic deposition of zirconia films, *Surface and Coatings Technology* 195(2) (2005) 138-146.
- [68] I. Zhitomirsky, Cathodic electrodeposition of ceramic and organoceramic materials. Fundamental aspects, *Advances in colloid and interface science* 97(1-3) (2002) 279-317.
- [69] D. Malka, S. Giladi, O. Hanna, M. Weitman, R. Cohen, Y. Elias, R. Attias, T. Brousse, A.A. Frimer, D. Aurbach, Catechol-Modified Carbon Cloth as Hybrid Electrode for Energy Storage Devices, *Journal of The Electrochemical Society* 166(6) (2019) A1147.
- [70] K. Yan, Y. Liu, Y. Guan, N. Bhokisham, C.-Y. Tsao, E. Kim, X.-W. Shi, Q. Wang, W.E. Bentley, G.F. Payne, Catechol-chitosan redox capacitor for added amplification in electrochemical immunoanalysis, *Colloids and Surfaces B: Biointerfaces* 169 (2018) 470-477.

- [71] D. Tallman, C. Vang, G. Wallace, G. Bierwagen, Direct electrodeposition of polypyrrole on aluminum and aluminum alloy by electron transfer mediation, *Journal of the Electrochemical Society* 149(3) (2002) C173.
- [72] S. Chen, I. Zhitomirsky, Influence of dopants and carbon nanotubes on polypyrrole electropolymerization and capacitive behavior, *Materials Letters* 98 (2013) 67-70.
- [73] C. Shi, I. Zhitomirsky, Electrodeposition of composite polypyrrole-carbon nanotube films, *Surface engineering* 27(9) (2011) 655-661.
- [74] G.-L. Wang, J.-J. Xu, H.-Y. Chen, Dopamine sensitized nanoporous TiO₂ film on electrodes: photoelectrochemical sensing of NADH under visible irradiation, *Biosensors and Bioelectronics* 24(8) (2009) 2494-2498.
- [75] A. Noorbakhsh, A. Salimi, Amperometric detection of hydrogen peroxide at nano-nickel oxide/thionine and celestine blue nanocomposite-modified glassy carbon electrodes, *Electrochimica acta* 54(26) (2009) 6312-6321.

7.9 Supporting informations

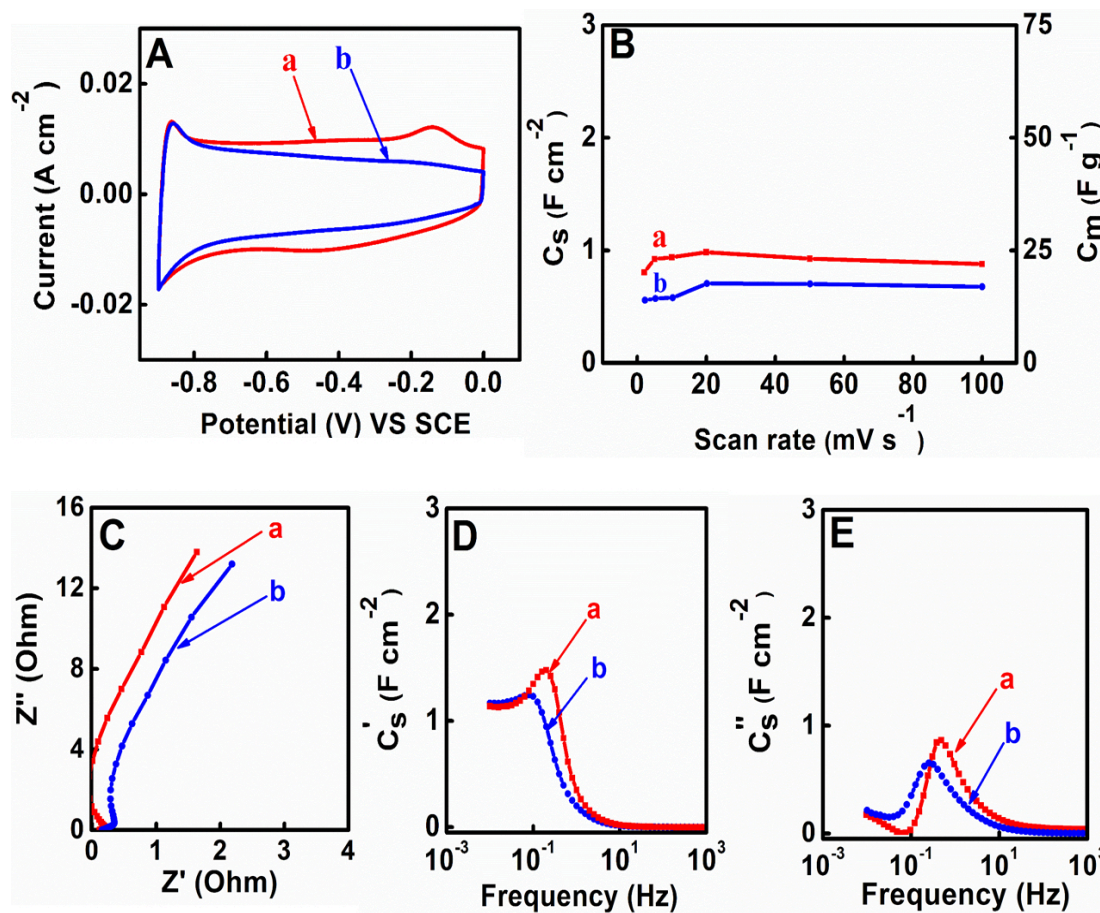


Figure 7.9 (A) CVs at scan rate of 5 mV s^{-1} , (B) C_s and C_m versus scan rate, (C) EIS Nyquist plot, (D) C_s' versus frequency and (E) C_s'' versus frequency for electrodes by 40 mg of NiFe_2O_4 /MWCNTs for $\gamma = 1$, prepared by physical mixing and probe sonication of (a) 5 min (b) 10 min.

Chapter 8

Conclusions and future works

8.1 Conclusions

Conceptually, new advanced colloidal processing techniques and advanced dispersants from different categories were developed and emerged to synthesis variant well-dispersed composites. Different gamma (γ) ratios (Fe_3O_4 or NiFe_2O_4 : MWCNTs) of these synthesized composites have been used in high-performance electrochemical capacitors (ESs) electrodes and devices with high active mass loading and high mass ratio of materials to the current collector. The significant innovations and contributions of this dissertation can be summarized as follows:

- Ultrasonic-assisted chemical synthesis of Fe_3O_4 in situ of activated carbon nanotubes (ACNTs) was efficient to fabricate Fe_3O_4 decorated MWCNTs (M-CNTs). Furthermore, using PA in the bottom-up PELLI method reduced the agglomeration of M-CNTs particles and improved the mixing of the composite components. As a result, well-dispersed M-CNTs composites have been used to fabricate the cathodic supercapacitor electrodes that showed remarkable areal capacitances and low resistance. The highest capacitance of the cathode electrode at high active mass loading of M-CNTs is 5.82 F cm^{-2} at 2 mV s^{-1} that has been achieved for $\gamma=1$ and 40 mg cm^{-2} . For the first time, advanced M-CNTs negative electrodes with a high capacitance comparable to MnO_2 -MWCNT positive electrodes at a similar high mass loading have been fabricated, which showed promising performance in a voltage window of 1.6 V.

- Celestine blue dye (CB) has been used as a multifunctional dispersing agent in the Fabrication of Fe_3O_4 decorated MWCNTs (M-CNTs) in different ultrasonic-assisted chemical synthesis methods, in situ-chemical precipitation (CCP) and physical mixing (PM). Celestine blue has been proved to promote the coating, dispersion and increase the conductivity of the active material by working as a charge transfer mediator for Fe_3O_4 and MWCNTs. The M-CNTs electrodes prepared using in situ (CCP) and 15% CB at different γ ratios showed lower resistance and higher capacitance and of 6.17 F cm^{-2} that was achieved for $\gamma=1.50$ at 2 mVs^{-1} . The asymmetric device based on negative electrode CB/M-CNTs and negative electrode CB/ Mn_3O_4 /MWCNTs have been fabricated, which showed promising performance 2.40 F cm^{-2} at 2 m Vs^{-1} with a large voltage window of 1.6 V.
- Different multifunctional dispersing agents with multiple coating mechanisms such as celestine blue dye (CB), Pyrocatechol violet (PV), azure A chloride (AAZ), and m-cresol purple (CP) have been used at in situ-chemical precipitation (CCP) method to fabricate M-CNTs and M-CNTs/ FeOOH composite materials. The presence of the catechol ligand in (CB) and (PV) has a remarkable effect on the dispersion/coating optimization compared to the effect of the electrostatic interactions that only present in (AAZ) and (CP). For the same γ and configurations, the CB/M-CNTs/ FeOOH electrode showed relatively higher stability (CV profile) compared to that one made by the CB/M-CNTs composite. The Galvanostatic charge-discharge (GCD) behavior of both CB/M-CNTs/ FeOOH and CB/M-CNTs electrodes showed high performance $> 5 \text{ F cm}^2$ and relative stability at different current densities. The asymmetric device

consists of the CB/M-CNTs/FeOOH as a negative electrode and CB/MnO₂/MWCNTs as a positive one has been fabricated, which showed promising performance 2.39 F cm⁻² at 2 mV s⁻¹ with a wide voltage window of 1.6 V.

- Ferrimagnetic NiFe₂O₄ ceramic nanoparticles have been developed to advance the pseudocapacitive properties of negative electrodes by using the application of CB as a co-dispersant and electron transfer mediator and the conductive MWCNT additive. The high areal capacitance of 2.33 F cm⁻² has been achieved at low resistance for an active mass of 40 mg cm⁻² and $\gamma=1$. The increased capacitance results from the synergistic effect of NiFe₂O₄, and the multifunctional properties of CB result from the polyaromatic chemical structure of this molecule that contains a catechol group, its electric charge and redox-active properties. The results open a route for the fabrication of advanced ceramic MOPC materials by combining pseudocapacitive and ferrimagnetic properties.

8.2 Future directions

In this thesis, it has been demonstrated that new advanced ESs composites have been developed and the several problems related to fabrication have been solved. Therefore, it is extremely important to continue the research for the development of new colloidal techniques and advanced composites for ESs application. Based on the research results in this thesis, promising directions will be proposed such as investigation of new dispersants with variant mechanisms and new materials particularly spinel based metal transition oxide as followings:

- To study the advantages of using solid solutions of Zinc ferrite (ZnFe_2O_4) in the applications of supercapacitor electrodes and devices.
- To develop and fabricate supercapacitor electrodes with a new redox material strontium ferrite ($\text{SrFe}_{12}\text{O}_{19}$) and vanadium oxides ($\text{V}_2\text{O}_5, \text{V}_2\text{O}_3$).